APPLICATION OF ENHANCED RESOLUTION IMAGING TO SSM/I DATA

Douglas R. Daum

Department of Electrical and Computer Engineering

M. S. Degree, Oct. 1994

ABSTRACT

The Backus Gilbert Inversion (BGI) technique and the Scatterometer Image Reconstruction (SIR) algorithm are investigated as methods to create enhanced resolution images. The methods offer similar resolution but SIR is computationally much more efficient. SIR processing times are one-twentieth of the BGI times. SIR is applied to Special Sensor Microwave/Imager (SSM/I) data to create images of the Amazon Basin. Using these SIR images, a method to remove atmospheric distortion from single pass images is developed. This method uses the single-pass SIR images to generate composite images representing the surface brightness temperature without small-scale, temporal distortion caused by clouds or precipitation. The utility of the composite images is illustrated through a vegetation discrimination study similar to studies completed with scatterometer images. The SSM/I algorithms discriminate correctly approximately 60% of the time. Other suggested uses of the composite images include multi-sensor vegetation studies, cloud and precipitation detection, and cloud and precipitation parameter extraction.

COMMITTEE APPROVAL:

David G. Long
Committee Chairman

David V. Arnold
Committee Member

Wynn C. Stirling
Graduate Coordinator

This thesis by Douglas R. Daum is accepted in its present form by the Department of Electrical and Computer Engineering of Brigham Young University as satisfying the thesis requirement for the degree of Master of Science.

David G. Long
Committee Chairman

David V. Arnold
Committee Member

Wynn C. Stirling
Graduate Coordinator

Date

ACKNOWLEDGMENTS

I thank my research advisor, Dr. David Long, for the support and advice he gave in developing and preparing the research in this thesis. His help has been invaluable. I also thank Dr. David Arnold and the other members of the BYU Microwave Remote Sensing Group for their evaluation of my research and my writing.

Lastly, I thank my wife, Heather, for lasting through our engagement as I prepared this thesis.

CONTENTS

LIST OF FIGURES

CHAPTER 1

INTRODUCTION

Microwave radiometers are electromagnetic receivers which measure radiation in the frequency band of 1-300 GHz. These devices were originally developed in the 1930's to study the microwave radiation produced in space [1]. The basic principle behind radiometry is that all matter emits electromagnetic radiation. The amount of emission depends on the matter's molecular composition, temperature, and geometric structure. Radiometers, therefore, are like very sensitive cameras that do not take pictures of the optical electromagnetic frequencies, but at much lower electromagnetic frequencies.

In the late 1950's scientists began to use microwave radiometers in terrestial studies. Microwave frequencies are particularly useful because they have a penetrating ability that optical frequencies do not have. They can more easily penetrate cloud water and atmosphere than other frequencies. In addition, they make measurements both day and night, thus offering 24 hour coverage. For this reason, radiometers have been placed on truck platforms, planes, and eventually satellites in order to learn more about the Earth.

Microwave radiometers are a very important means to ascertain geophysical information about the Earth. Global studies require measurements taken over large areas of the earth. For that reason, most radiometers have been designed to gather accurate measurements using relatively low resolution. These studies include atmospheric profiling over areas of constant background emission such as the ocean. Other studies include large area soil and plant moisture content [2, 3] and surface temperature measurement [4]. The low resolution, however, has discouraged the application of microwave radiometers in many studies.

Most spaceborne microwave radiometers have poor resolution when compared to other spaceborne sensors. The smallest resolvable area that most radiometers can detect is approximately the size of their antenna pattern on the Earth. These patterns are generally 20 to 150 km elliptical shapes called sensor footprints. In contrast, spaceborne optical sensors have resolution as fine as 10 m. In order to

overcome this low resolution, enhanced resolution reconstruction techniques have been developed and applied to microwave radiometers.

Enhanced resolution images are advantageous over raw data because they are able to extract features and boundaries smaller than the sensor footprint. Two such algorithms are the Scatterometer Image Reconstruction (SIR) technique [5, 6] and the Backus Gilbert Inversion (BGI) method [7, 8]. Part of this thesis will report on results of simulating, comparing, and evaluating these two algorithms as they pertain to land studies over the Amazon basin, showing that the radiometer data may be applied to vegetation studies.

In addition to having low resolution, spaceborne microwave sensors are adversely affected by cloud and precipitation interference. Although this interference is less than that experienced by optical sensors, the radiometer-derived images may still contain unwanted atmospheric artifacts which prevent the extraction of geophysical parameters. The second part of this thesis presents methods for removing the atmospheric distortion which increases the utility of the final images for gathering geophysical information about the Earth's surface. The data for this study was obtained from the seven frequency microwave radiometer known as the Special Sensor Microwave/Imager (SSM/I).

The contributions of this research are: (1) a qualitative comparison of SIR and BGI as applied to microwave radiometer data, (2) an application of SIR and BGI to Amazon basin imagery, (3) an objective atmospheric distortion removal method, (4) an appropriate method for combining radiometric SIR images to generate a surface mapping without atmospheric effects, (5) a study of the enhanced radiometric data for vegetation discrimination over the Amazon, and (6) a comparison of radiometer and scatterometer based vegetation discrimination.

Chapter 2 contains a brief introduction of microwave radiometry, the SSM/I, and resolution. Chapter 3 provides a detailed evaluation and comparison of SIR and BGI. Chapter 4 uses the enhanced resolution images to produce cloud-free "base" images of the Amazon. Chapter 5 applies the base images to study vegetation discrimination over the Amazon basin. Finally, conclusions and suggestions for further research are given in Chapter 6.

CHAPTER 2

BACKGROUND

2.1 Introduction

This chapter introduces the basic theory behind microwave radiometry and its application in spaceborne remote sensing. This chapter is not intended to be a full discussion of blackbody and radiative transfer theory, but it provides enough information to acquaint the reader with these theories for this thesis. Following that discussion, the chapter describes the effect of antenna patterns on radiometric measurements. This will lead to a discussion of the Special Sensor Microwave/Imager data used in this research and to a description of the geographical area of interest–the Amazon Basin. Lastly, to prepare the reader for following chapters, a brief review of image reconstruction and image resolution is presented.

2.2 Microwave Radiometric Theory

According to Plank's law, all matter emits energy in the form of electromagnetic radiation. In radiometric terminology this radiation is called brightness. The basic theory behind radiometric brightness is the blackbody radiator. Classically, a blackbody is defined as a perfect radiative absorber. In other words, any frequency and amount of radiation incident upon the material is absorbed by the molecules of the material. This energy absorbtion increases the temperature of the blackbody. The blackbody also acts as a perfect emitter. Plank developed an equation for the energy emitted (brightness B_f) by a blackbody,

$$B_f = \frac{2hf^3}{c^2}\left[\frac{1}{e^{hf/kT}-1}\right] \tag{2.1}$$

where the energy (in $Ws^{-1}m^{-2}Hz^{-1}$) is a function of Plank's constant (h), Boltzman's constant (k), the speed of light (c), radiative frequency (f), and absolute temperature (T). Since the brightness is a function of temperature, the body which emits energy is often described by its brightness temperature.

A non-ideal material is known as a *greybody* because it does not act like a perfect (black) absorber/emitter. All real substances are greybodies. Scientists have defined a quantity called emissivity as a measure of how close a greybody is to being a blackbody. Emissivity is the ratio of actual radiated power from the greybody (B_{gb}) over the theoretical power emitted by a blackbody (B_{bb}) at the same temperature (Eq. 2.2).

$$e = \frac{B_{gb}}{B_{bb}} \tag{2.2}$$

The emissivity of materials range from close to zero to almost unity. This difference in emissivity allows the radiometer to distinguish between different types of materials. In addition, although emissivity is non-polarized, the radiated power may be polarized due to the geometry of the radiating substance. This provides another method of distinguishing between different materials such as vegetation types.

A basic diagram of how a remote sensing spaceborne radiometric measurement is obtained is found in Figure 2.1. The figure illustrates the major contributions to measurements made by a spaceborne radiometer. First, there is upwelling radiation from the ground. This radiation is scattered and/or attenuated by vegetation, clouds, and precipitation. Some of the radiation is reflected back down by the vegetation or atmospheric conditions. Second, the clouds and vegetation also emit their own radiation both toward the radiometer and toward the ground. Third, the brightness of outer space contributes to the radiometric measurement in a lesser degree for downward looking radiometers. Thus, decomposing the observed energy into the various contributions is theoretically difficult to accomplish except under many simplifying assumptions. The most crucial factors affecting a radiometric measurement, however, are the surface emissivity, the vegetation canopy, and the atmospheric conditions. A more complete description of radiative transfer theory is found in [1].

2.3 Effect of Antenna Pattern on Brightness Measurements

The radiometric measurements are a function of the scene and the radiometer antenna pattern. Without atmospheric or vegetation distortion, a radiometric measurement can be modeled as a product of the surface brightness and

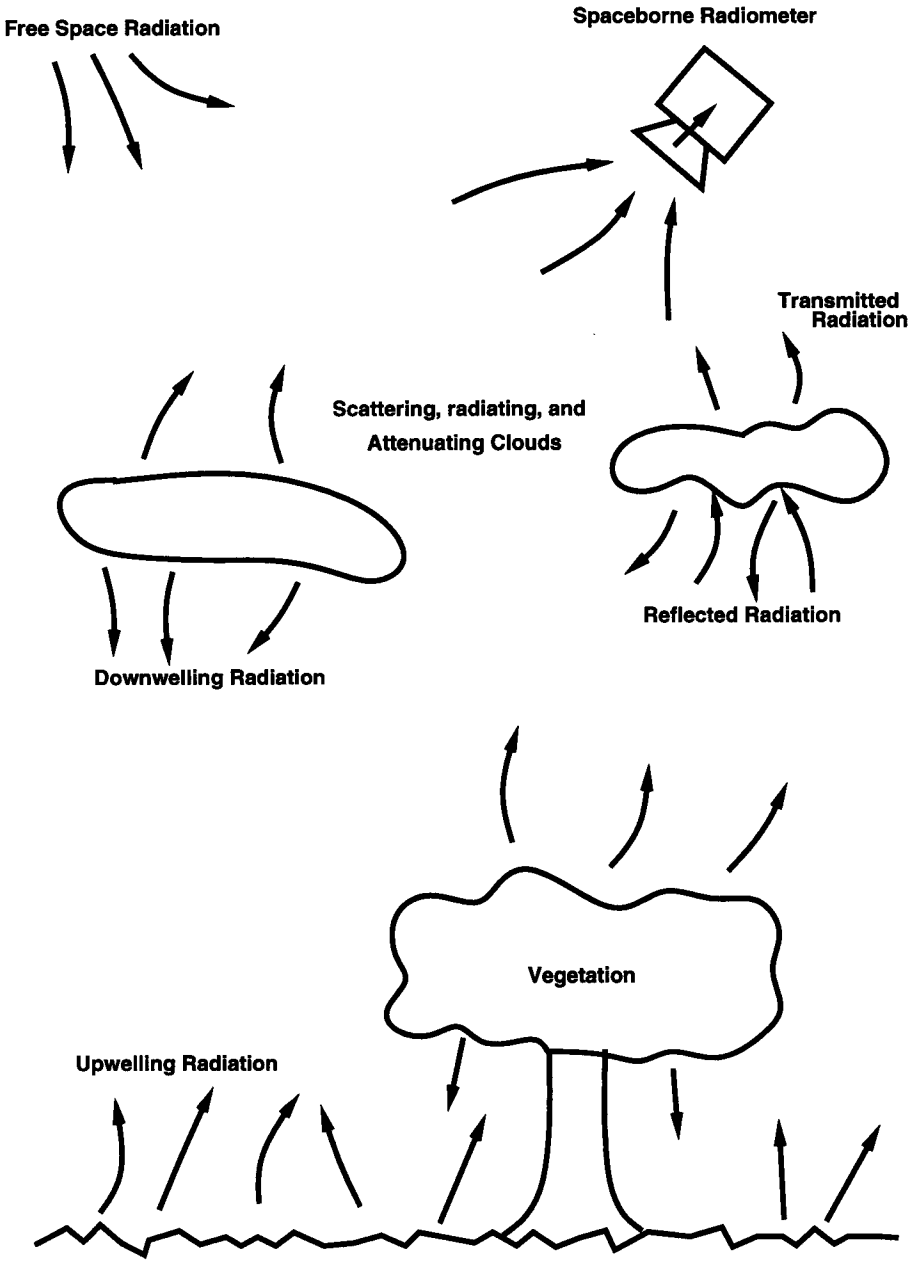

Figure 2.1: Radiative Transfer Measured by a Spaceborne Radiometer. Total Energy of Radiometer = Sum of Contributions with Attenuation and Scattering.

the antenna pattern. For example, a measurement T_0 is obtained about a point (x_o, y_o) by integrating the surface brightness response $h_o(x,y)$ (Km^{-2}) of that spot with the antenna pattern $G(x,y)$:

$$T_o = \frac{1}{G_o} \int \int G(x,y) h_o(x,y) dx dy, \tag{2.3}$$

where

$$G_o = \int \int G(x,y) dx dy.$$

These integrals are usually calculated over the non-negligible area of the antenna pattern. The antenna pattern is usually characterized by its half power limits. This characterization is known as the footprint. Radiometric footprints generally have an elliptical shape on the surface of the earth due to the elevation angle of the radiometer. (See Figure 2.2).

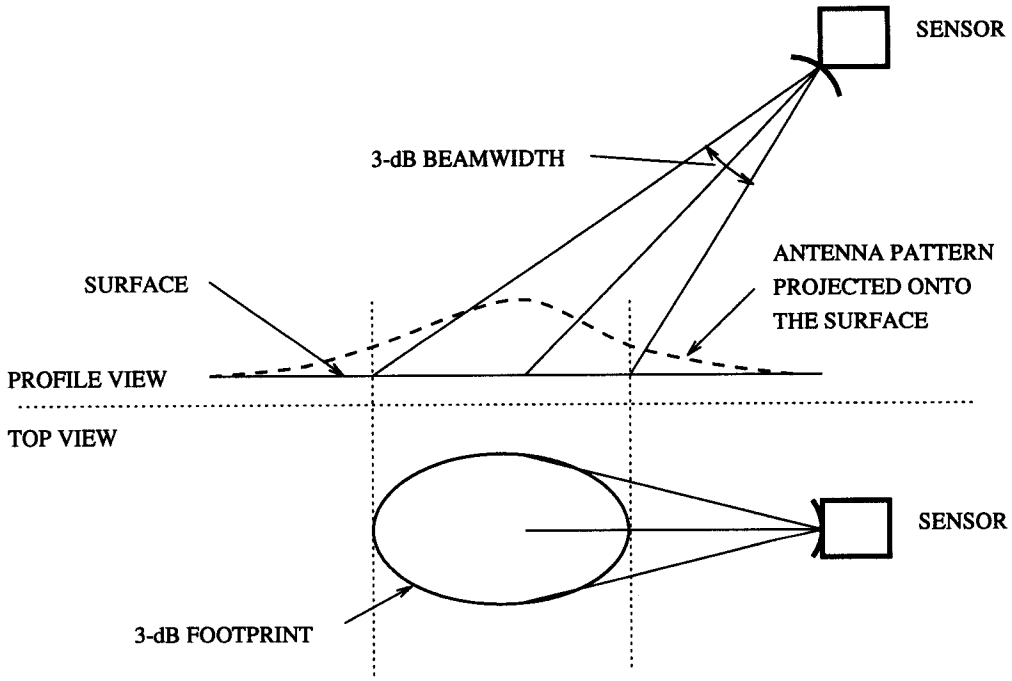

Figure 2.2: Radiometric Antenna Footprint from [6].

In addition, antenna patterns have sidelobe contributions. These contributions are neglected in this thesis since they are negligible for the microwave instrument used. A more extensive description of the radiometer data used in this thesis follows.

2.4 The Special Sensor Microwave/Imager (SSM/I)

This thesis discusses use of radiometric data from the Special Sensor Microwave/Imager (SSM/I). The SSM/I is part of the Defense Meteorological satellite Program (DMSP) funded by the Navy and Air Force [9]. The goal of the program is to retrieve geophysical mappings on a global scale. These include cloud liquid water content [10], precipitation retrieval [11], snow cover classification [12], and surface temperature measurement [4]. To gather this data, the military has launched three of these instruments into space, although only two are currently operational. The spacebased platforms have a near-polar orbit at about 833 km height and a period of 102.0 minutes. The swath width is approximately 1400 km resulting in global coverage every three days. Figure 2.3 illustrates the basics of the SSM/I coverage (from [9]).

The SSM/I is a total-power [1], seven channel, four frequency radiometer. The channels consist of the horizontal and vertical polarizations of 19.35, 22.23, 37.0, and 85.5 GHz with the exception that no 22.23 GHz h-pol is available. (For the SSM/I, horizontal polarization is when electric field is parallel to the Earth's surface, vertical polarization is perpendicular.) The 3dB footprints range from about 15-70 km in the along-track direction and 13-43 km in the cross-track direction. The antenna patterns are found in [9]. The measurements are made with an integrate-and-dump filter ranging from times of 3.89 ms for the 85.5 GHz channels to 7.95 ms for the other channels. The spatial distribution of these antenna pattern changes along the swath scan and begins to overlap at the edges of the 102 degree scan. (See Figure 2.4). Table 2.1 contains the basic channel information. Additional information is available in [9].

The SSM/I data used in this thesis comes from September, 1992. It was made available through the Brigham Young University's Microwave Earth Remote Sensing Group (MERS) who received it from Remote Sensing Systems, Santa Rosa, CA. The data was extracted from 8 mm tapes provided by Remote Sensing Systems and then processed on the MERS VAX workstations. Low level processing used software provided by Remote Sensing Systems [13] to extract brightness temperature measurements, their locations, and their time stamps from the raw tape data.

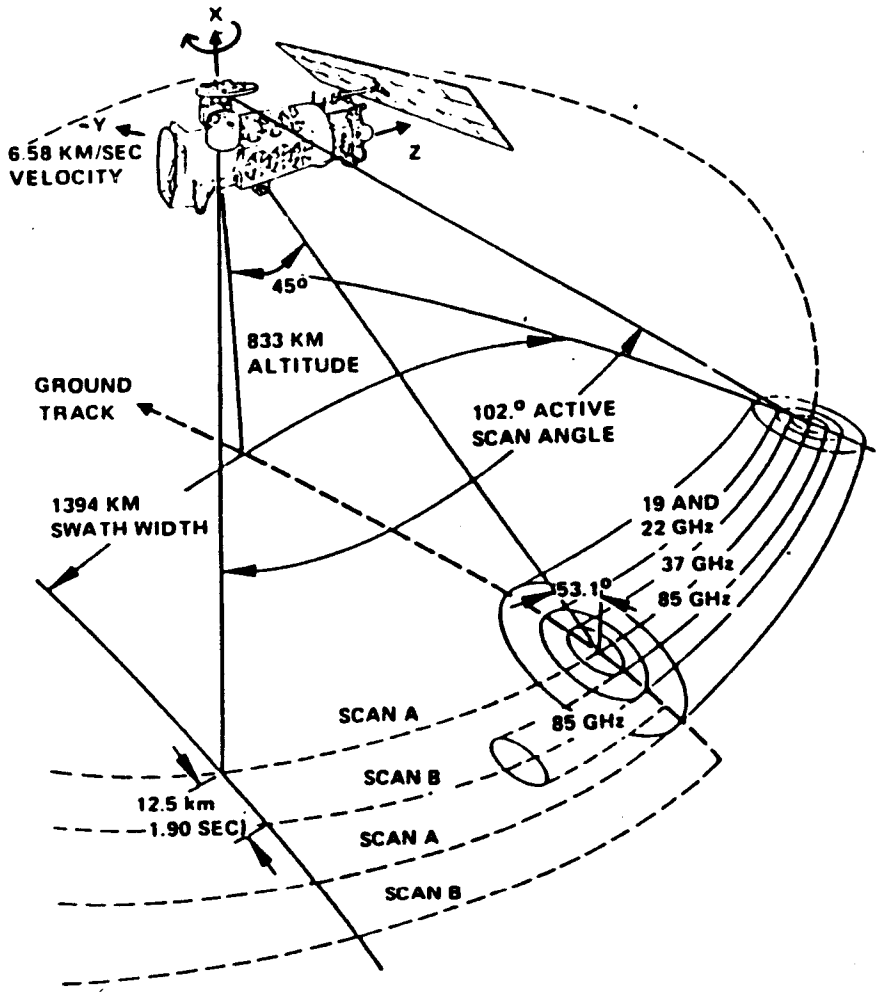

Figure 2.3: SSM/I Scan Geometry from [9].

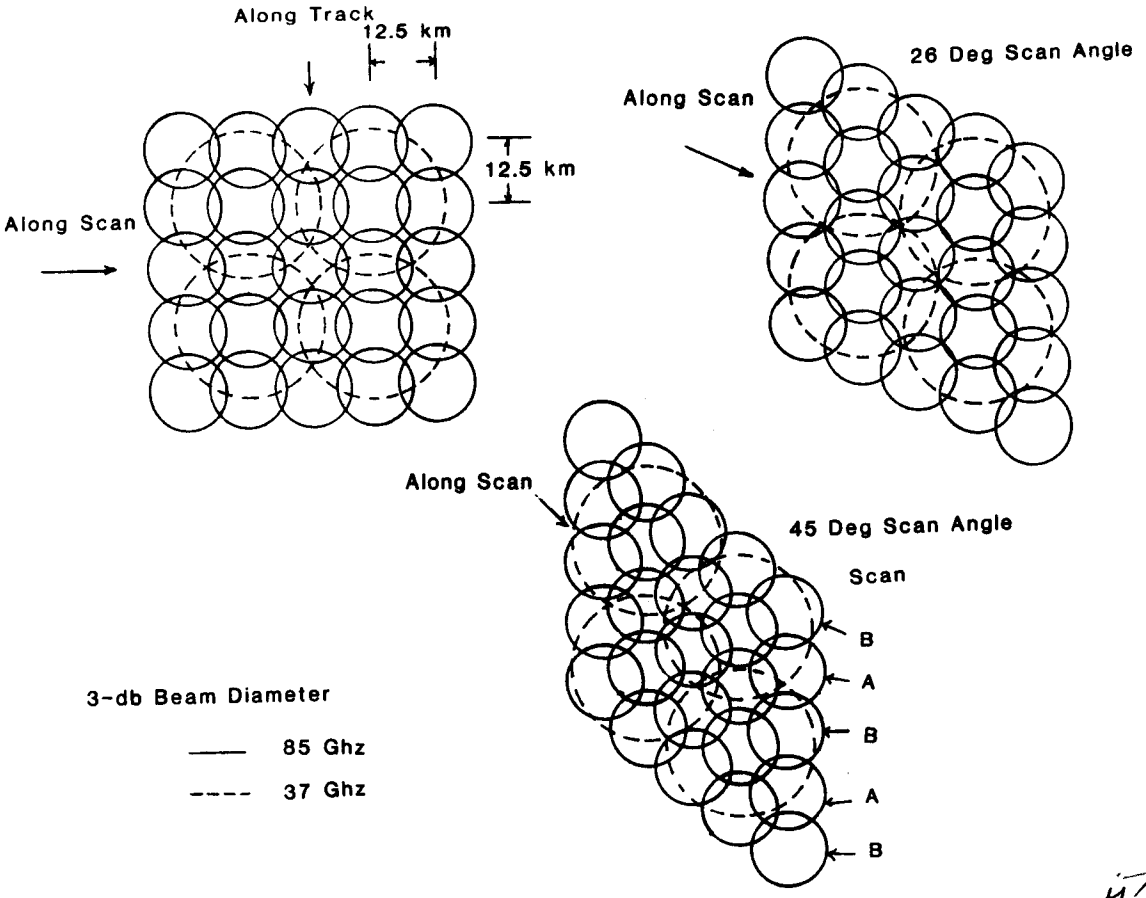

Figure 2.4: SSM/I Antenna Pattern Spatial Sampling from [9]. The upper left group represents the spatial sampling of the midswath measurements and the other groups the spatial sampling of angles from the center of the swath. The A and B scans correspond to the 85 GHz channel.

SSM/I Channel Data				
Channel (GHz)	Pol.	IF Pass. (MHz)	3dB Footprint Along-trk km	3dB Footprint Cross-trk km
19.35	V	10-250	69	43
19.35	H	10-250	69	43
22.235	V	10-250	50	40
37.0	V	100-1000	37	28
37.0	H	100-1000	37	29
85.5	V	100-1500	15	13
85.5	H	100-1500	15	13

Table 2.1: SSM/I Channel Data.

2.5 Description of the Amazon Basin

The SSM/I images in this thesis come from measurements retrieved over the Amazon Basin. This thesis focuses on this area for several reasons. First, previous microwave sensor studies have used the area [5]. Second, the Basin has large areas of densely vegetated land that has little seasonal variation, making the brightness mappings of the area more consistent. Lastly, the scientific community is interested in the Amazon for global warming and deforestation studies.

This thesis defines the geographical area of the Amazon Basin as the area extending from 80° W to 33° W longitude and 24° S to 7° N latitude (see the box in Fig. 2.5). As seen in the map, the area covers Brazil, Bolivia, Peru, Paraguay, as well as parts of Colombia, Venezuela, and Guyana. The majority of the surface consists of rainforest, savanna, and deciduous woodland, thus causing a spatial variance in radiometric brightness. These differences are discussed in more detain in Chapter 5. Some images also come from a subset of this area covering the Amazon Delta. This area is defined by a 15° square region whose Southwest corner is 8° S and 60° W.

2.6 Image Processing

The goal of this work was is to produce high resolution SSM/I images of the Amazon Basin and then analyze them to show their use in geophysical parameter extraction. Before discussing the image reconstruction techniques in the next chapter, it is prudent to review a few concepts about image processing

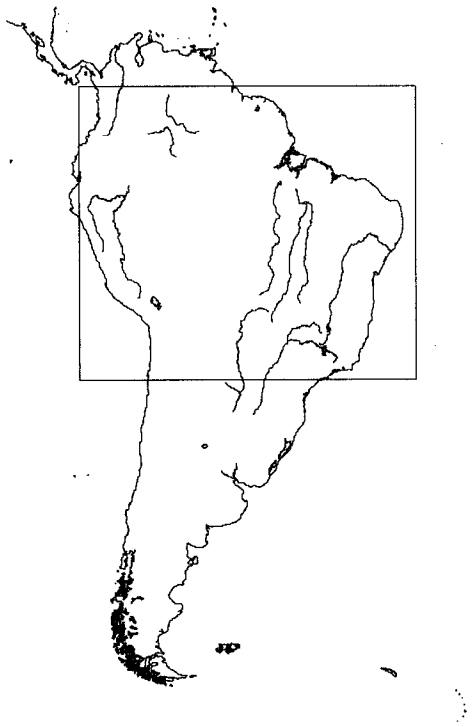

Figure 2.5: Amazon Basin Area: 80° W - 33° W, 24° S - 7° N.

and define the terminology used in this thesis. The terminology and notation will be consistent with image processing texts such as Jain [14].

Images are created from raw data through the process of image reconstruction. I define image reconstruction as the creation of two dimensional images from vector stored brightness temperatures and locations. For example, a simple reconstruction method would simply fill pixels covered by measurements. The resolution is then the size of the measurement footprint. Although other researchers have defined resolution differently [6], I use the more traditional definition that image resolution is the smallest intelligible non-artifact in an image [14]. This research investigated the use of two reconstruction algorithms that achieve better resolution than simple averaging [2, 5].

It is important to note that I did not develop new image reconstruction algorithms but instead attempted to verify and compare the algorithms being used in SSM/I processing (Chapter 3). These images were then used in geophysical research (Chapters 4 and 5) of the Amazon Basin.

CHAPTER 3

SIMULATION COMPARISON BETWEEN THE BGI AND SIR ALGORITHMS

3.1 Introduction

This chapter compares and validates the Backus-Gilbert Inversion method and the Scatterometer Image Reconstruction algorithm applied to radiometric data. The Backus-Gilbert Inversion technique has previously been applied to SSM/I data [7, 8, 15] and the Scatterometer Image Reconstruction algorithm (SIR) has been applied to Seasat Scanning Multichannel Microwave Radiometer data [6]. This chapter applies both algorithms to SSM/I data, thus providing the first comparison of the two algorithms' strengths and weaknesses in reconstructing images from the same microwave instrument. This comparison focuses on characteristics of images from the Amazon Basin, especially feature edge clarity and overall image quality.

Both simulated and actual data sets are used to compare the algorithms. The simulation data set imitates a characteristic background brightness surface of the Amazon Basin. This surface is sampled at approximately the same spatial density as the SSM/I measurements. To improve the simulation, I analyzed both noiseless and noisy simulations using statistical data collected near the Amazon Delta region. To conclude, actual data from the SSM/I was used in each algorithm.

It is found that the two algorithms yield similar resolution images, but that SIR is much more computationally efficient than BGI. SIR is over twenty times faster and requires much smaller input files. SIR is also superior since it does not require user specified parameters to reduce noise as does BGI.

The chapter contains four main sections: a brief discussion of the imaging algorithms, a report of the simulations, an application of the algorithms to SSM/I data over the Amazon Basin, and conclusions derived from the simulation and SSM/I application.

3.2 Description of Imaging Algorithms

Enhanced resolution imaging increases the value of microwave data. Basically, the images aid extraction of geophysical parameters that are hidden in the lower resolution raw data. Resolution enhancement accomplishes this by recovering the sensor information between sample measurement centers. The next sections describe two methods of creating the enhanced resolution images.

3.2.1 The Backus-Gilbert Inversion Method

The Backus-Gilbert Inversion (BGI) algorithm is a correction technique which uses an inversion method for solving integral equations [16]. In this case the algorithm is used to determine surface brightness from integrated, overlapping antenna patterns. Several authors such as Robinson *et al.* [7], Farrar *et al.* [8], and Poe [15] have used this algorithm successfully to adjust the resolution of Special Sensor Microwave/Imager (SSM/I) to either higher or lower resolution for the use of multichannel surface studies. The simulations described in this report qualify these results and compare them to SIR.

The BGI algorithm creates a weighted least squares estimate image. Its basic operation is to retrieve the actual surface/atmosphere brightness temperature from the brightness temperature seen by the radiometric antenna. The algorithm inputs include: the measured antenna brightness temperatures, $T_a(r_i)$; the antenna gain patterns for those measurements, $G(r, r_i)$; and the location of the measurements, r_i. The algorithm then outputs a matrix of pixel values corresponding to an estimate of the actual brightness temperatures, $T_b(r_j)$. The relation between the observed antenna measurements, $T_a(r_i)$, and the actual surface brightness temperature spatial distribution, $T_b(r)$, is found by integrating the antenna pattern over the distribution of surface brightness temperatures, $T_b(r)$, as in the following equation:

$$T_a(r_i) = \int G(r, r_i) T_b(r) dA \tag{3.1}$$

To reconstruct the desired $T_b(r_j)$ values, the algorithm assumes that the actual brightness temperature may be obtained through a linear combination of N nearby

antenna brightness temperatures. That is:

$$T_b(r_j) = \sum_{i=1}^{N} a_i T_a(r_i) \tag{3.2}$$

Combining the equations above yields:

$$T_b(r_j) = \int \left[\sum_{i=1}^{N} a_i G_i(r, r_i) \right] T_b(r) dA \tag{3.3}$$

The solution to the equation may be found if the linear combination coefficients a_i are determined. Unfortunately, given a finite number of samples there is no unique solution. The goal, therefore, is to find the combination of a_i which minimizes error without over-amplifying noise. The solution to this problem is found from a mean square minimization with additional regularization terms included to reduce the noise amplification (the details are in [16]). The solution is:

$$a_i = \mathbf{Z^{-1}} \left[\mathbf{v} \cos\gamma + \mathbf{u} \frac{\mathbf{1 - u^T Z^{-1} v} \cos\gamma}{\mathbf{u^T Z^{-1} u}} \right] \tag{3.4}$$

where

$$\mathbf{u}_i = \int G(r, r_i) dA \tag{3.5}$$

$$\mathbf{v}_i = \int G(r, r_i) \frac{1}{A_i} dA \tag{3.6}$$

$$\mathbf{Z}_{ij} = \mathbf{G}_{ij} \cos\gamma + \omega \Delta T \sin\gamma \delta_{ij} \tag{3.7}$$

$$\mathbf{G}_{ij} = \int G(r, r_i) G(r, r_j) dA \tag{3.8}$$

and γ is a subjectively chosen tuning parameter to control the effect of the noise variance term, $(\Delta T)^2$. The parameter ω makes the two terms of Eq. 3.7 dimensionally compatible. This study uses $\omega = 0.001$ as did the study by Robinson, *et al.* [7]. Further information concerning the algorithm's parameters may be found in [7] and [15].

As implemented in this thesis, another key input to the algorithm is a antenna pattern expansion integer called NSIZE. This parameter increases the number (N) of antenna brightness temperature measurements used in the brightness temperature estimation (See Eq.3.2). If NSIZE equals zero then the predicted brightness of a pixel will be computed using only the measurements whose antenna

patterns overlap the desired pixel. If NSIZE is an integer greater than zero then any measurement which extends within NSIZE pixels of the desired pixel will also be used. In Figure 3.1, the solid line represents the antenna pattern of a measurement which would always be used in the linear combination since it overlaps the desired pixel. The dashed box represents the antenna pattern of a brightness measurement which does not directly overlap the desired pixel, but is included in the linear combination if NSIZE=2 since it lies within two pixels of the desired pixel. (See Figure 3.1.) The NSIZE parameter has a large effect in simulation as will be seen later in this chapter.

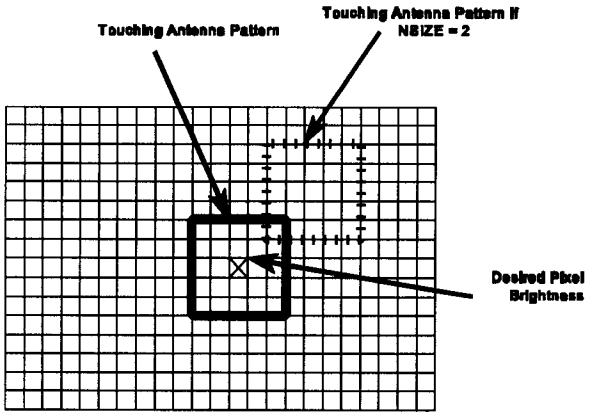

Figure 3.1: Antenna Patterns Included in Linear Combination: Solid Line Always Included, Dashed Line if NSIZE=2.

3.2.2 The SIR Algorithm

The second imaging method used in this thesis is known as the Scatterometer Image Reconstruction algorithm or SIR [17]. The algorithm, originally designed to produce scatterometer images, produces radiometric images by using an iterative procedure and an initial brightness estimate. The procedure is nonlinear and depends on the antenna pattern dimension and shape for its resolution.

The SIR algorithm is a variation of the multiplicative algebraic reconstruction technique (MART), a maximum entropy reconstruction. MART uses a predicted value of brightness temperature of each measurement and compares that

to the actual measurement. A new prediction is then calculated using a scale factor from the ratio of the forward projection and the actual measurement. As iterations continue, the scale factor approaches unity and the pixel value is determined. The detailed derivation for scatterometer data is found in Long *et al.* [5] and its adaptation to radiometer data in Davis [6].

As mentioned in Davis [6], several other options are applied to help stabilize SIR and reduce noise. One of these options is a modified version of SIR known as SIRF. SIRF stands for Scatterometer Image Reconstruction with Filter. As implied in the name, the algorithm is basically the same as the SIR algorithm with the exception of a 3×3 edge preserving filter defined in [6] which is applied between iterations. This filter helps reduce noise effects but also decreases resolution enhancement.

3.3 Simulation

This section describes the simulation used to compare BGI and SIR. First, it describes the simulation image. Second, it outlines the method to generate simulated antenna measurements. Third, non-enhanced images are discussed. Lastly, noise-free and noisy simulation results are presented for BGI and SIR (and SIRF).

3.3.1 The Simulation Brightness Surface

The synthetic simulation image (see Fig. 3.2) is 60×60 pixels in size. The figure has features similar to those seen by radiometric data over the Amazon. The features include a 270 K "river," 295 K "dry spots," and a pyramid-like increasing feature. The background temperature is set at 285 K, similar to the average temperature from raw SSM/I data over the Amazon. The feature sizes are also significant since they are smaller than the artificial antenna pattern used to sample the surface. The next section discusses the antenna pattern.

3.3.2 Noise-Free Simulated Antenna Measurements

Synthetic brightness measurements are extracted from the simulated surface by sampling the surface using an artificial antenna pattern. This antenna

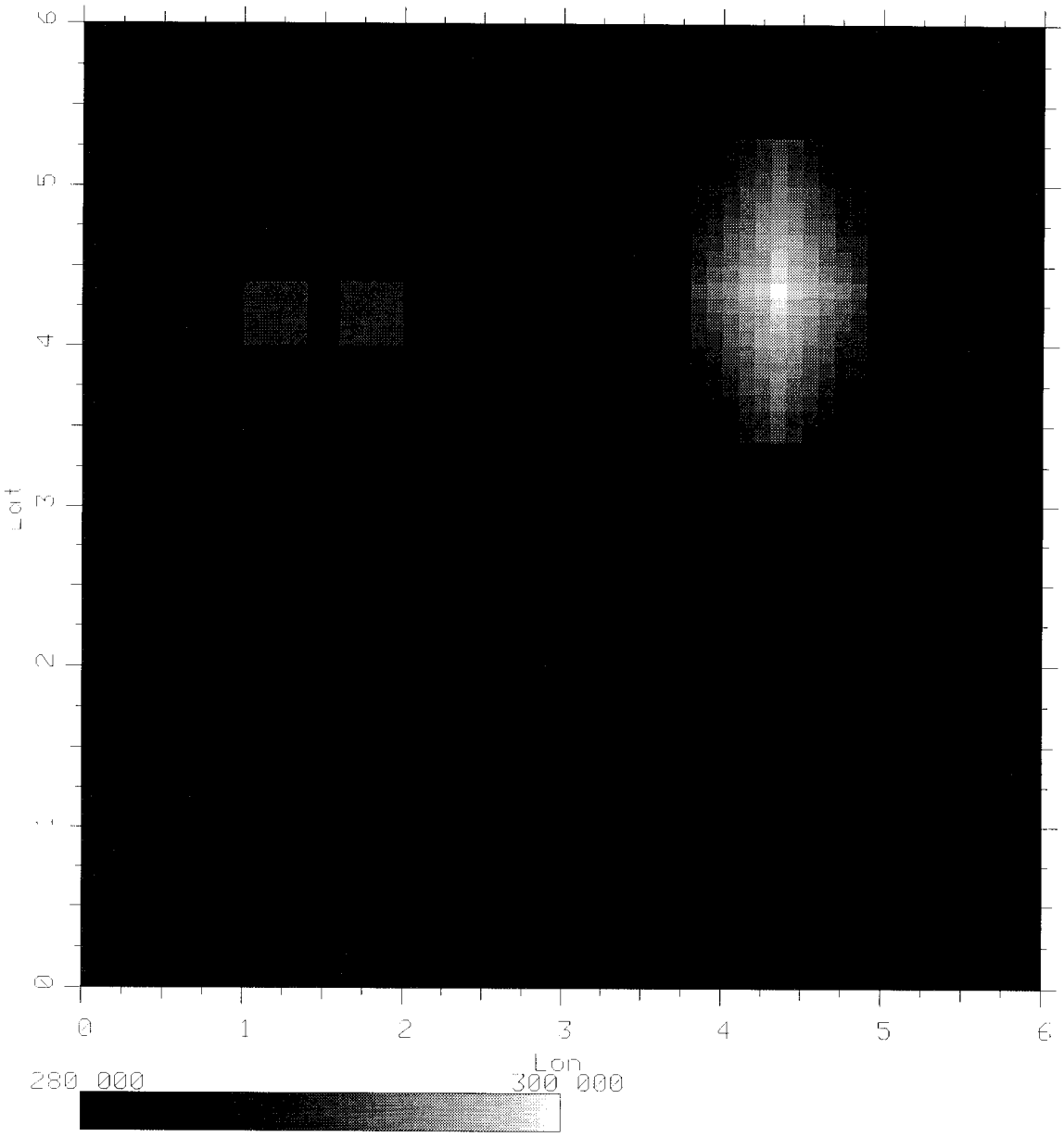

Figure 3.2: Large Simulation Test Image (The Antenna Pattern is Slightly Bigger than One of the Squares in Upper Left Corner).

pattern (Fig. 3.3.2) is a 7×7 pixel grid with a roll off gain in the 5×5 center. The non-normalized pattern gain follows the equation

$$G_{ij} = \frac{640}{2 + \sqrt{i^2 + j^2}} \tag{3.9}$$

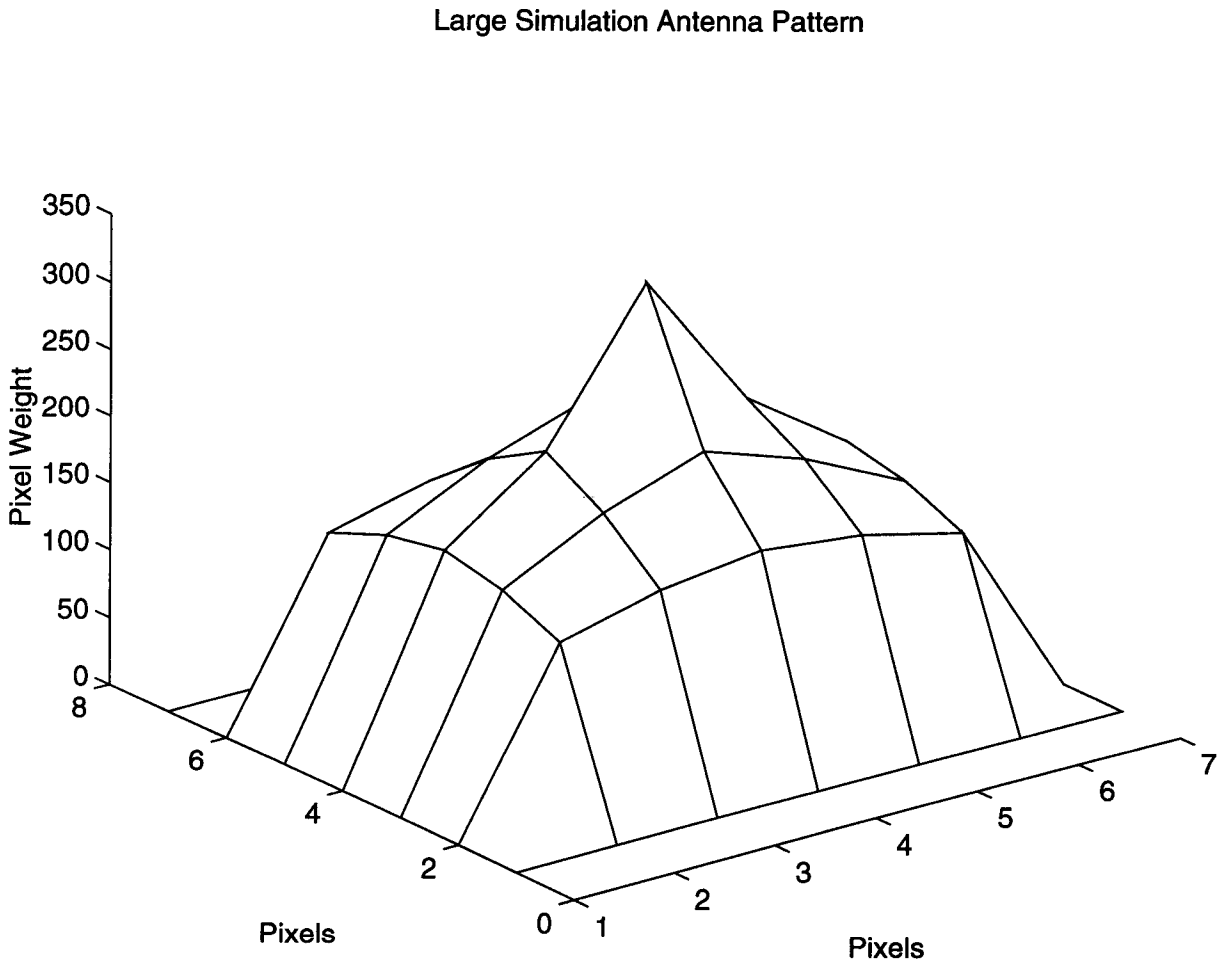

Figure 3.3: Simulated Antenna Pattern for Large Simulation.

where the parameters i and j are the distances in pixels from the center of the antenna pattern.

The simulated measurements are extracted from the simulated surface by shifting the antenna pattern throughout the image and integrating the product of its overlap with the simulated surface (see Eq. 3.1). The sample spatial density

of the synthetic image is set so that only one row of non-zero pixel gains overlap between samples. This is similar to the overlap of SSM/I data [9]. The antenna pattern output samples serve as the noise-free simulation data.

3.3.3 Noisy Simulated Antenna Measurements

Additional simulations include noisy data. The SSM/I has two main sources of noise: instrument noise and atmospheric distortion. Instrument noise is treated in this chapter while Chapter 4 treats the atmospheric distortion. To study the instrument noise, raw SSM/I measurements from a fairly uniform surface background of the Amazon Basin were examined. By using an area with little surface type variation, this study isolates the SSM/I measurement noise from variations caused by spatially changing brightness. Table 3.1 contains the resulting measurement statistics. As one may see, the average brightness temperature is in the mid 280 K range while the standard deviation is generally less than 1 K. The noisy simulation uses 1 K as its standard deviation as a measure of the noise distribution.

Channel	Ave T_b (K)	σ (K)	Max (K)	Min (K)
19.35 GHz V	288.3	1.06	291.5	285.6
19.35 GHz H	287.6	1.05	290.5	284.3
22.23 GHz V	287.0	0.53	290.3	284.0
37.00 GHz V	284.1	0.76	287.0	281.4
37.00 GHz H	283.7	0.91	286.4	280.7
85.50 GHz V	286.2	0.33	289.4	282.5
85.50 GHz H	286.0	0.94	289.4	282.0

Table 3.1: F10 SSM/I Data Summary from $-55°$ to $-52°$ E , 0 to 3° N, September, 1992.

Independent and identically distributed noise is added to the measurement readings by adding a Gaussian random variable with standard deviation of $\Delta T = 1K$ to each simulated antenna power reading. Actual SSM/I data may have noise correlation between adjacent measurements due to atmospheric effects. Atmospheric effects are treated in the following chapter.

3.3.4 Enhanced Resolution Reconstruction

SIR and BGI are called enhanced resolution reconstruction algorithms because they create images with resolution smaller than the raw measurement footprints. *It is important to note that the algorithms do not modify or "enhance" existing low resolution images, but instead reconstruct enhanced resolution images from the raw data.*

To illustrate an image created from the raw measurements without resolution enhancement, Figure 3.4 shows an example of a non-enhanced, noise-free reconstructed image. The smallest features in the reconstructed image are the size of the sensor footprint since the algorithm directly plots the sensor brightness temperature for each measurement. The reader is referred to [17] for an expanded discussion of enhanced and non-enhanced reconstruction.

3.3.5 Noise-Free Simulation Results

The noise-free simulation results for BGI and SIR are given in Figs. 3.5 to 3.8. Overall, both algorithms offer similar results though SIR is subjectively superior in reconstructing the spots of the upper left corner. They both track the course of the dark river and illustrate the "pyramid" pattern of the upper right corner. They each fail, however, to accurately reconstruct the proper width of the river and to clearly detect the "dry" spots in the upper left side. The most obvious difference between SIR and BGI is in their responses to the river's edge. The BGI algorithm tends to cause more high wavenumber artifacts than SIR. These artifacts increase in number as the BGI NSIZE parameter is increased (compare Fig. 3.5 with Fig. 3.7). While these high wavenumber artifacts are undesirable, the higher wavenumber content also seems to aid BGI to a more accurate representation of the "pyramid" pattern. Thus, there is a trade off between SIR and BGI in the number of high wavenumber artifacts vs. the high wavenumber content of the image.

To try to reduce the BGI artifacts, the noise parameter γ is changed from zero to $\pi/4$. The algorithm's noise variance parameter, $(\Delta T)^2$, is set at 1 K and the ω at 0.001 even though the measurements are noise-free. The results are in Figure 3.9. As one may see, the noise parameter has little to no effect when

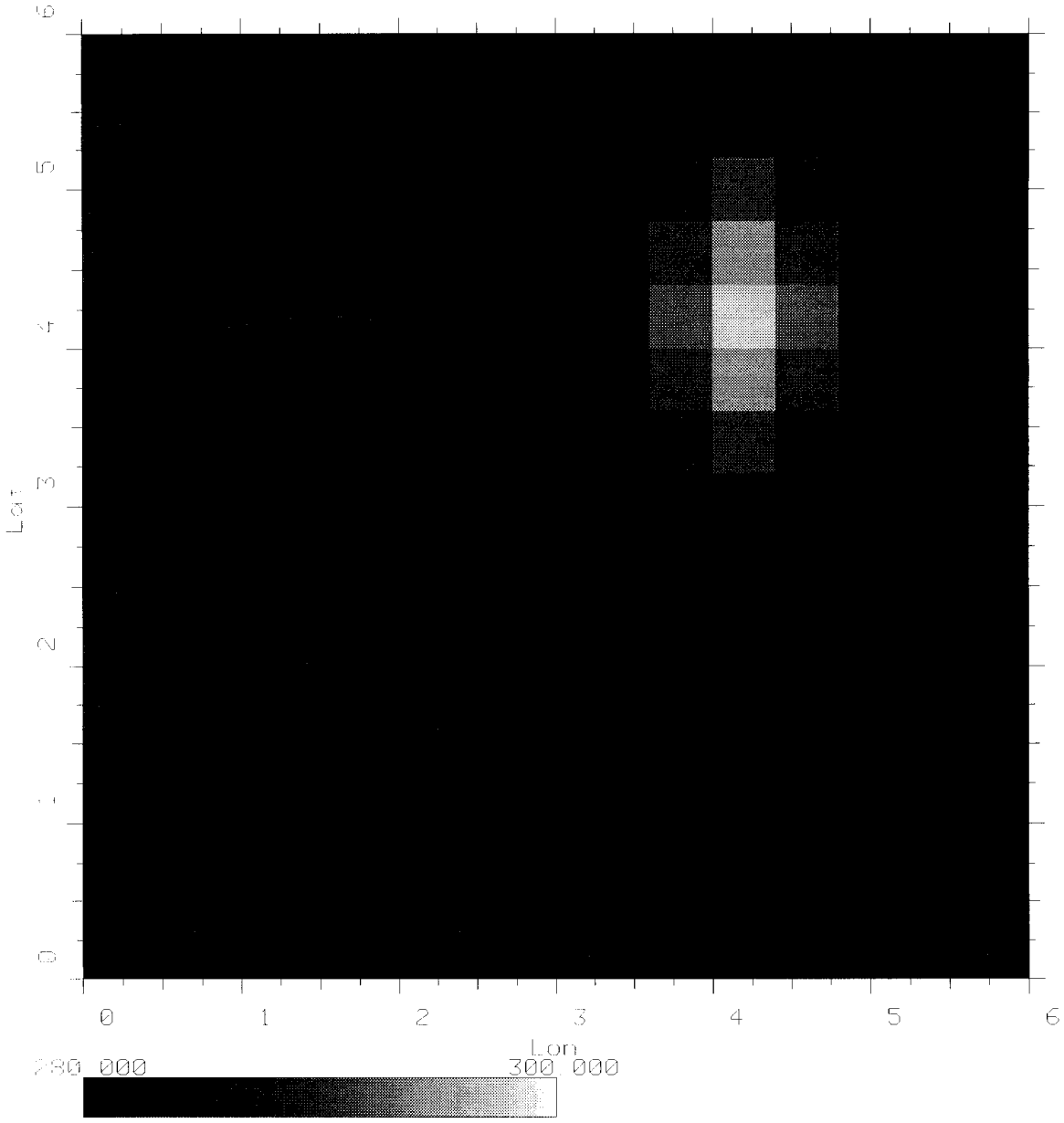

Figure 3.4: Non-Enhanced Reconstruction: Simple Measurement Plotting.

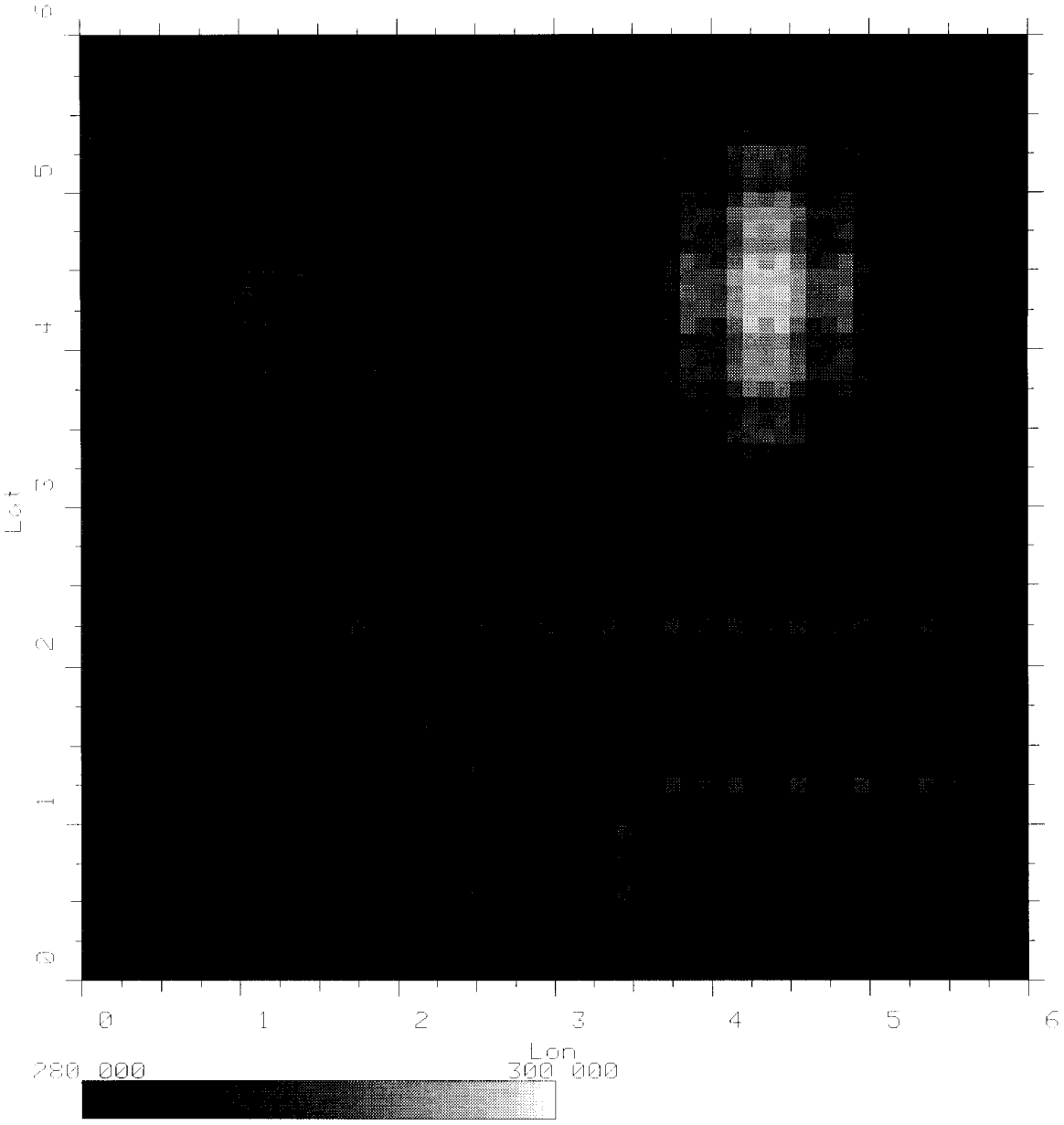

Figure 3.5: Noiseless BGI Results with NSIZE=0.

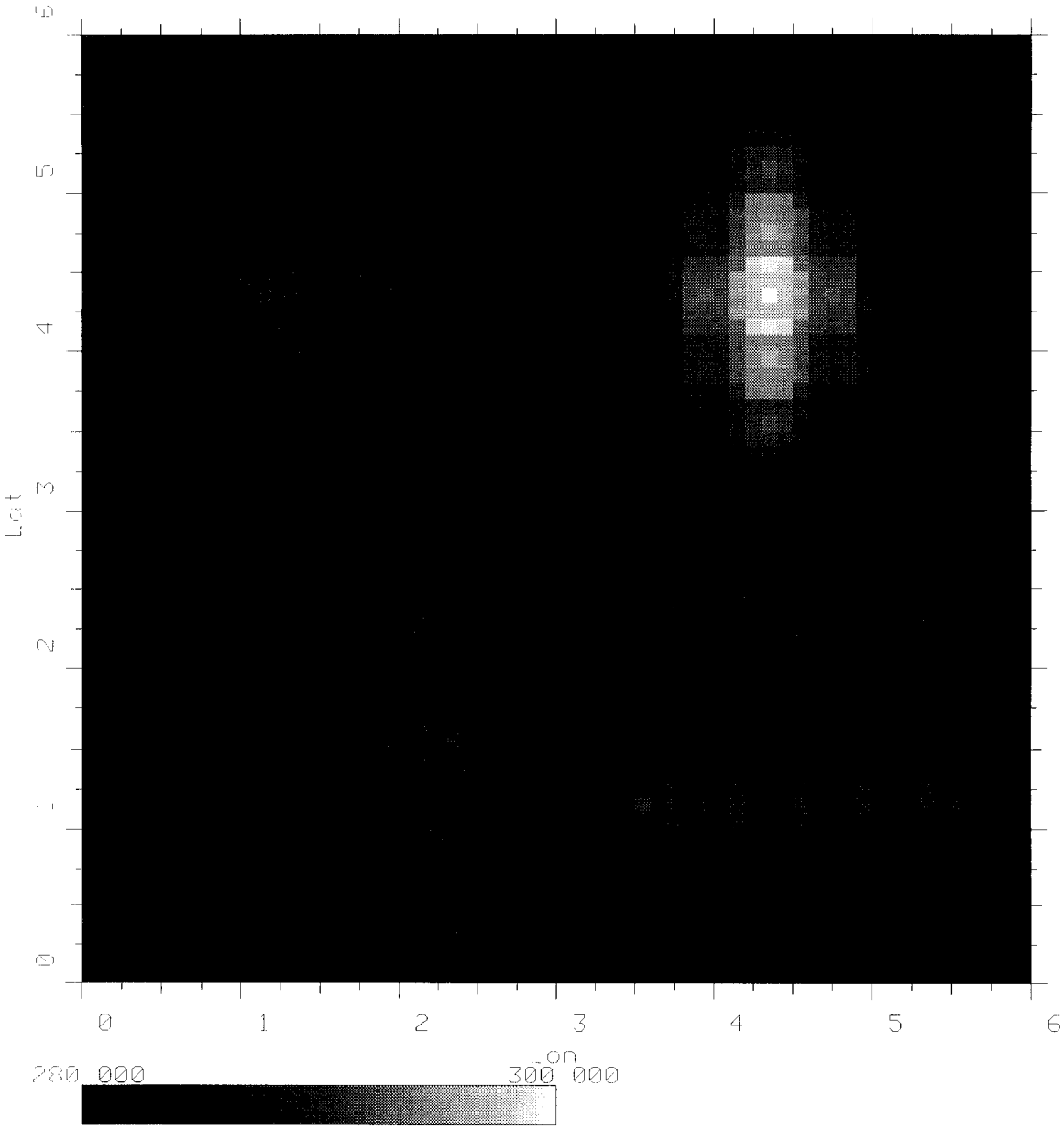

Figure 3.6: Noiseless BGI Results with NSIZE=2.

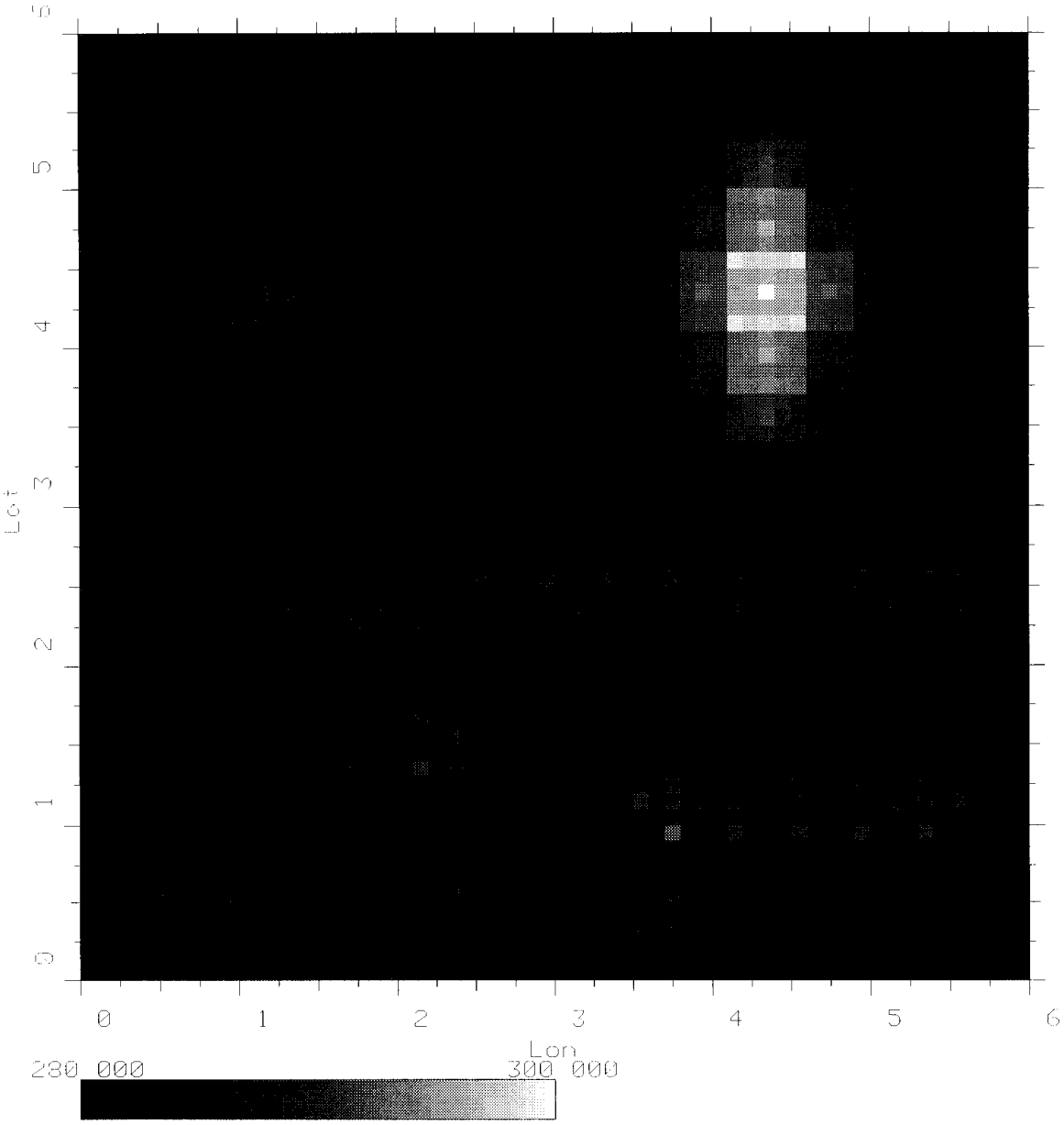

Figure 3.7: Noiseless BGI Results with NSIZE=4.

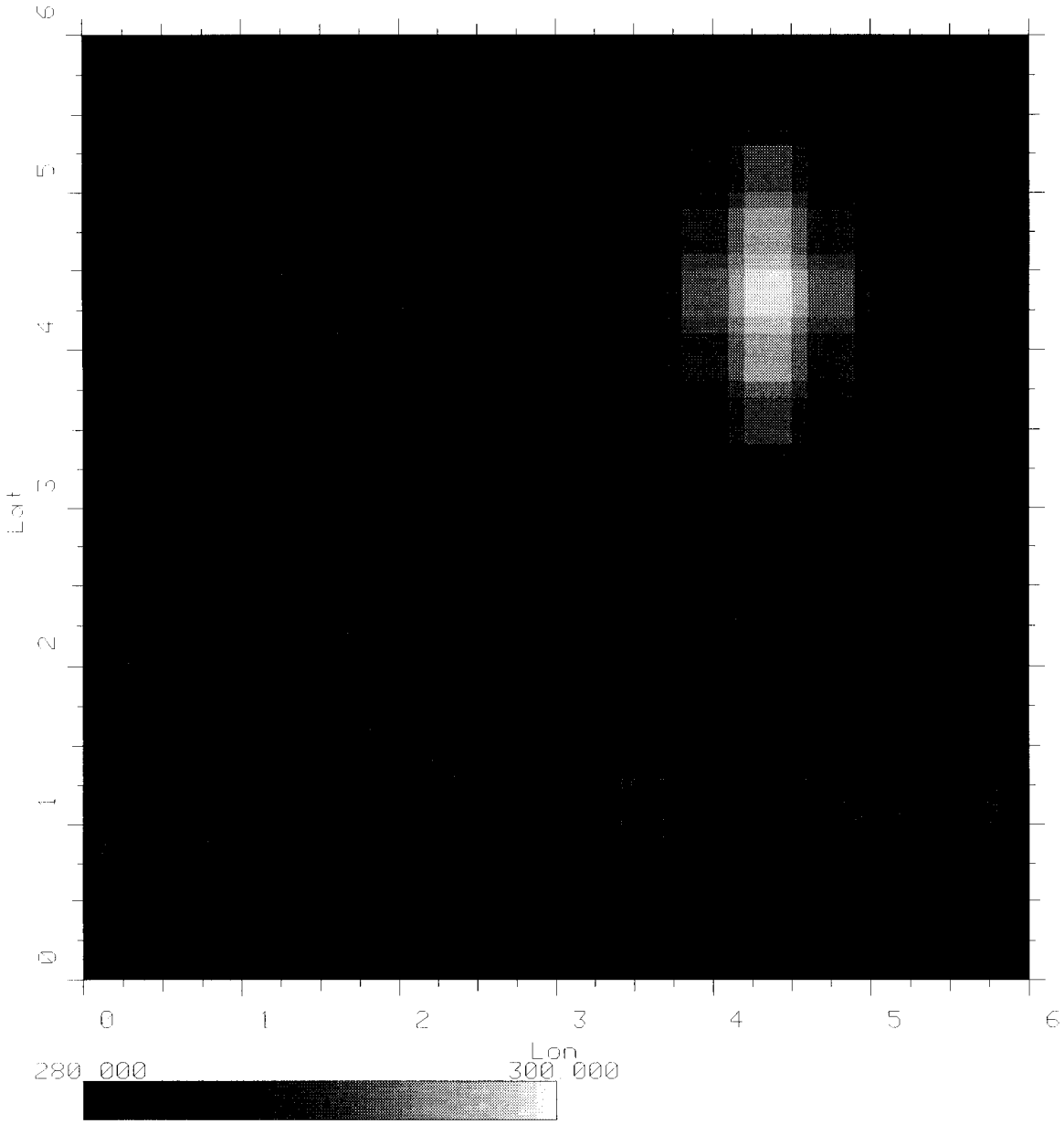

Figure 3.8: Noiseless SIR Results.

operating on noiseless data. Therefore, it is apparent that the high wavenumber artifacts are inherent to the BGI algorithm. Since γ is a noise control parameter, additional simulations on the noise-free data are not performed.

Similarly, to improve the "pyramid" feature with the SIR image, SIRF is applied instead of SIR. Recall that SIRF applies a median filter between iterations so that smoother figures are generated. The result is in Figure 3.10. The resulting image does do a better job in reconstructing a smoother "slope" than the SIR image does. SIRF, however, sacrifices resolution. The resolution decrease is illustrated by the disappearance of the upper left bright spots. The resolution decrease, thus, makes SIRF an inferior algorithm for noise-free data.

To objectively compare the algorithms, consider the tabulated root mean square error (RMSE) between pixel values of the reconstructed images and the truth image (see Table 3.2). This table shows that objectively, SIRF is the best algorithm with SIR as second best. The difference, however, is not large enough to warrant the subjective loss in resolution caused by SIRF. The SIR and BGI errors are nearly equivalent supporting the subjective judgement that the algorithms offer similar resolution.

Root Mean Square Error in Noise-Free Reconstruction			
Algorithm	NSIZE	γ	RMSE (K)
SIR	-	-	2.57
SIRF	-	-	2.49
BGI	0	0	2.72
BGI	2	0	2.60
BGI	4	0	2.61
BGI	0	$\pi/4$	2.70

Table 3.2: Root Mean Square Error Between Noise-Free Reconstructed Images and Truth Synthetic Image.

3.3.6 Noisy Simulation Results

The results of the noisy simulations are found in Figures 3.11 through 3.19. These images are first contrasted to their counterpart noise-free simulation and then compared among reconstruction algorithms.

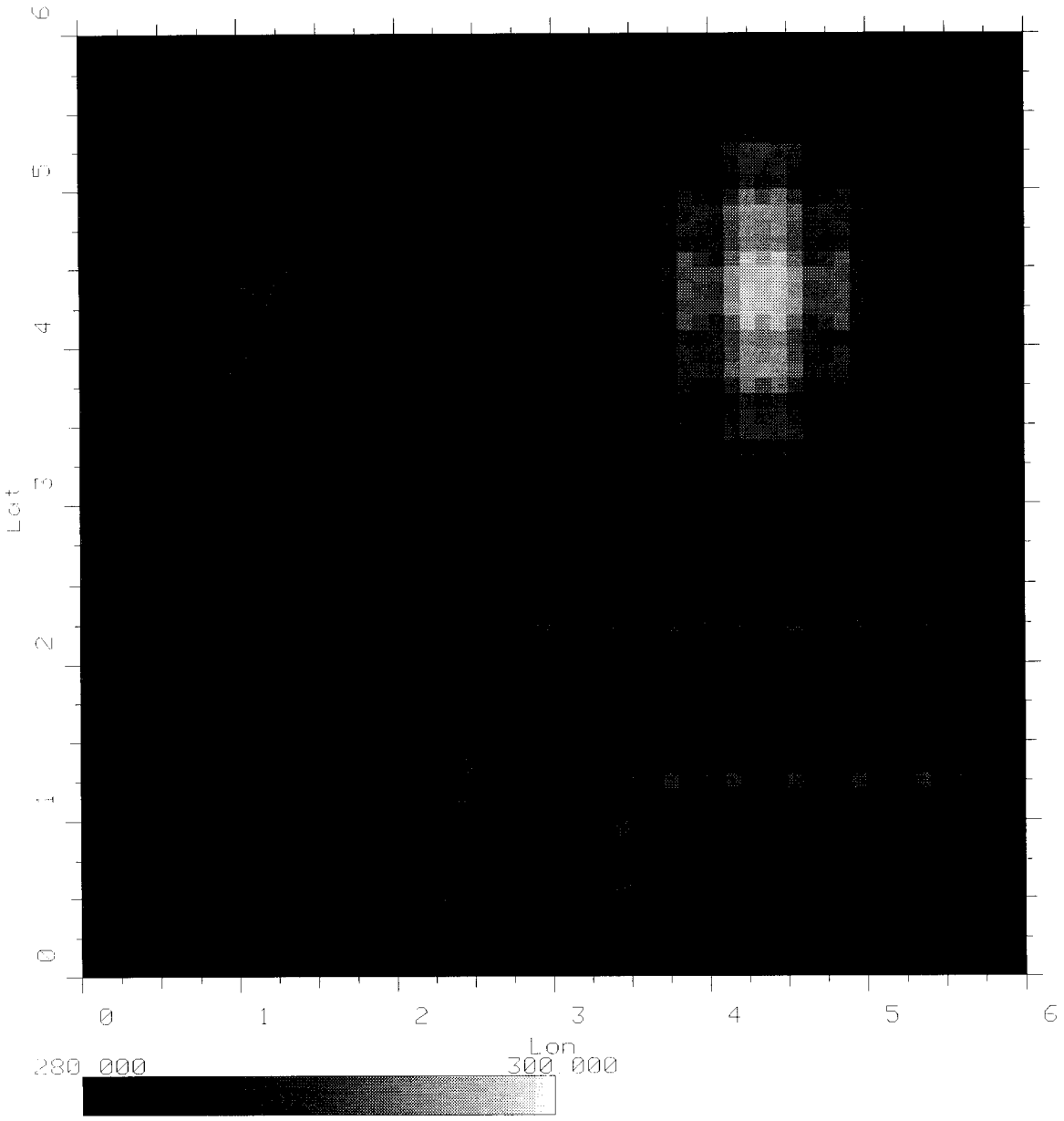

Figure 3.9: Noiseless BGI Results with NSIZE=0 and $\gamma = \pi/4$.

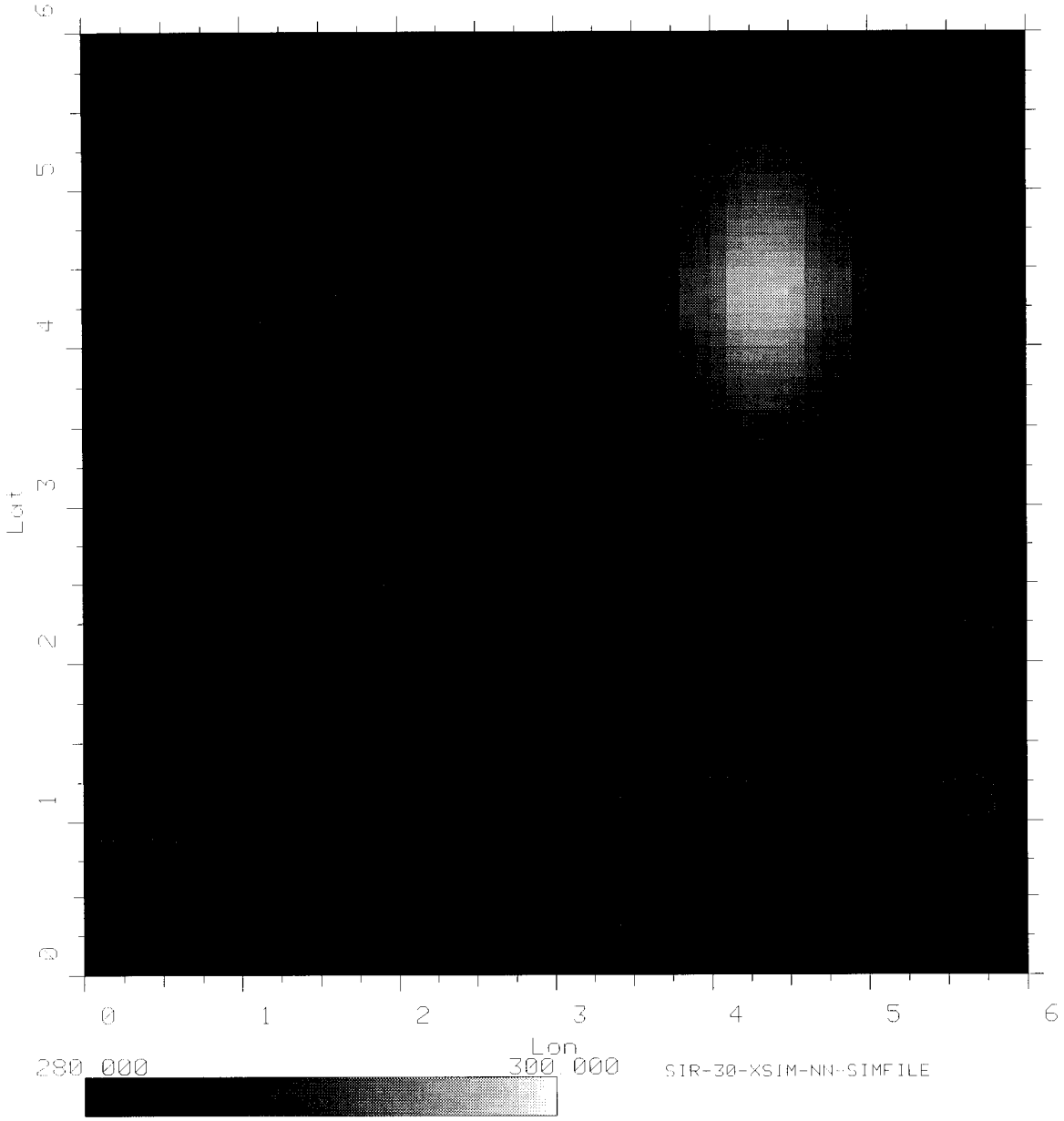

Figure 3.10: Noiseless SIRF Results.

The first three of these images (Figs. 3.11 - 3.13) are noisy reconstruction counterparts of the noise-free simulation images when NSIZE is varied from zero to four (see Figs. 3.5 - 3.7). As in the noise-free simulation, the greater NSIZE parameter tends to increase high wavenumber content. This high wavenumber content, however, is almost negligible compared to the noise level of the image. To decrease the noise level, the noise parameter γ is varied between zero and $\pi/2$. To understand the effect of γ, consider the fact that when it is equal to zero the algorithm takes no action to reduce noise. On the other hand, when $\gamma = \pi/2$ then the algorithm does not try to enhance resolution, but instead simply averages the antenna measurements which "touch" each pixel. The optimal choice of γ depends on the data being used [8] [15] and will not be discussed in this thesis. The results for this simulation are found in Figures 3.14 - 3.17 (all use NSIZE=0). The figures show that the greater γ value decreases noise to a slight degree. The largest change is between $3\pi/8$ and $\pi/2$. This also is the step where resolution decreases the most. Thus, BGI has a large trade off between resolution and noise reduction.

Figures 3.18 and 3.19 contain the noisy results of SIR and SIRF respectively. SIR shows "checker-board" noise. The "checker-board" noise shows that the SIR results depend highly on the spatial-sampling density of the simulation. Since each measurement has only a single pixel overlap with each adjacent measurement, SIR is unable to perform a spatial averaging. The SIRF algorithm is able to perform the averaging but, again, also eliminates any chance of recovering small resolution spots. This is unsatisfactory because the spots may be recovered from an ensemble of enhanced resolution images. The methods to combine images is discussed in Chapter 4.

A comparison of the RMSE between the algorithms indicates that SIRF is the superior method for noisy data (see Table 3.3). The RMSE, however, is nominally the same among all algorithms. Therefore, the images are subjectively classified as having similar resolution.

3.3.7 Computational Differences Between SIR and BGI

Although SIR (SIRF) and BGI offer similar resolution, SIR is computationally less intense than BGI and is, therefore, much faster and uses less memory.

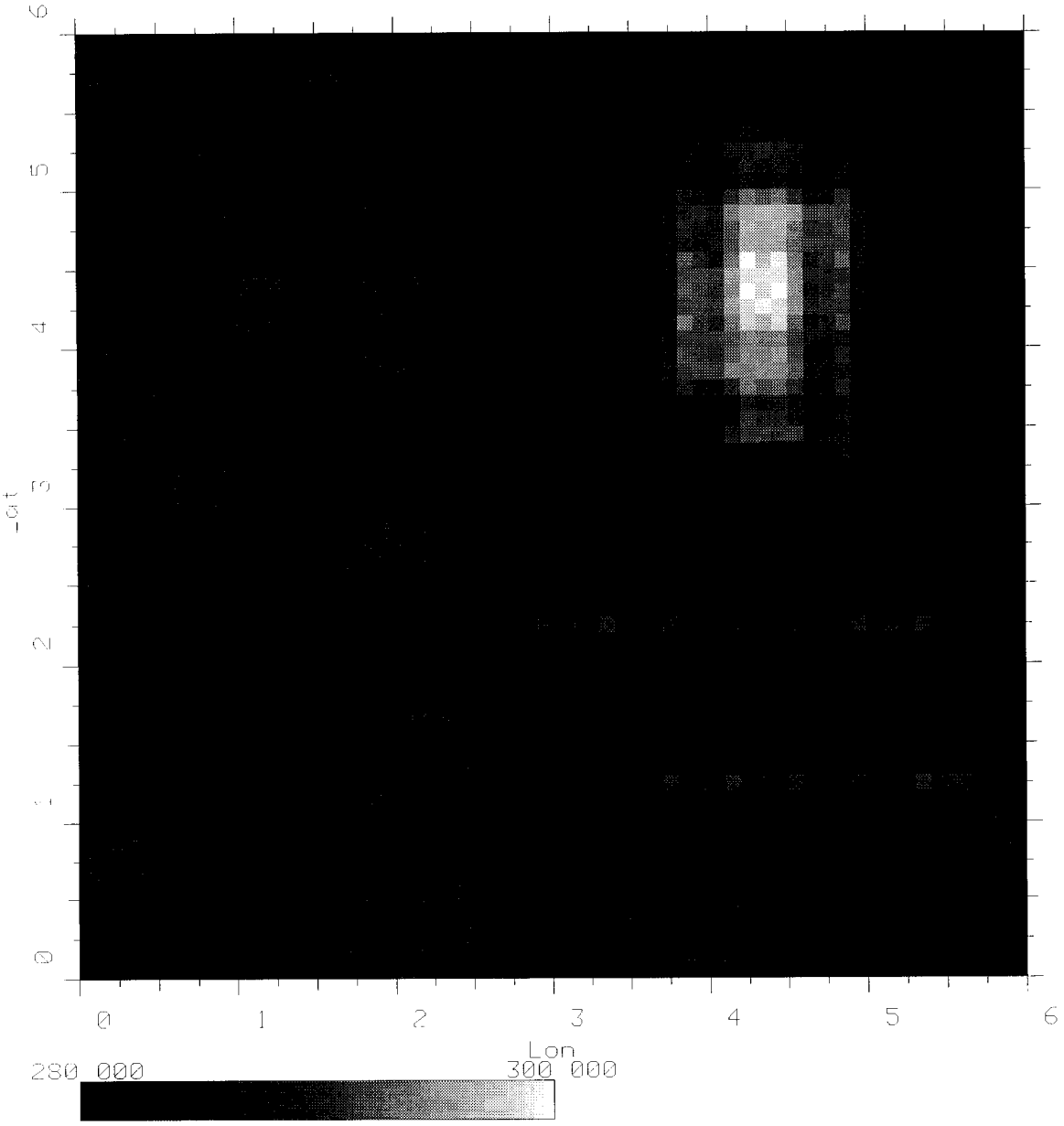

Figure 3.11: Noisy BGI Results with NSIZE=0 and $\gamma = 0$.

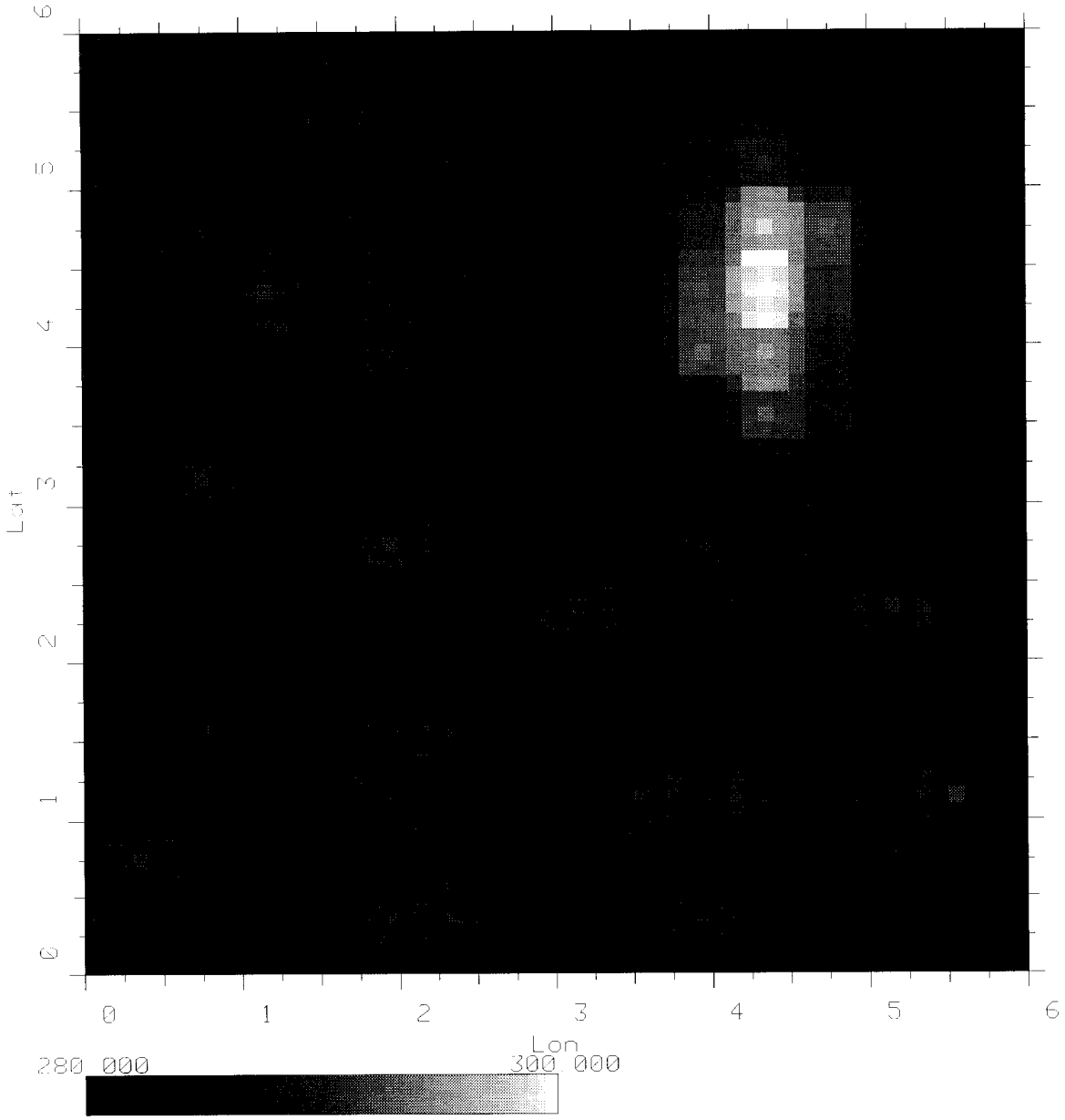

Figure 3.12: Noisy BGI Results with NSIZE=2 and $\gamma = 0$.

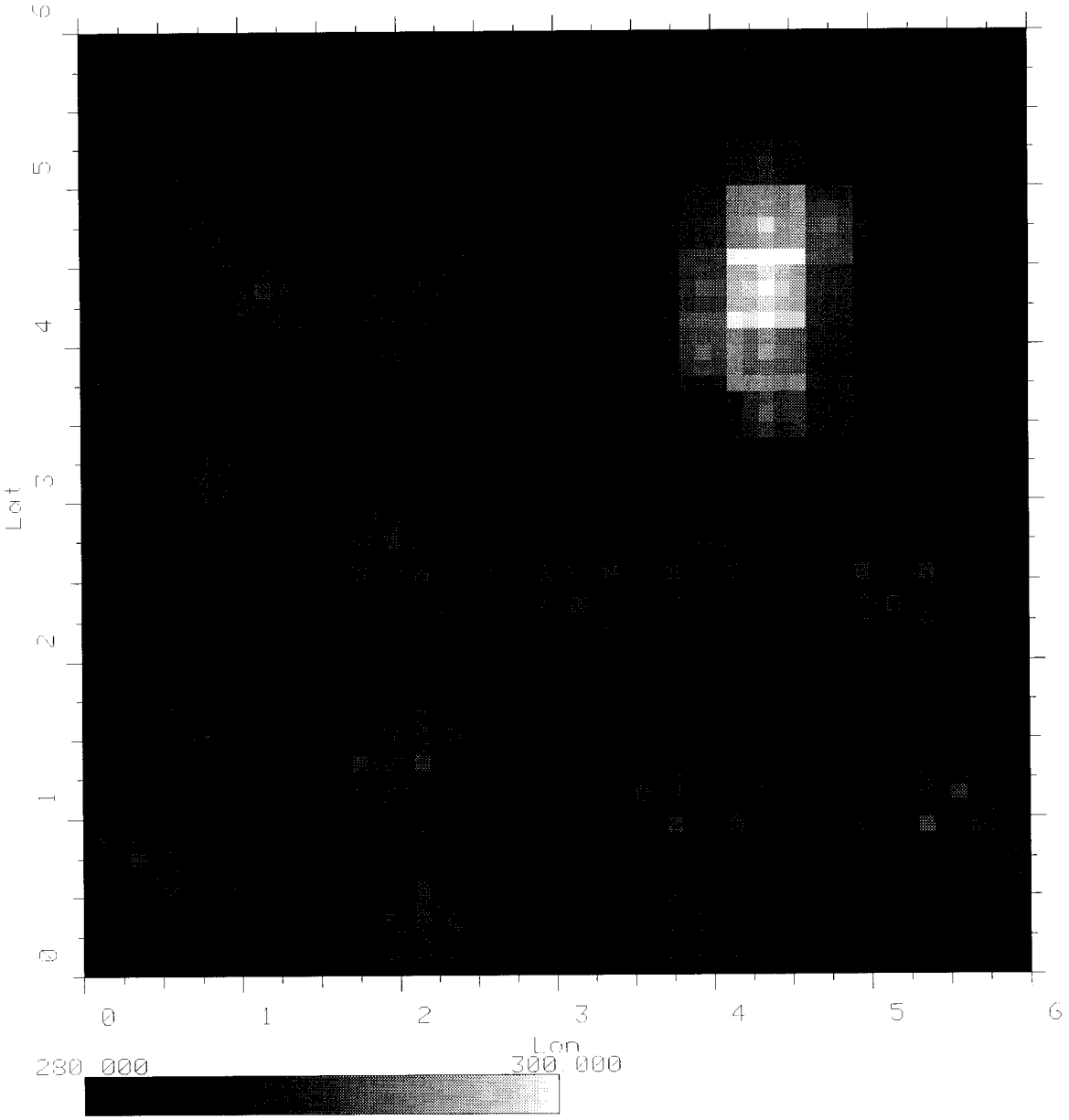

Figure 3.13: Noisy BGI Results with NSIZE=4 and $\gamma = 0$.

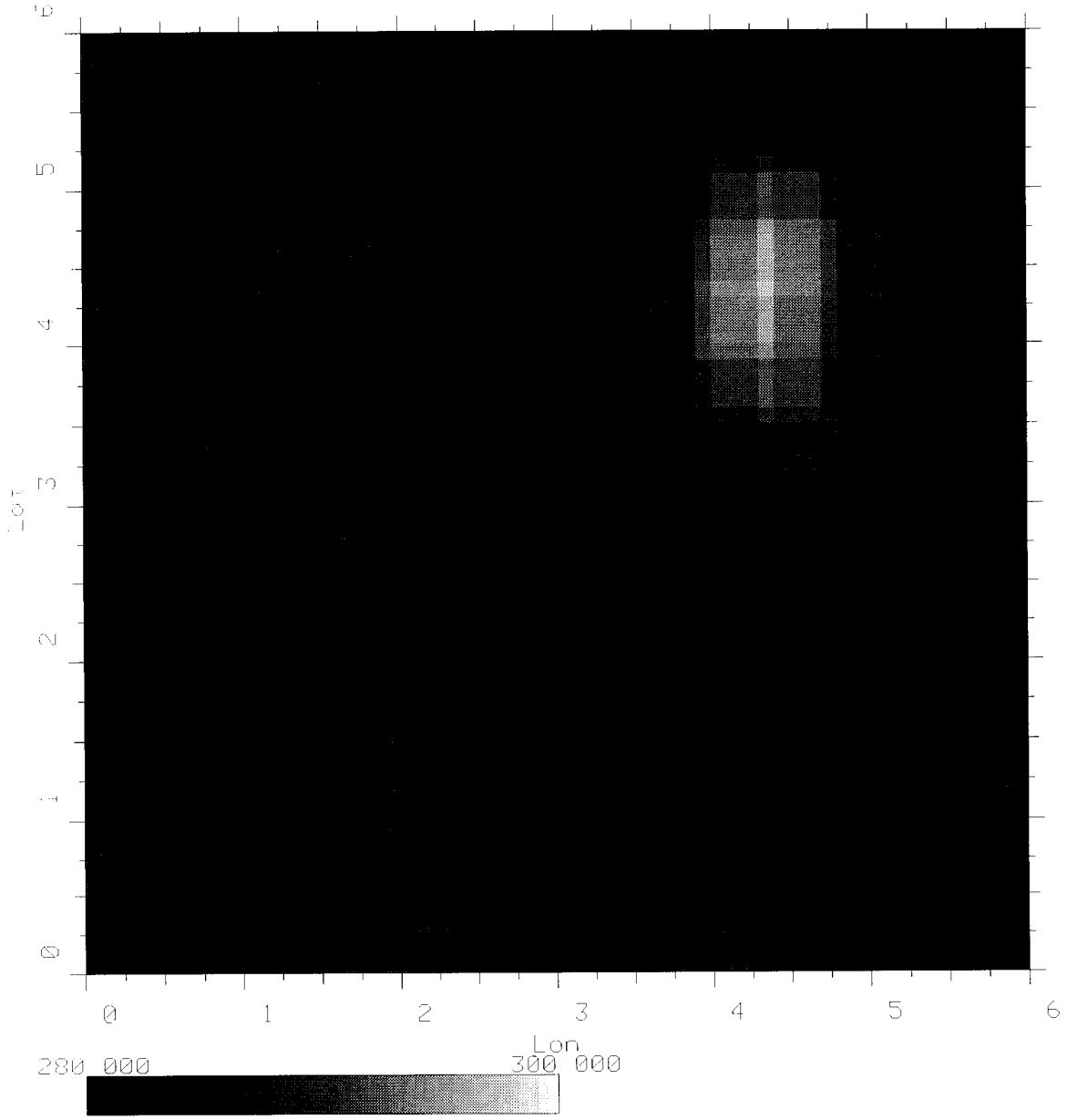

Figure 3.14: Noisy BGI Results with NSIZE=0 and $\gamma = \pi/8$.

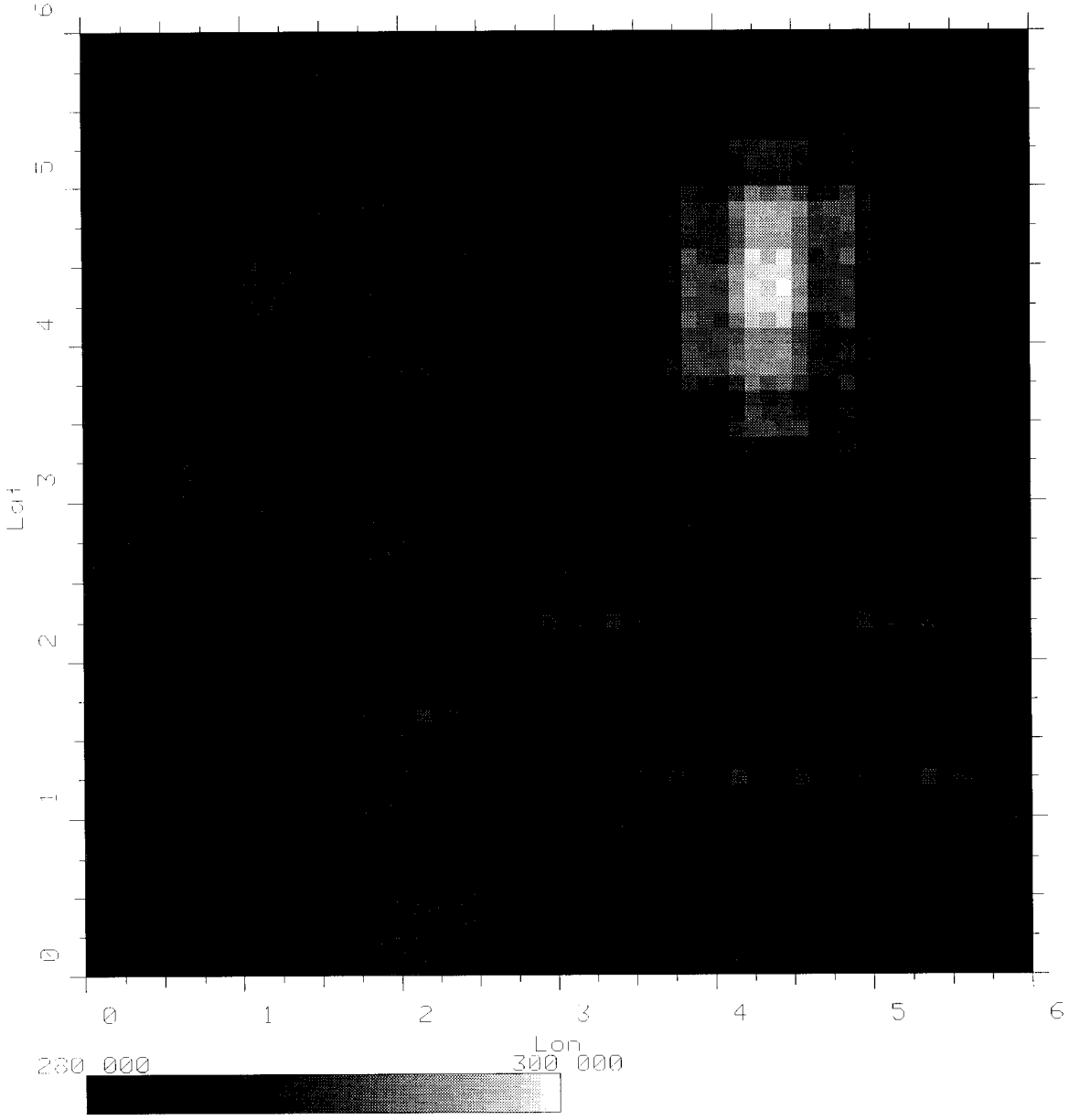

Figure 3.15: Noisy BGI Results with NSIZE=0 and $\gamma = \pi/4$.

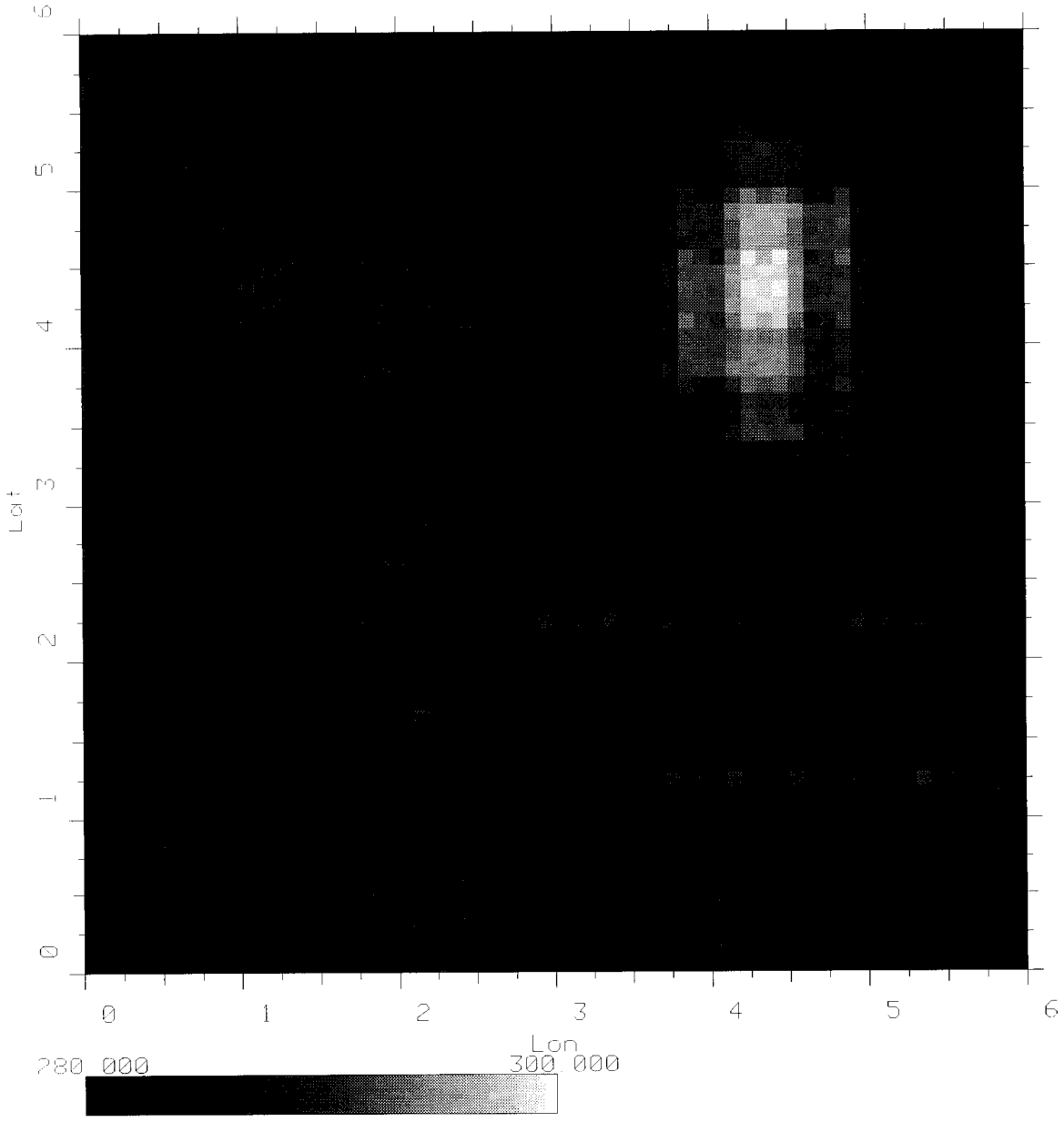

Figure 3.16: Noisy BGI Results with NSIZE=0 and $\gamma = 3\pi/8$.

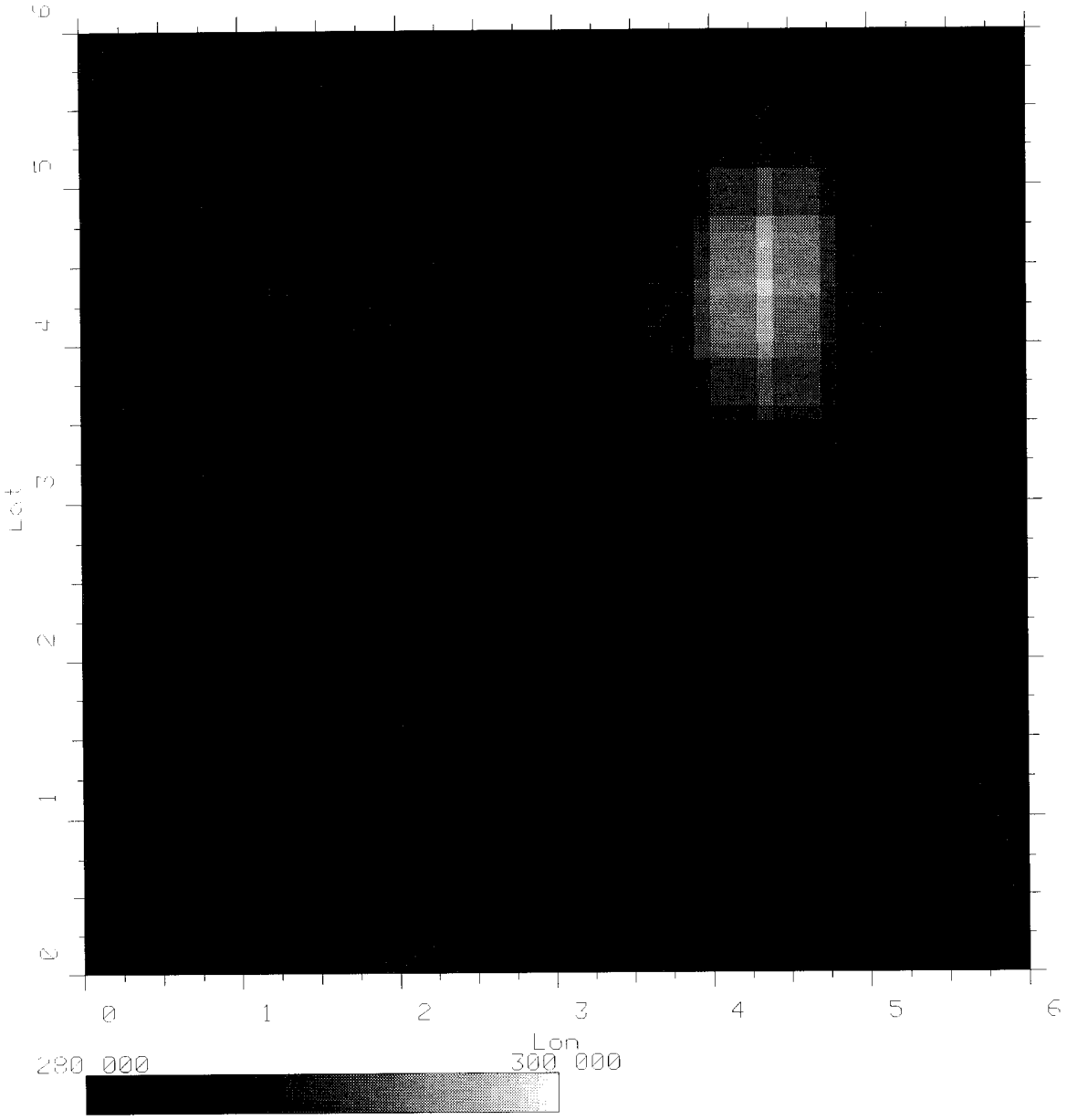

Figure 3.17: Noisy BGI Results with NSIZE=0 and $\gamma = \pi/2$.

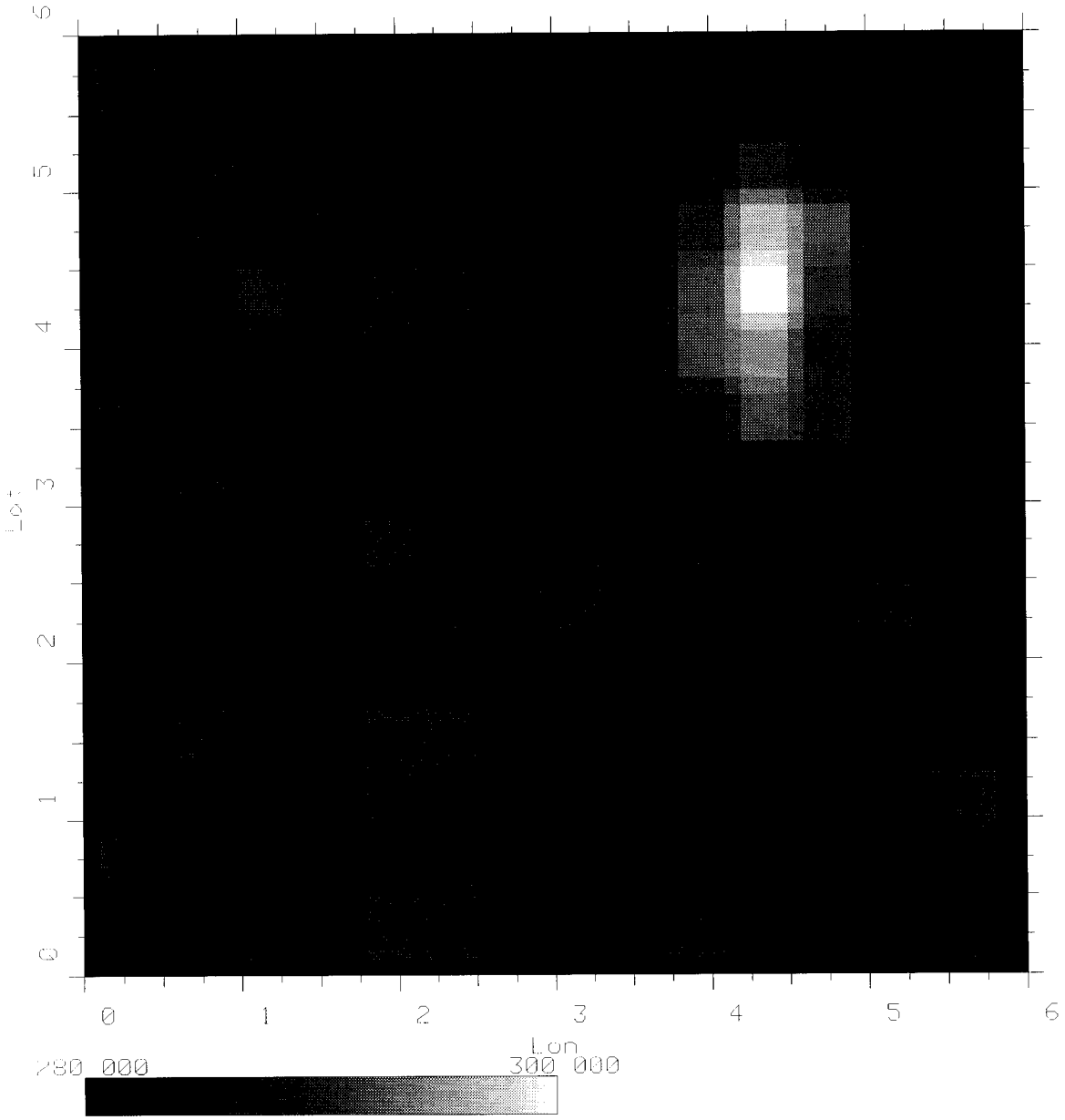

Figure 3.18: Noisy SIR Results.

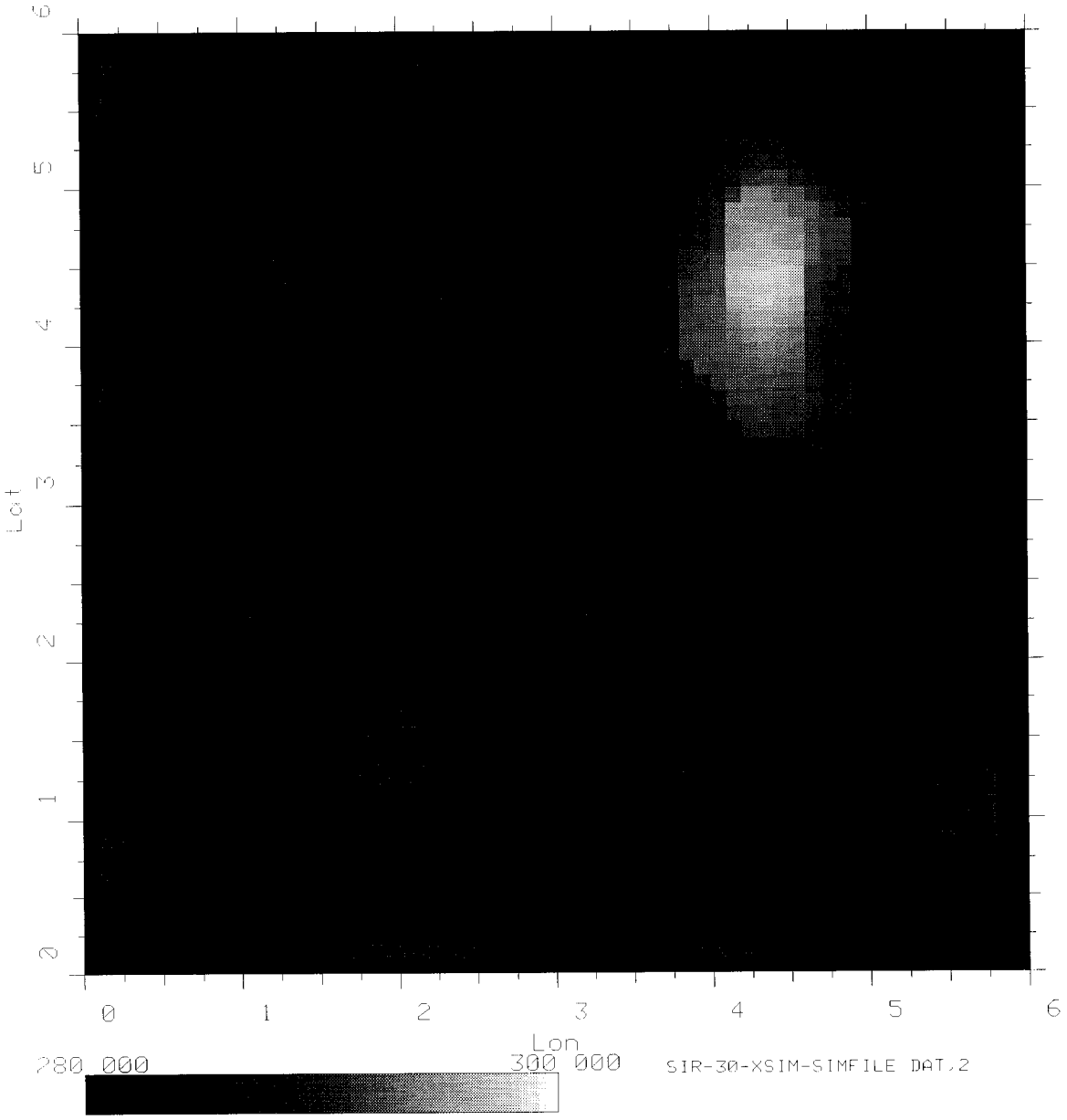

Figure 3.19: Noisy SIRF Results.

Root Mean Square Error in Noisy Reconstruction			
Algorithm	NSIZE	γ	RMSE (K)
SIR	-	-	2.86
SIRF	-	-	2.62
BGI	0	0	2.88
BGI	2	0	2.83
BGI	4	0	2.85
BGI	0	$\pi/8$	2.73
BGI	0	$\pi/4$	2.70
BGI	0	$3\pi/8$	2.84
BGI	0	$\pi/2$	2.73

Table 3.3: Root Mean Square Error Between Noisy Reconstructed Images and Truth Synthetic Image.

For example, a SIR processed simulation image takes about one minute on a VAX workstation. The fastest BGI algorithm (NSIZE=0), on the other hand, takes approximately 30 minutes. The computational difference comes from basic algorithmic approaches. BGI requires matrix inversions for each pixel and, hence, much more CPU time. The processing time becomes very critical for actual data because the images are much larger. In addition, in order to speed BGI up to its present rate, the algorithm uses direct access files which are over twenty times the size of the sequential SIR files.

The other computational difference between the algorithms is their user chosen parameters. While BGI requires subjectively chosen input values for parameters such as NSIZE, γ, and ω, SIR does not require any inputs other than the data. Thus, SIR images are created directly while the user may have to experiment with BGI's parameters by running the algorithm many times to optimize the images. For the reasons stated in this section, SIR (SIRF included) is chosen as the superior reconstruction algorithm.

3.4 SSM/I Images Produced with Backus-Gilbert and SIR

Thus far, simulations have been used to compare BGI and SIR. I now consider actual data. This data from the F10 SSM/I satellite was collected during September, 1992. In this example, the antenna pattern and measurements are

from the low resolution 19 GHz v-pol channel with effective footprints of about $40km \times 60km$. The image area is a $15° \times 15°$ square centered over the Amazon delta. The results of the Backus-Gilbert algorithm for NSIZE equal zero is given in Figure 3.20. The SIR reconstructed image is shown in Figure 3.21. The images are very similar. The BGI image seems a bit smoother but not significantly more. The major difference between the algorithms is processing time. The SIR image takes approximately 15 minutes to process on a VAX workstation while the BGI algorithm requires almost 12 hours. This processing time becomes very crucial when processing very large areas such as the Amazon basin. BGI also requires a much larger file in order to work at its present speed (it requires a formatted direct access file). For example, the input data for the delta BGI image must be preprocessed and stored in a file containing on the order or 40,000 blocks while an equivalent input data for SIR is about 2,000 blocks. Thus the actual data agrees with the simulation results that SIR is the superior algorithm, in a computational load sense, for SSM/I data.

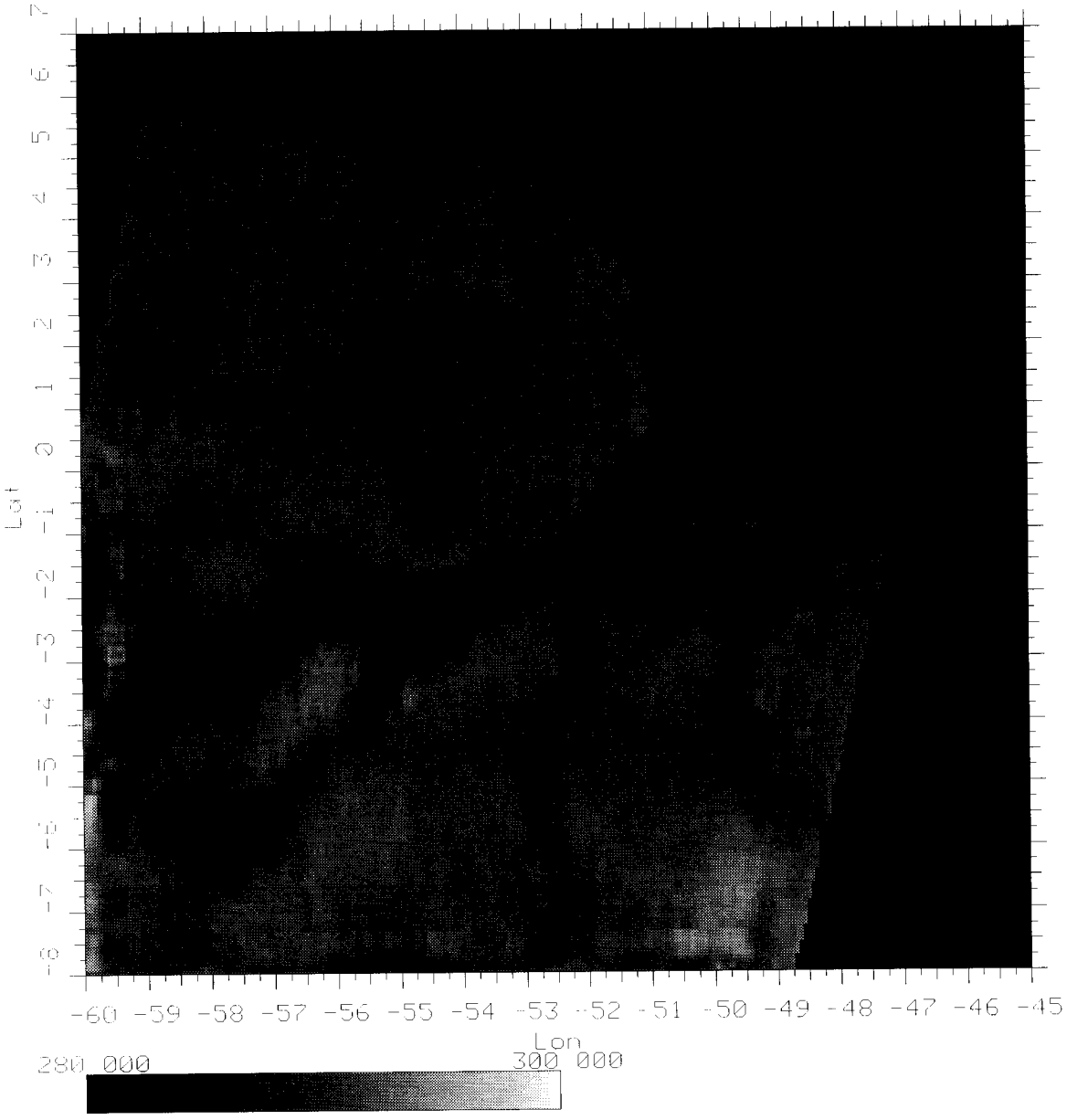

Figure 3.20: BGI Image of Amazon Delta Region with NSIZE=0 and γ=0.

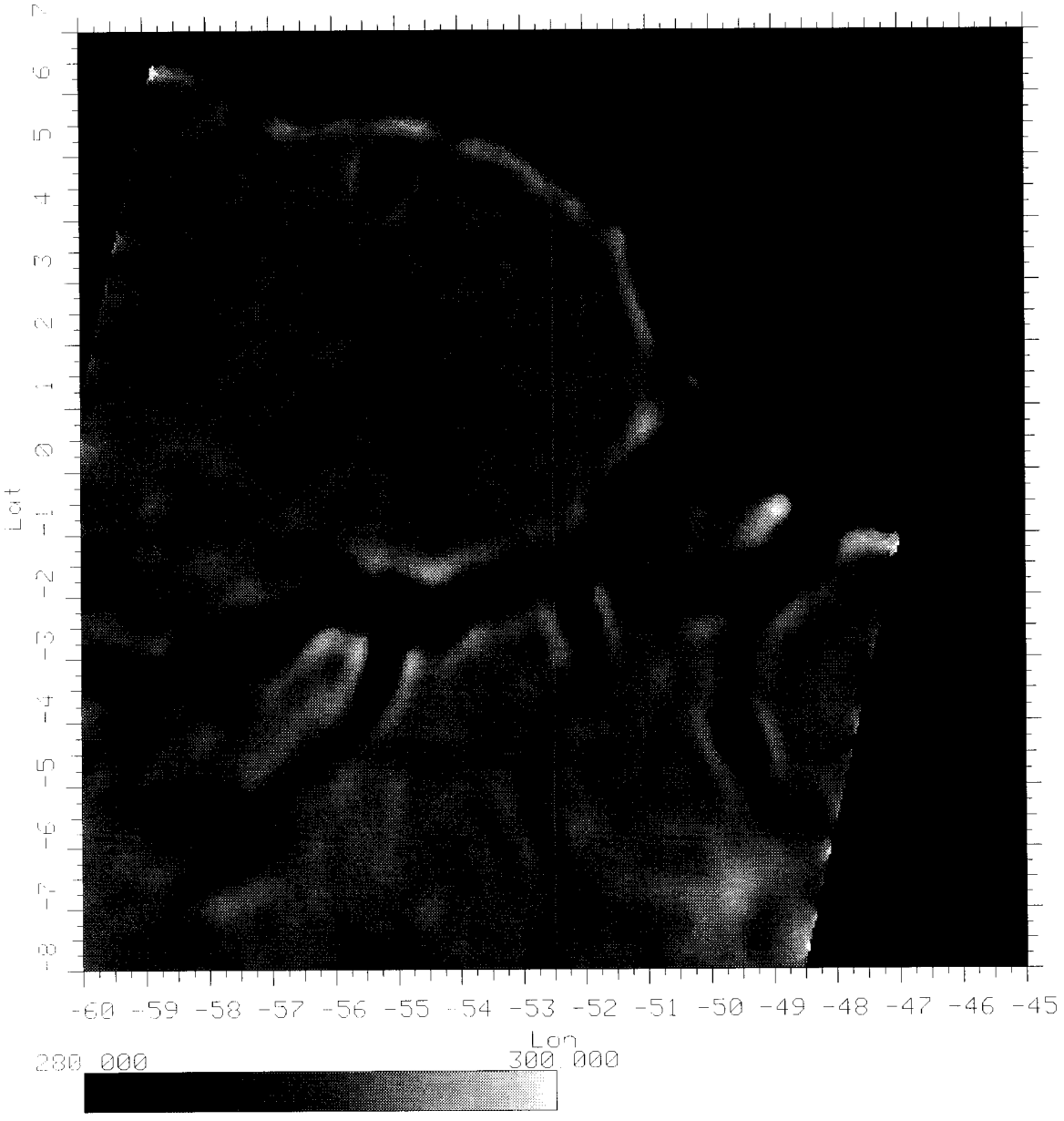

Figure 3.21: SIR Image of Amazon Delta Region.

3.5 Conclusions

This chapter has presented simulations used to compare the performance of the BGI and SIR algorithms. The simulation includes both noise-free and noisy cases. The simulations show that SIR and BGI give comparable resolution results, but that SIR is much more computationally efficient. SIR is chosen as the superior algorithm because it is over twenty times faster, requires input files up to twenty times smaller, and requires no user provided parameters other than sensor data. For those reasons, this thesis uses SIR images for the rest of its image reconstructions and experiments.

CHAPTER 4

SINGLE PASS COMBINATION AND ATMOSPHERIC DISTORTION REMOVAL

4.1 Introduction

One of the challenges in surface mapping the Amazon from microwave radiometer data is atmospheric distortion. Although cloud and rain cause little microwave attenuation for frequencies less than 10 GHz, the higher microwave frequencies of the SSM/I (19.35, 22.235, 37.0, and 85.0 GHZ) show substantial atmospheric loss due to scattering on hydrometeors (rain, ice, etc.) and water vapor. In some studies, especially those over the ocean, this distortion is preferable since cloud water content and particle size may be deduced from the change in brightness. For studies of the Earth's surface, however, these atmospheric effects may prevent the accurate gathering of microwave brightness measurements of the surface.

Clouds and precipitation effect surface brightness measurements in two ways. First, the cloud scattering non-uniformly lowers the measured brightness temperature for all frequencies of the SSM/I, especially the 85 GHz channels. These can be confused with surface features when caused by small-spatial scale clouds. Second, the clouds attenuate the polarization differences caused by the geometrical or chemical composition of different surface types. This prevents the surface polarization difference from being used to discriminate between vegetation types (i.e. rainforest and savanna) or standing water. Thus, the ability to perform surface mappings is reduced by atmospheric distortion.

In this chapter we investigate several objective methods to regain the utility of SSM/I images over land by producing enhanced resolution surface mappings without the atmospheric anomalies. From these methods, an algorithm called the Modified Maximum Average is chosen as superior. This method is capable of removing small-scale temporal effects from SSM/I images by combining multiple images from the same SSM/I channel. Cold atmospheric distortions are removed

from the ensemble by windowing, thus enabling the technique to generate a set of "base" images which describe the surface brightness without cloud interference. These "base" images are used in the next chapter to extract geophysical data about vegetation types in the Amazon.

This chapter contains the following: 1) a discussion of the atmospheric effects in single pass images, 2) a description of the geographical area imaged, 3) the development of the objective atmospheric distortion removal technique, and 4) a presentation of a background mapping to be used in a vegetation discrimination experiment considered in the next chapter.

4.2 Atmospheric Effects in Single Pass Images

SSM/I images are able to detect small-spatial scale, temporal atmospheric distortions over the Amazon Basin. These correspond to moving clouds or precipitation areas less than 1000 km wide. The distortions appear as cool spots in the SSM/I data. Spencer, *et al.* [11] explain that the cold measurement distortions over land come from scattering off of hydrometeors. Although one theoretically could track the clouds crossing the Amazon Basin with the SSM/I data, the SSM/I does not provide adequate spatial and temporal coverage to track clouds (same area coverage is available only every 2-3 days). The distortions appear, therefore, as random artifacts in a time series of images over the same geographical area. These artifacts are now discussed.

Figure 4.1 contains several SIR processed images of the Amazon Delta from September, 1992. These images are generated from 19 GHz v-pol measurements from local hours of 8-11 AM. The images differ in two ways. First, there is a small brightness difference between each image generated by the sensor noise level. These differences are small and are spread throughout the images. The second difference comes from the atmospheric effects. Figure 4.2 contains the same images but with white boxes indicating some of these effects. Although the 19 GHz channel is the least sensitive frequency of the SSM/I, the dark blotches on the images indicate temporal, localized changes in brightness. These blotches are initially predicted to be clouds, rain, or standing water. Standing water, however, causes a large difference between horizontal and vertical polarization of the 19

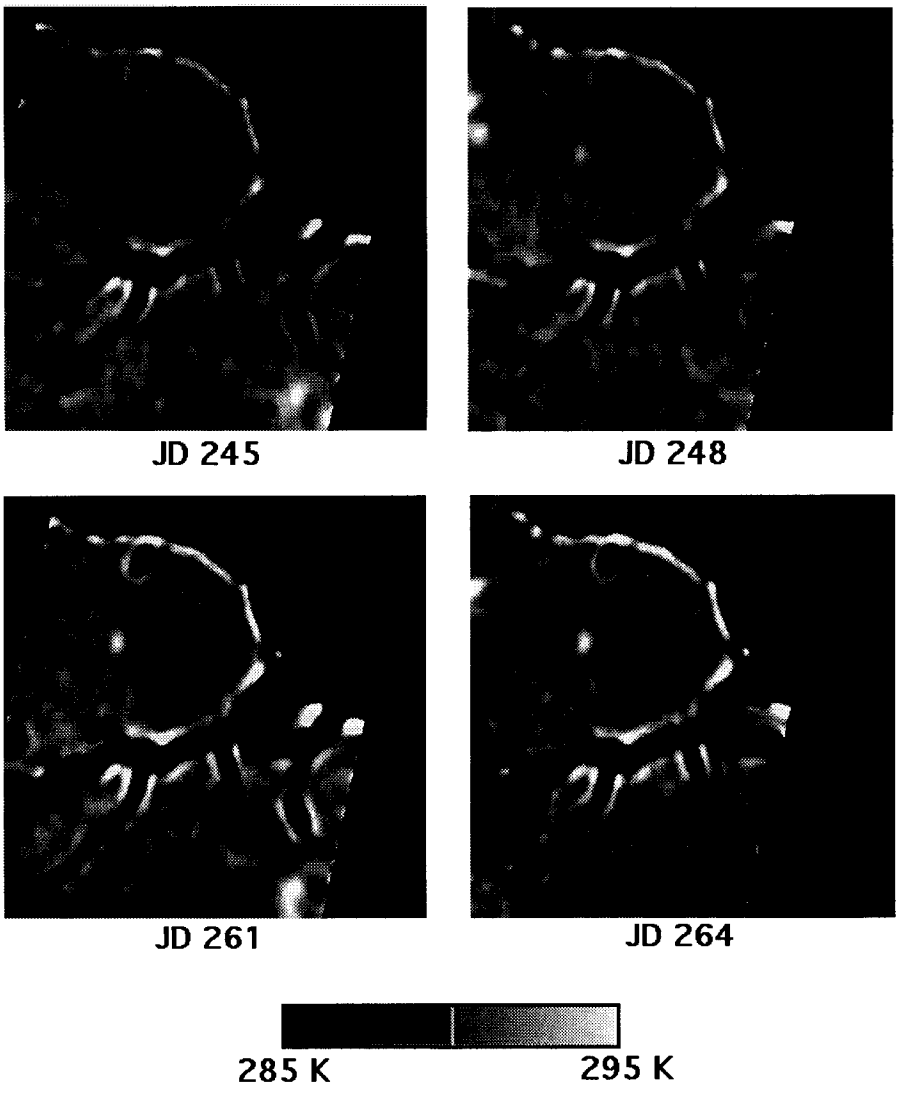

Figure 4.1: SSM/I Images of the Amazon Delta.

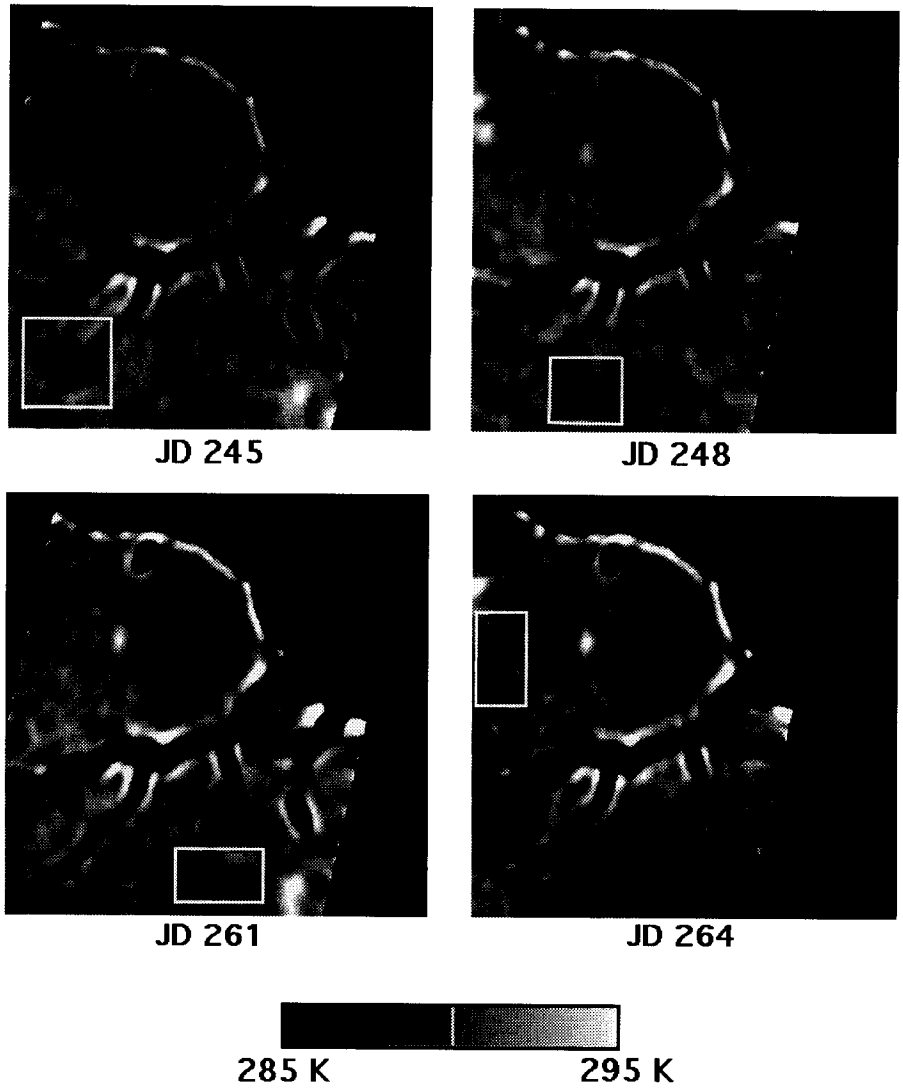

Figure 4.2: Same Images as Previous Figure with Boxes Surrounding Examples of Atmospheric Distortion.

GHz channels. Difference images between the two polarizations do not indicate any dominant polarization so it is assumed that the distortions can not be caused by standing water. Thus, the cools spots are likely caused by rain or clouds.

The next sections of this chapter will discuss various methods to remove these atmospheric effects from single pass images. To give the reader a peremptory understanding of the results, consider an image generated from the method called the Modified Maximum Average (See Fig. 4.3). Although the composite image resolution is the same as the single pass images, the clouds indicated in Figure 4.2 are not present in the composite image. It also lowers the noise level between the single day images. The composite image, therefore, is much more valuable as a tool to perform radiometric studies of the Amazon surface.

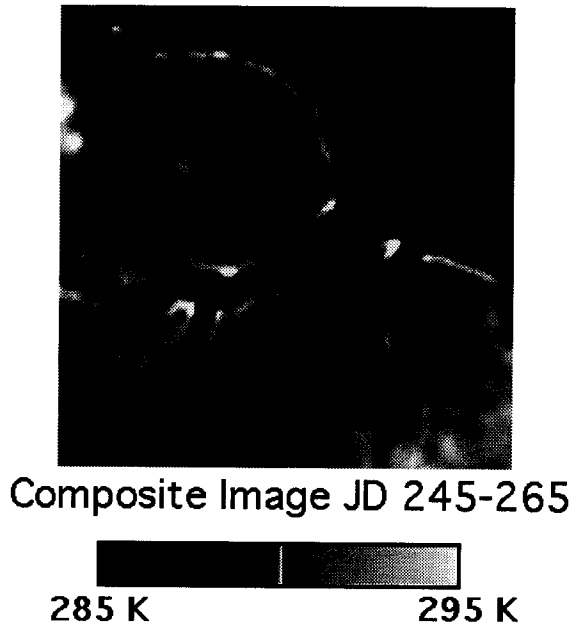

Figure 4.3: Example of Composite "Base" Image with No Atmospheric Distortion.

4.3 Techniques to Combine Images and Remove Atmospheric Effects

The previous chapter investigated methods to reconstruct images from SSM/I data. These images indicate temporally changing brightness measurements caused by clouds and precipitation. This section presents and compares several

methods to remove these atmospheric scattering effects from single pass images (i.e., Figure 4.1). These methods generate "composite" images of the Amazon surface which are less contaminated by atmospheric distortion. While most current research has sought multi-channel algorithms to accomplish this task [12, 18, 19, 11], this research only uses enhanced resolution images from the same microwave channel. By only using single frequency information, these methods generate composite images of the geographical area for each channel of the SSM/I without causing additional correlation between channels. The less correlated images are more useful for geophysical research since more variation exists (see Chapter 5). The image combination algorithms rely, however, on the assumption that surface brightness variation over an area is only caused by small-scale, temporal atmospheric distortions rather than changing surface brightness. This condition is satisfied by the consistent vegetation of the Amazon. Composite images can also reduce measurement noise from the frequency ensemble without decreasing resolution.

The question, therefore, is: What is the best way to produce an enhanced resolution composite image without atmospheric distortion? To address this question, this thesis reports on several techniques such as SIR processing of all data, ensemble averaging, windowed averaging, second highest value choosing [20], and modified maximum averaging [21]. While all of these methods are described later in this chapter, the modified maximum average is chosen as the best method to remove atmospheric effects.

SSM/I data from the first fifteen days of September are used to investigate the techniques previously mentioned. For most of the techniques, the data is first SIR reconstructed to give single-pass images of the Amazon Basin similar to the Delta images of Figure 4.1. These images offer an ensemble of 5-10 pixel values for each geographical location in the image. Larger ensembles of pixel values may be obtained by using a longer time period, but then there is a greater risk of contamination by seasonal changes in surface brightness. Thus, a half month period of passes was used. The techniques were tested in two ways. First, each technique's composite image from the high resolution data of the 85 GHz v-pol channel was studied. Second, the techniques were simulated and compared using synthetic data.

4.3.1 SIR Processing of All Data

This technique is distinct from the other techniques because it combines different pass data and uses the SIR algorithm to process all of the data into a single image. This is the easiest method to produce multipass images since the input is simply the raw data supplied to SIR. The resulting image for the 85 GHz v-pol channel is found in Figure 4.4. As seen in the figure, the main weakness

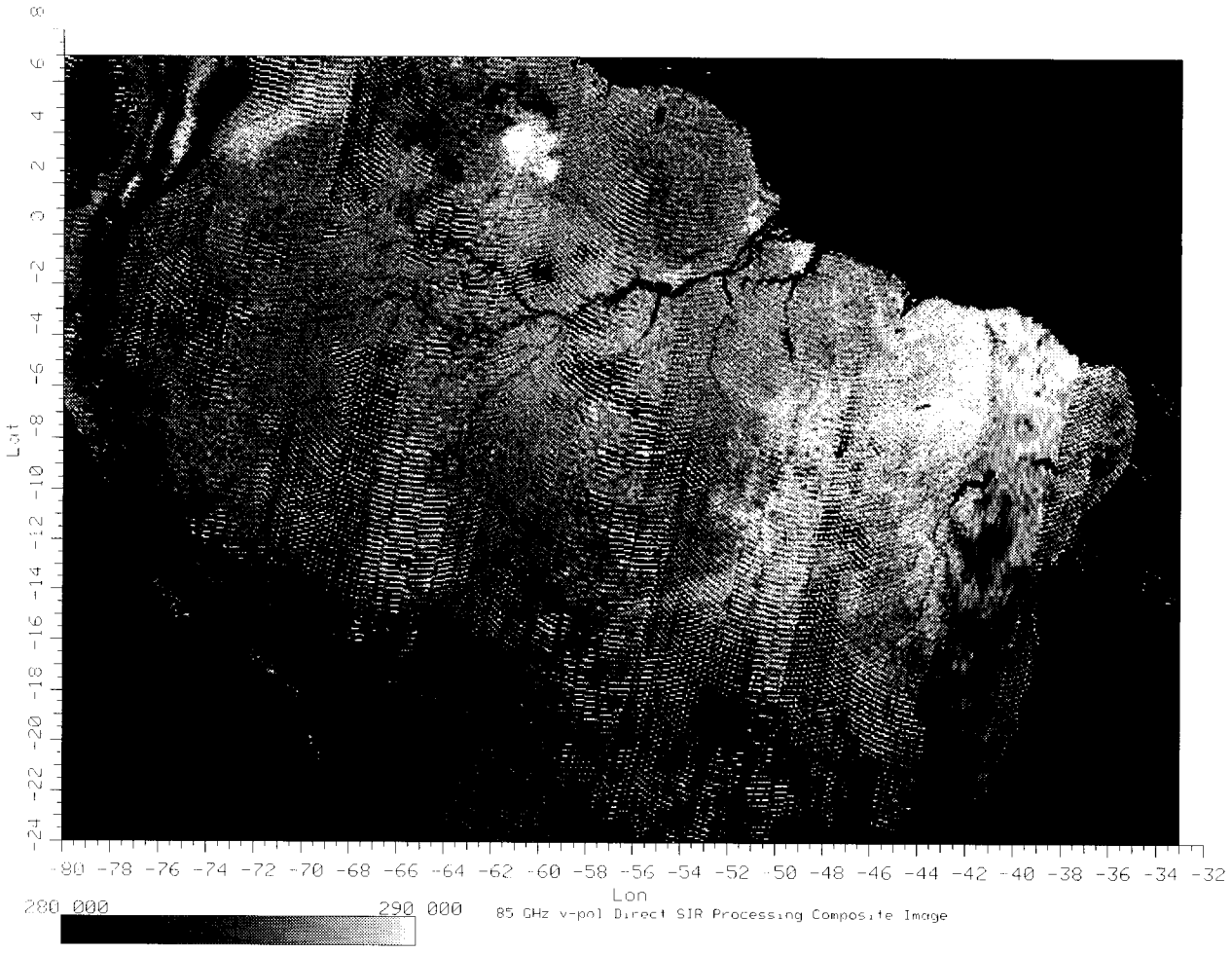

Figure 4.4: Direct SIR Processing Image: 85 GHz v-pol.

of the algorithm is that it does not objectively remove atmospheric distortion.

When both cloud-covered and cloud-free measurements are taken over exactly the same geographical location, SIR averages the measurements together. If these measurements are just slightly offset, however, SIR will weight each more heavily in its center. The result of this causes the undesirable arc-like appearance in the image. Since this technique generates unacceptable composite images, the other techniques do not attempt to combine data from different satellite passes into the same SIR image. Instead, they first generate a set of images from individual satellite passes and then combine these images to to remove atmospheric effects.

4.3.2 Mean

This technique is the simplest form of combining single pass images. The algorithm input is a set of single pass SIR images. These images are averaged on a pixel basis to produce the composite image. Cross image registration is not a problem since the image reconstruction plots the images to the raw measurement's pre-registered geolocation. Pixel values less than 50 K or greater than 325 K are ignored in this average since it is assumed that they are erroneous data (320 K corresponds to 115 degrees Fahrenheit). The results are found in Figure 4.5. Theoretically, this technique reduces atmospheric distortions by ensemble averaging. Unfortunately, the very cold atmospheric distortion lowers the averages to an unacceptable level, as seen in the image's black spots. As in the previous technique, this method's main weakness is that it does not remove the distorted measurements.

4.3.3 Windowed-Average

The windowed-average technique is similar to the mean calculation but it first attempts to remove atmospheric distortions by creating a range of non-distorted brightness values. This is a three step process. First, each pixel's average brightness temperature is found by using the mean calculation method described above. Second, the ensemble standard deviation is computed for each each pixel. Third, each composite pixel value is calculated by averaging only the ensemble values within a user defined range or window based on the pixel's standard deviation from its mean. In effect, this algorithm treats two types of distortion: Gaussian

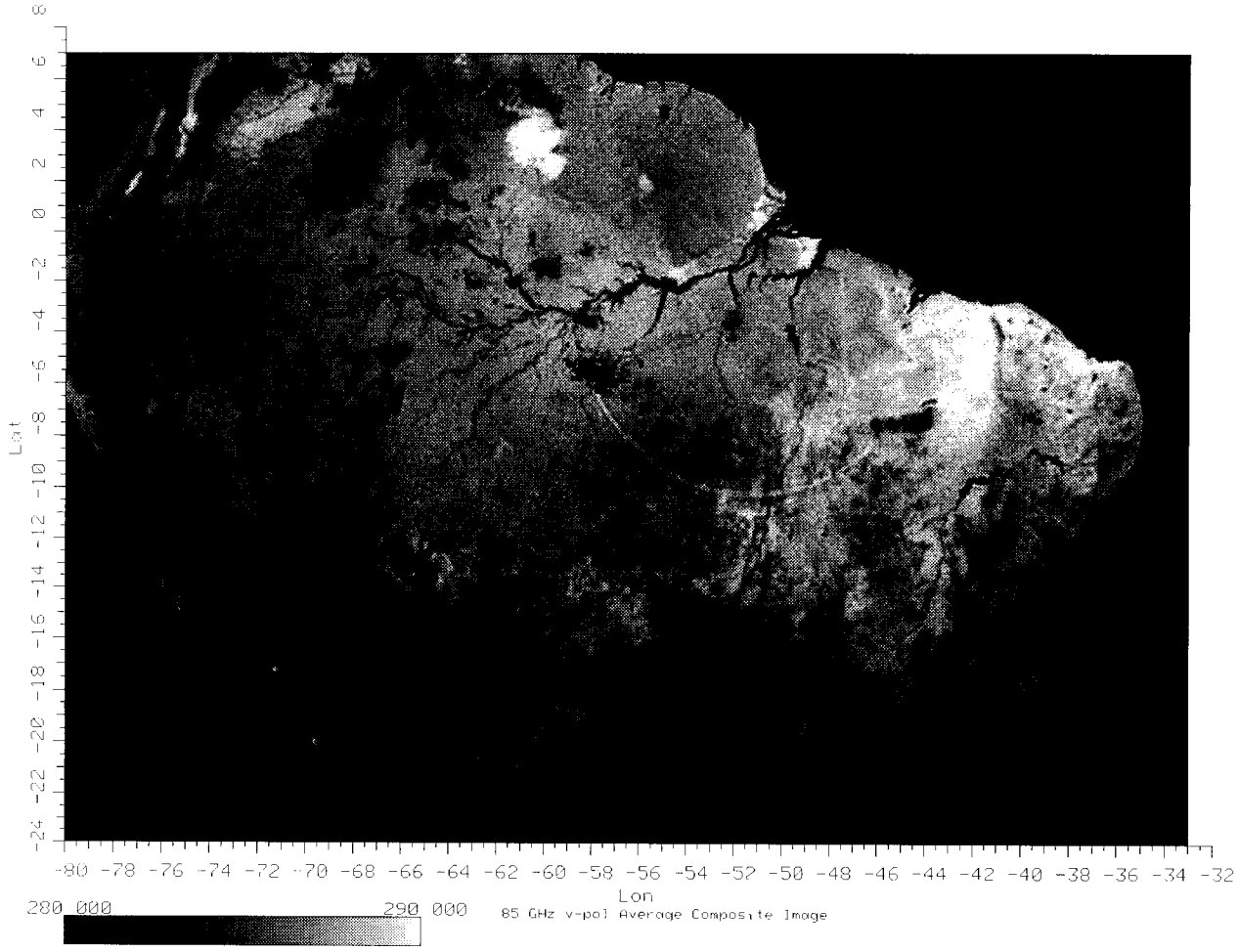

Figure 4.5: Single Pass Averaging: 85 GHz v-pol.

noise and atmospheric cold spots. By removing the "tails" of the pixel value distribution, the cloud cold spots that lie outside range of Gaussian noise are eliminated. Methods to pick the window size are found in [20]. As with the other algorithms, this technique assumes that the distorting atmospheric conditions are temporally random such that no geographical area attracts semi-permanent clouds, rain, etc. Such conditions cause multi-population distributions of cloudy and cloud-free pixel values. These conditions may occur in mountain-locked areas such as the Andes but appear not to exist in the flatter Amazon. Figure 4.6 illustrates the results of this technique using pixel values within one standard deviation of their ensemble mean.

The windowed-average technique gives results similar to the mean. Again, the method fails to detect and remove the cold atmospheric measurements. Since the 85 GHz channel is highly effected by clouds and rain, a single cold measurement increases the standard deviation as well as lower the mean. Thus, the large standard deviation makes the window of cloud-contaminated ensembles so large that the cloud-covered values are not removed. If the window range is reduced by a percentage of the standard deviation, then ensembles without cloud contamination (low std. dev.) are not averaged because almost all pixel values are outside the window. If no measurement values are found in the window, then the average value is used. In short, the algorithm fails because the range of standard deviations differs too greatly between cloud-free and cloud-covered ensembles.

4.3.4 Second Highest Value

This method is used by Choudhury, *et al.* [21]. In this approach atmospheric distortion is removed by only using the second highest pixel value from the ensemble. Since the atmospheric distortion generally lowers the brightness temperature measurements, high pixel values should offer images with the least atmospheric influence. However, the highest value is often strongly influenced by noise or can come from processing artifacts. For that reason, the technique uses the second highest pixel value. The results of this method are found in Figure 4.7. The image produced by this technique appears to be free from the cold atmospheric distortion seen in the other techniques. In that aspect the technique is

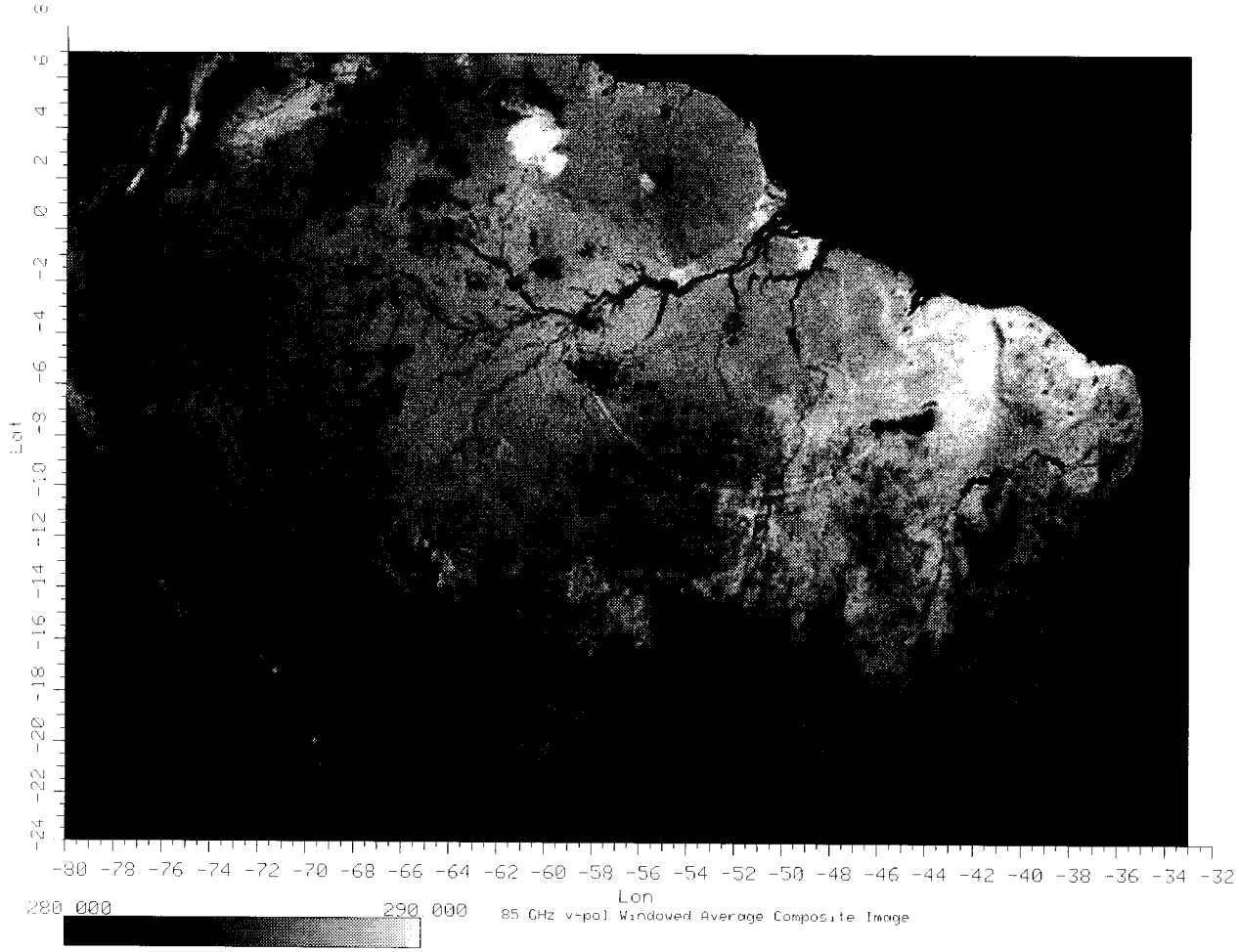

Figure 4.6: Windowed Average (-1 St.Dev to +1 St. Dev): 85 GHz v-pol.

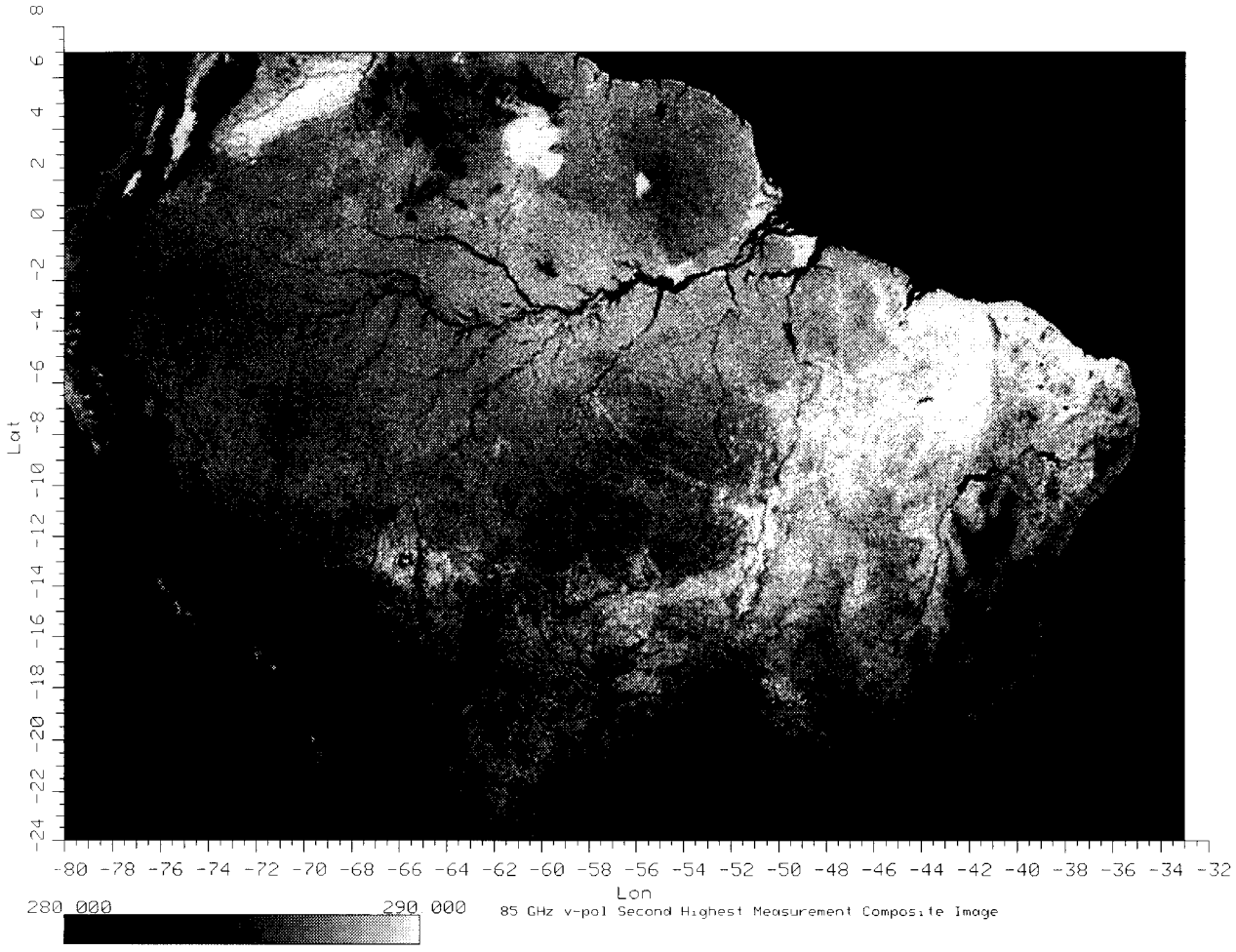

Figure 4.7: Second Highest Value Estimation: 85 GHz v-pol.

successful.

Although the second highest value algorithm does not "average" pixel values to reduce noise, it does produce a noise variance lower than the complete ensemble noise. Choosing the second highest value is an example of rank order statistics. The best known type of rank order technique is the median filter of which there is a large body of literature [14]. Some aspects of the median filter will be presented here to give some insight into performance of the related "second highest value" method.

Narenda [22] has compared the noise reduction of the median filter and the average filter as they are applied to normal and uniform distributions. Adapting his results to a one dimensional study, the estimate variances of the mean and median values from a set of n measurements are listed in Table 4.1. For these sim-

Comparsion of Mean and Median Techniques with Noise Variance σ^2		
	Gaussian Noise	Uniform Noise
Median	$\frac{\pi\sigma^2}{2(2+n)}$	$\frac{3\sigma^2}{n+2}$
Mean	$\frac{\sigma^2}{n}$	$\frac{\sigma^2}{n}$

Table 4.1: Variance of the Mean and Median Estimate Noise using "n" Samples.

ple distributions, the mean filter is more effective at noise reduction. Tail heavy distributions, however, offer opposite results. Narenda illustrates this by analyzing the log-normal distribution. For this case he finds that the median filter is approximately 50% better than the mean for a sample size of $n = 9$. Thus, the second highest technique's ability to reduce noise is strongly influenced by the measurement distribution.

According to order statistics, from an ensemble of n independent, identically distributed measurements, $X_1, X_2, ..., X_n$, the probability density function $f_{X_{(r)}}(y)$ of the rth largest measurement $X_{(r)}$ is a function of its position in the

ordered ensemble and the distribution of each independent measurement, i.e.,

$$f_{X_{(r)}}(y) = \frac{n!}{(r-1)!(n-r)!}[F_X(y)]^{r-1}[1-F_X(y)]^{n-r}f_X(y) \qquad (4.1)$$

where $F_X(y)$ and $f_X(y)$ are the cumulative distribution function and probability density function of the independent measurements, respectively. Such rank order statistics may be helpful in estimating the reduction in noise variance when the amount of distortion and its distribution is unknown [23].

Since the distribution function for the SSM/I data is not known precisely, it is not possible to analytically compare estimator variance reduction for the "second highest value" and mean value methods. However, it is known that in the presence of atmospheric distortion, the distribution is skewed low, while the desired estimation parameter is the mode on the high end of the distribution (See Section 1.3.5). This strongly suggests that the rank order statistic needed, r, is closer to n than the median, $n/2$. Given this insight, the "second highest value" method is a reasonable approach.

4.3.5 Modified Maximum Average

The modified maximum average technique was created *ad hoc* during this research by combining attributes of the previous three techniques. The algorithm attempts to estimate the brightness of a pixel by first selectively choosing a set of pixel values from the ensemble and then by averaging those selected values together. This is done in the hope that the selection of values from the ensemble will remove the cloud distorted pixel values and that the averaging of the selected pixels will help to reduce noise and attenuate bias.

To select pixel values from the ensemble, one first calculates the sample mean value, μ_o, of the entire pixel ensemble. Values which are greater than μ_o yield a subset of the complete ensemble corresponding to its highest values. To complete the selection process, the highest value of this subset is eliminated. Thus, the selected values consist of all those values which are above the ensemble mean but less than the highest value of the ensemble.

Analyzing this technique statistically is challenging for two reasons: 1) the distribution of pixel values when clouds are included is not clearly known and

2) the algorithm combines both box averaging statistics and order statistics. To justify this approach, consider the simple model where a pixel measurement is a Gaussian distribution with a weighted binary random variable:

$$T_{b,m} = \eta(\mu, \sigma_o) - p_d K \tag{4.2}$$

where $T_{b,m}$ is the measured brightness temperature, η is the Gaussian distribution with mean μ and standard deviation σ_o, p_d is either one or zero based on the probability that a measurement contains cloud distortion (about 30%), and K is a large positive RV representing the drop in brightness temperature due to a cloud (thus K will depend on the cloud thickness, water content, etc., the statistics of which are unknown). An example of such a continuous distribution of measurements is found in Figure 4.8. The marks below the temperature axis illustrate samples of an ensemble of seven pixel values with $K = 10$ and $p_d = 30\%$ cloud distortion. The algorithm also illustrates the bias from the different techniques.

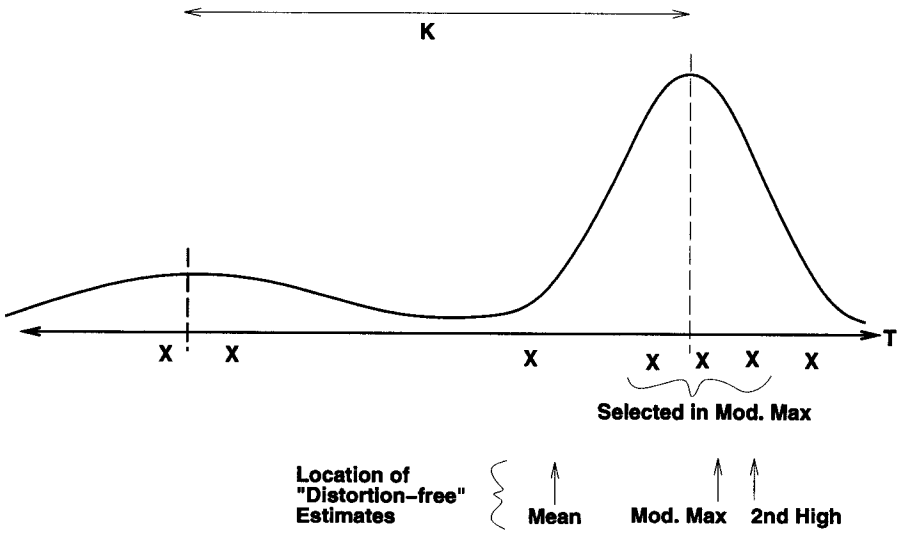

Figure 4.8: Example of Radiometric Measurement Distribution with Sample Discrete Ensemble.

To compare the variances of the modified maximum mean algorithm and the second highest technique consider Figure 4.9. The "X"'s represent an example ensemble of seven samples taken from the distribution. The variance of the second highest technique is governed by the average temperature difference

between the highest and third highest value of the ensemble. The variance of the modified mean algorithm will depend on the variances of the second, third, and usually fourth measurement. Graphically, one may see that the averaging of these values will lower the estimate variance more than just using the second highest value.

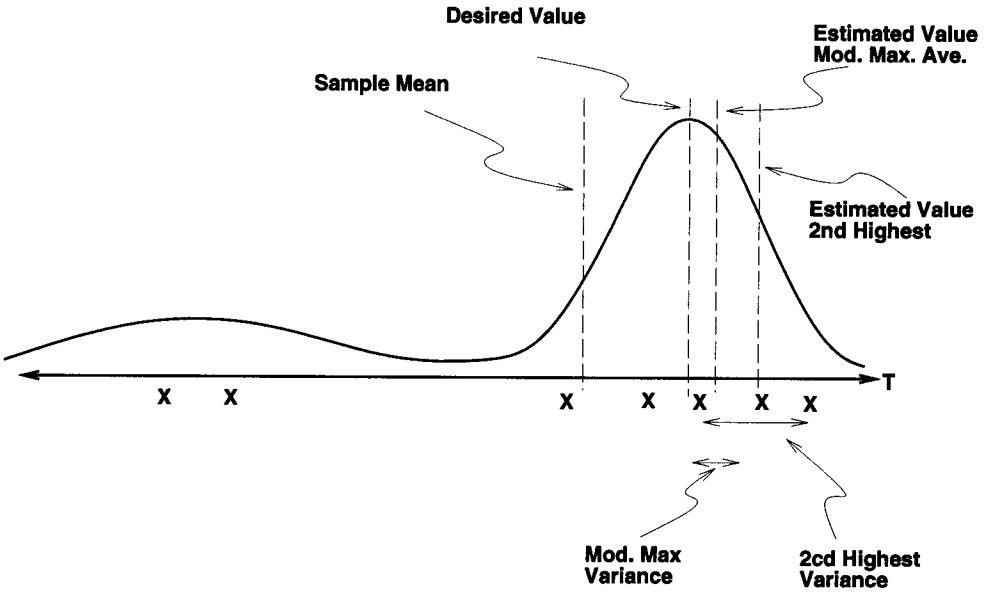

Figure 4.9: Example of Variance for Modified Maximum and Second Highest Techniques.

The modified maximum average estimate in this example is biased high, and will be whenever the ensemble includes more than one sample form the lower mode of the mixture distribution. However, it is clear that this bias is less than that from the second highest approach, and the estimation variance will be less if the main mode is from a Gaussian distribution.

The results of the modified maximum algorithm (see Figure 4.10) are very promising. The image does not contain cold atmospheric distortions nor swath edge artifacts. A simulation further compares and demonstrates the algorithms.

4.3.6 Atmospheric Distortion Removal Simulation

This section shows the results of the techniques in an atmospheric removal simulation. The simulation tests the four algorithms that remove or attenuate distortion by combining images on a pixel basis. The SIR processing algorithm

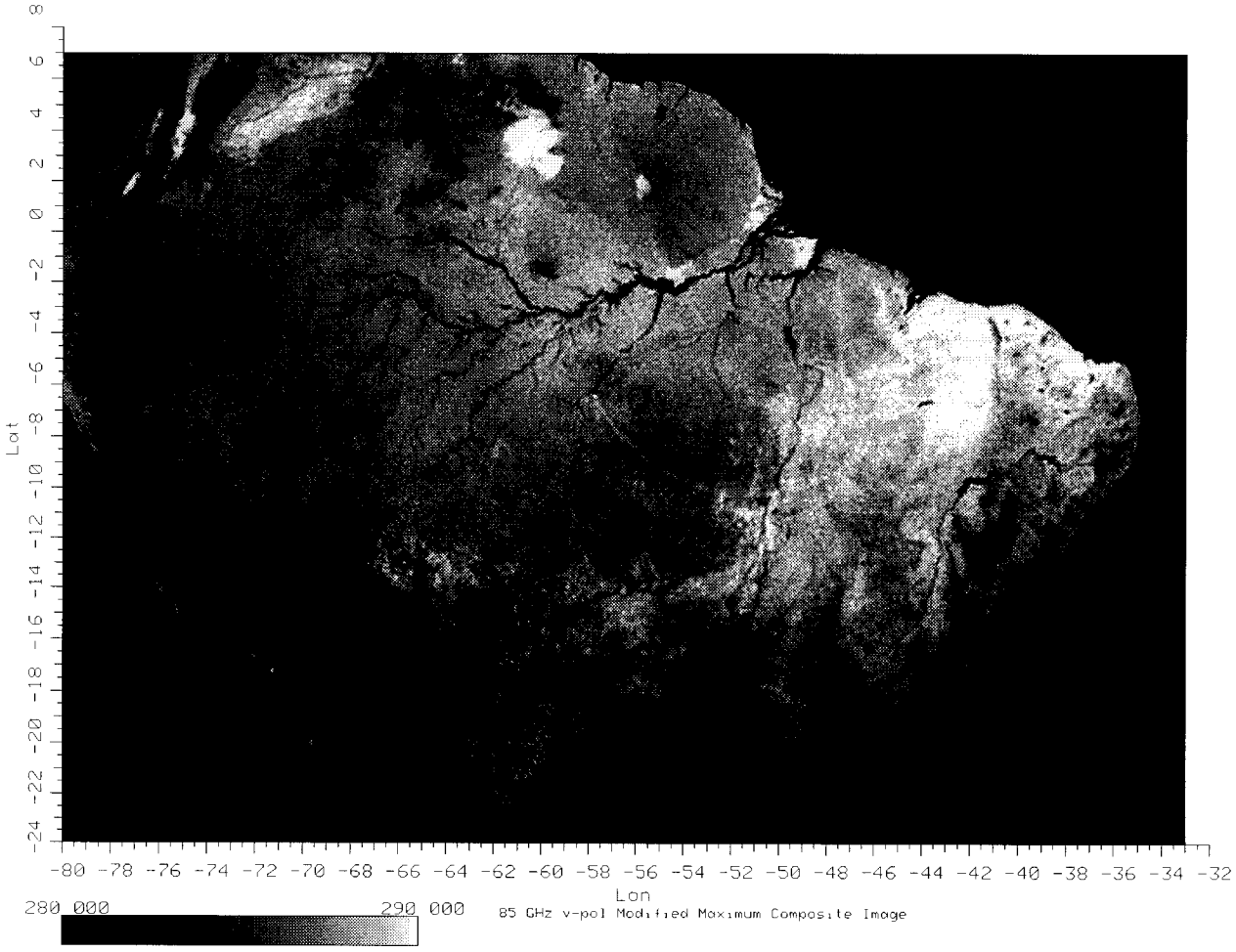

Figure 4.10: Modified High Measurement Calculation: 85 GHz v-pol.

is not simulated because it performed so poorly with true SSM/I data. The simulation is now described.

The simulation assumes that the true pixel brightness for a certain geographical area is 280 K. An ensemble of seven pixel values is then created by adding a Gaussian random variable of standard deviation 1 K to the "true" value. Seven pixels simulate an average number of radiometric measurements in a fifteen day period while the Gaussian random variable represents the sensor noise in those measurements. Two of the ensemble measurements are then assumed to be atmospherically distorted by an amount T_{dis}. This is referred to as the atmospheric dip. The first measurement is reduced by T_{dis} and the second measurement by one half that amount. This models a pixel which is contaminated by two clouds, one twice as distorting as the other. The seven member ensemble is then processed by each algorithm and the results are saved. The results of 1000 simulations are then averaged to give the results in Figure 1.11.

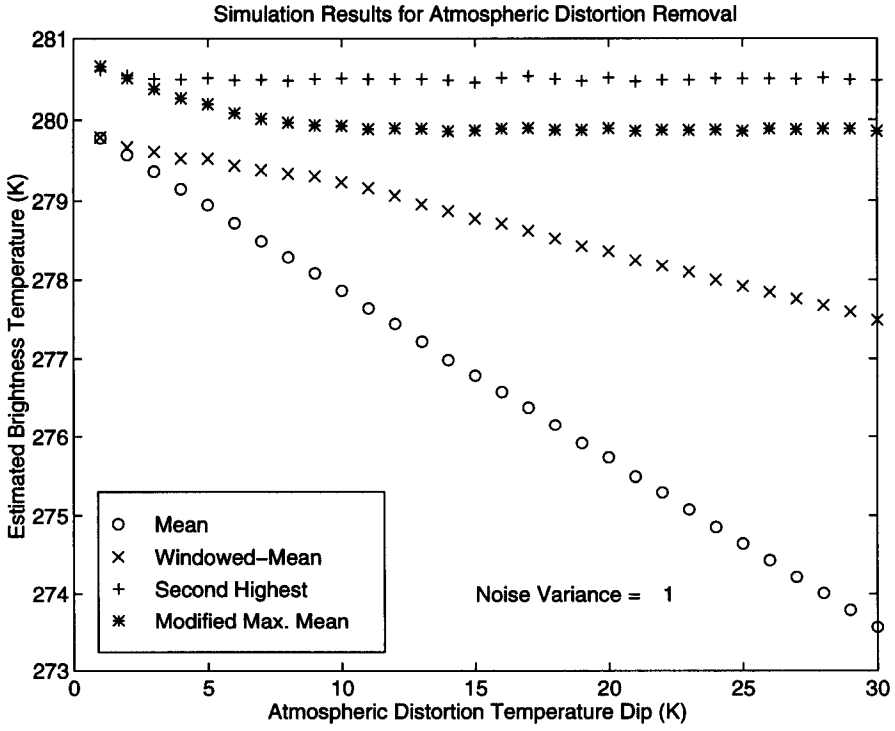

Figure 4.11: Simulation Results of Atmospheric Distortion Removal (True value is 280 K).

For pixels with little to no atmospheric distortion, the mean and windowed-average algorithms generate values closest to the 280 "true" value. For ensembles which are more corrupted by atmosphere (greater than 5 K), the second highest and modified maximum techniques are superior. Finally, the modified maximum mean technique is chosen as the best algorithm due to its averaging effect. Thus, the simulation confirms the results found with real SSM/I data.

4.4 Summary

This chapter discussed ways to generate surface brightness mappings for the SSM/I channels. These surface mappings represent the surface brightness temperature without temporal scattering from clouds or precipitation. These mappings are generated with single pass SIR images and a modified averaging algorithm. Since the composite "base" images are used in the next chapter, they are presented now (See Figs. 4.12 to 4.18).

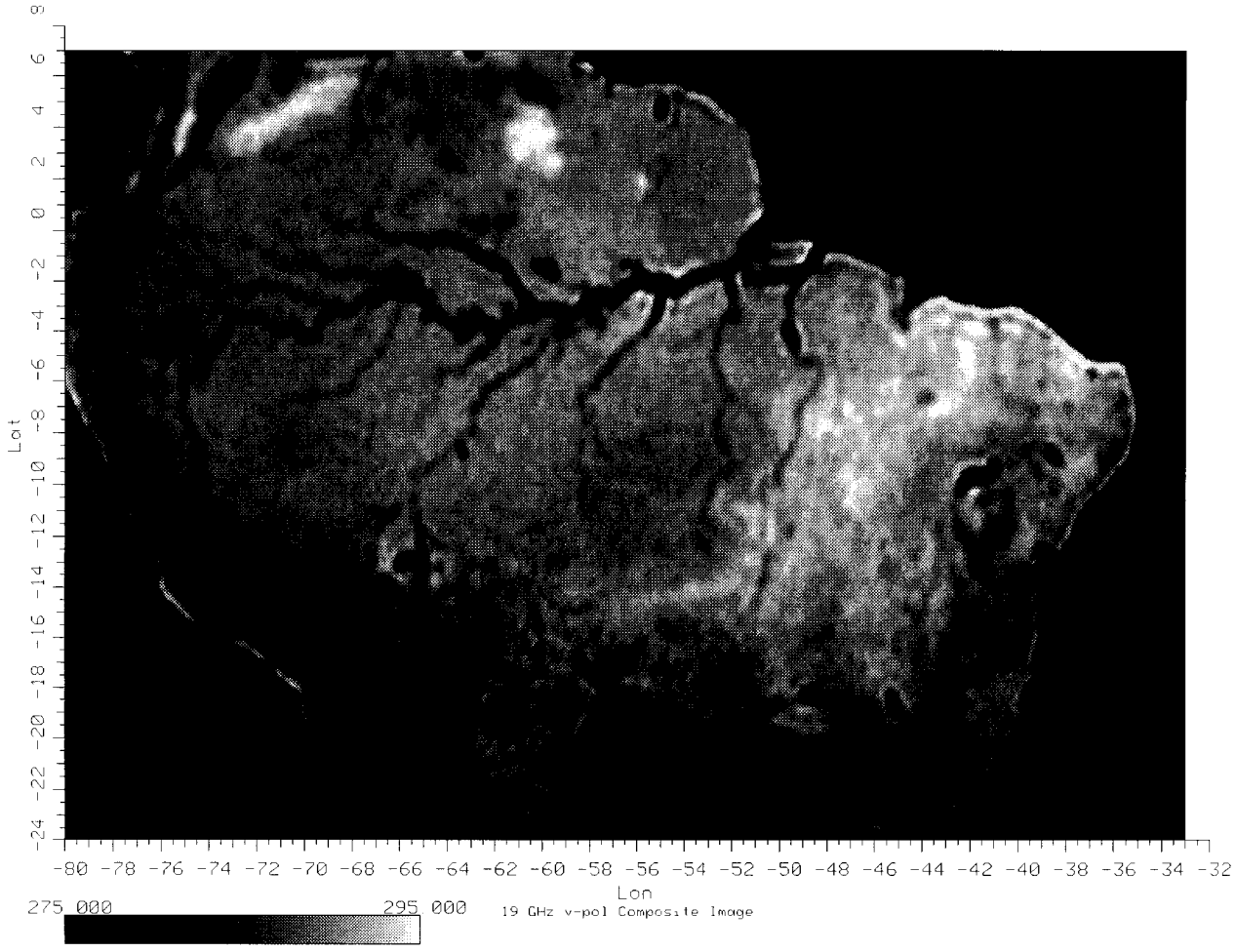

Figure 4.12: Background Mapping of Amazon Basin for 1-15 September, 1992: 19.35 GHz v-pol.

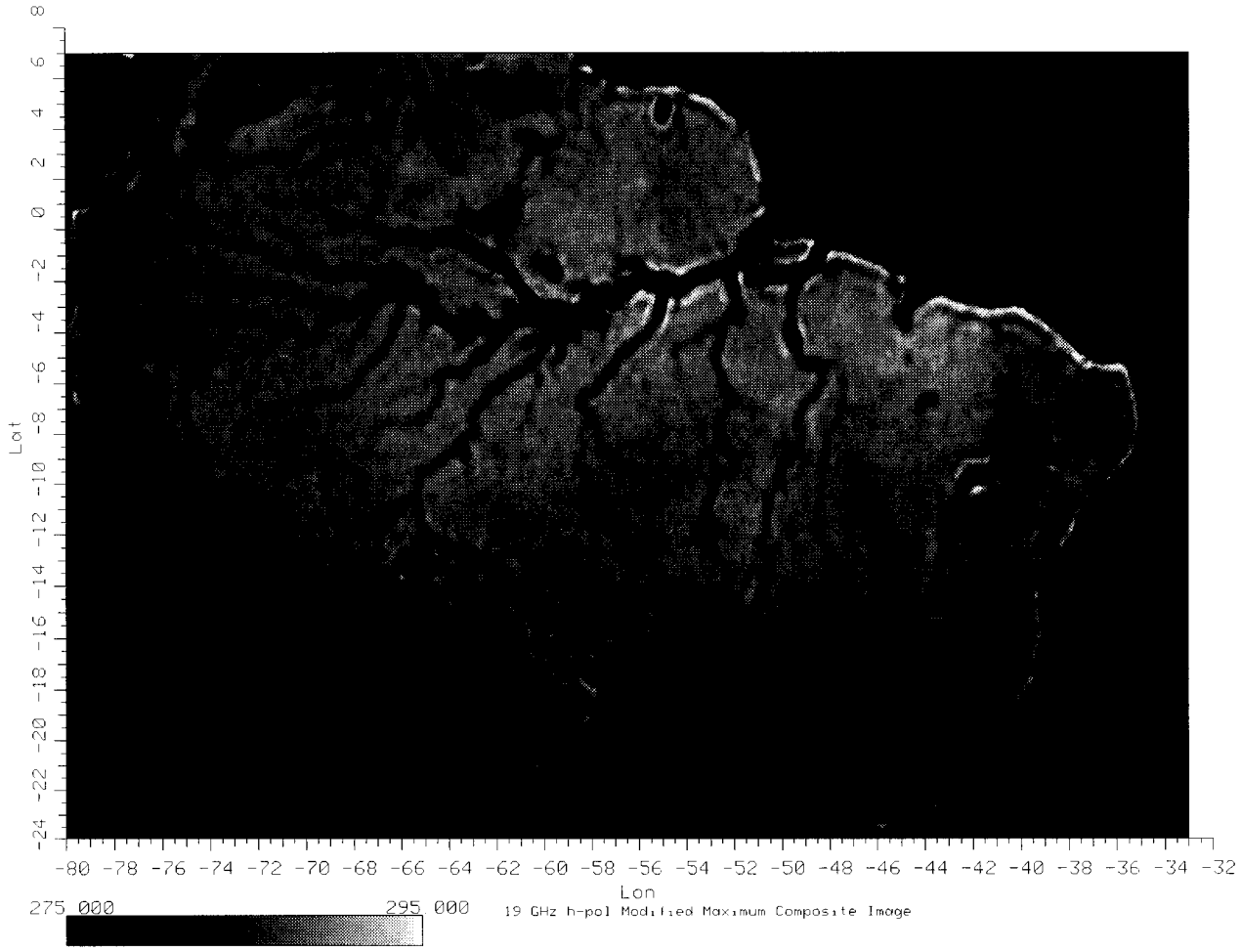

Figure 4.13: Background Mapping of Amazon Basin for 1-15 September, 1992: 19.35 GHz h-pol.

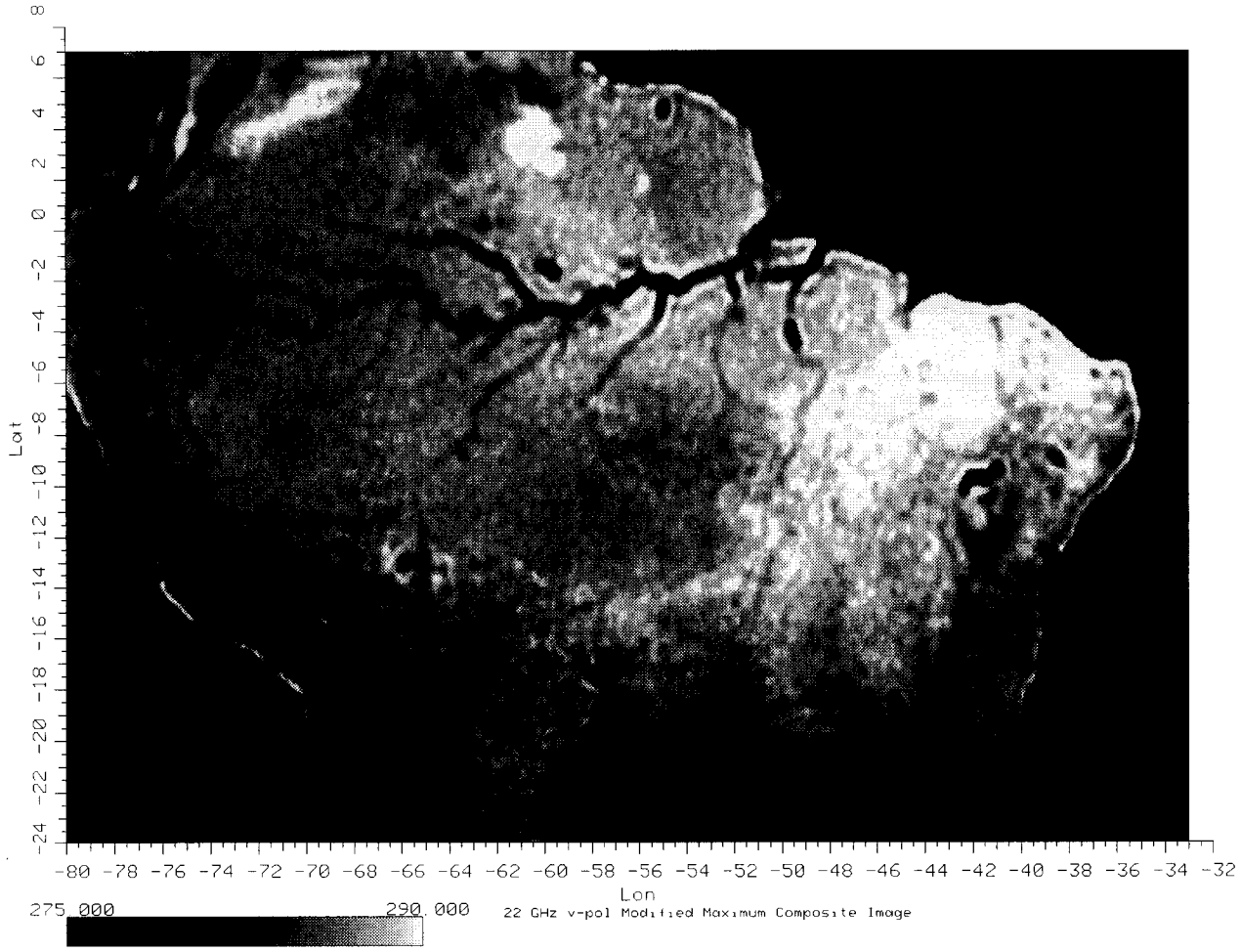

Figure 4.14: Background Mapping of Amazon Basin for 1-15 September, 1992: 22.235 GHz v-pol.

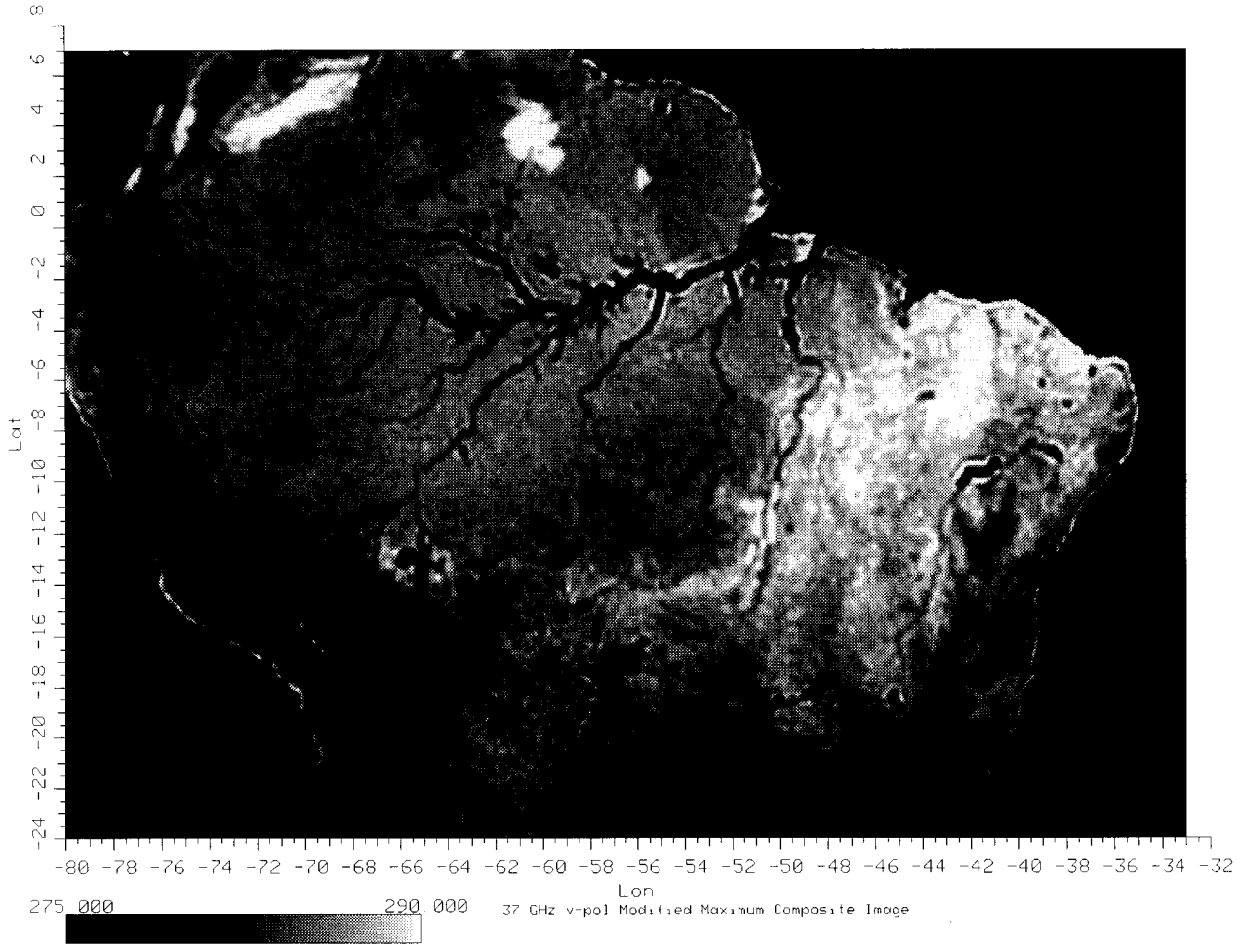

Figure 4.15: Background Mapping of Amazon Basin for 1-15 September, 1992: 37.0 GHz v-pol.

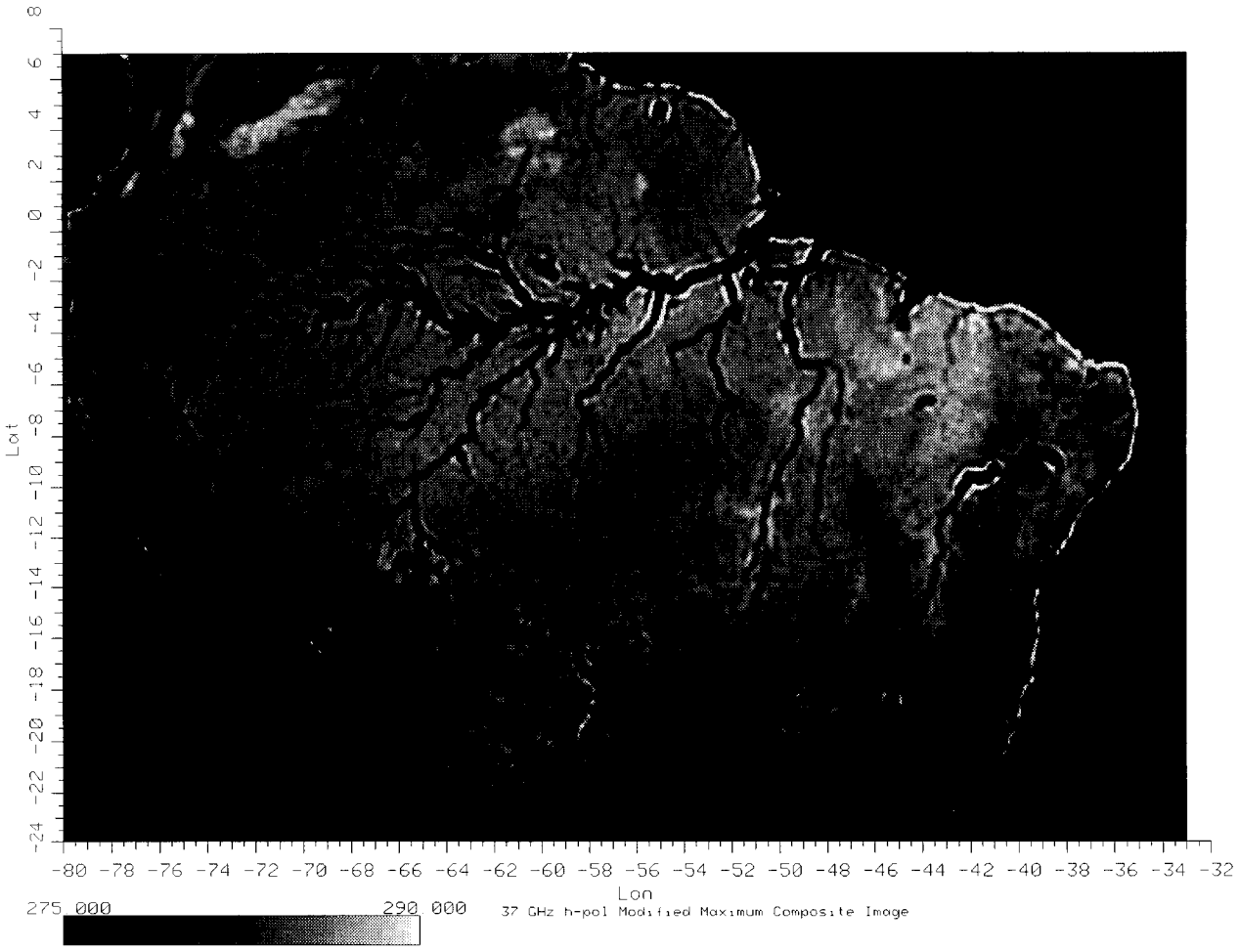

Figure 4.16: Background Mapping of Amazon Basin for 1-15 September, 1992: 37.0 GHz h-pol.

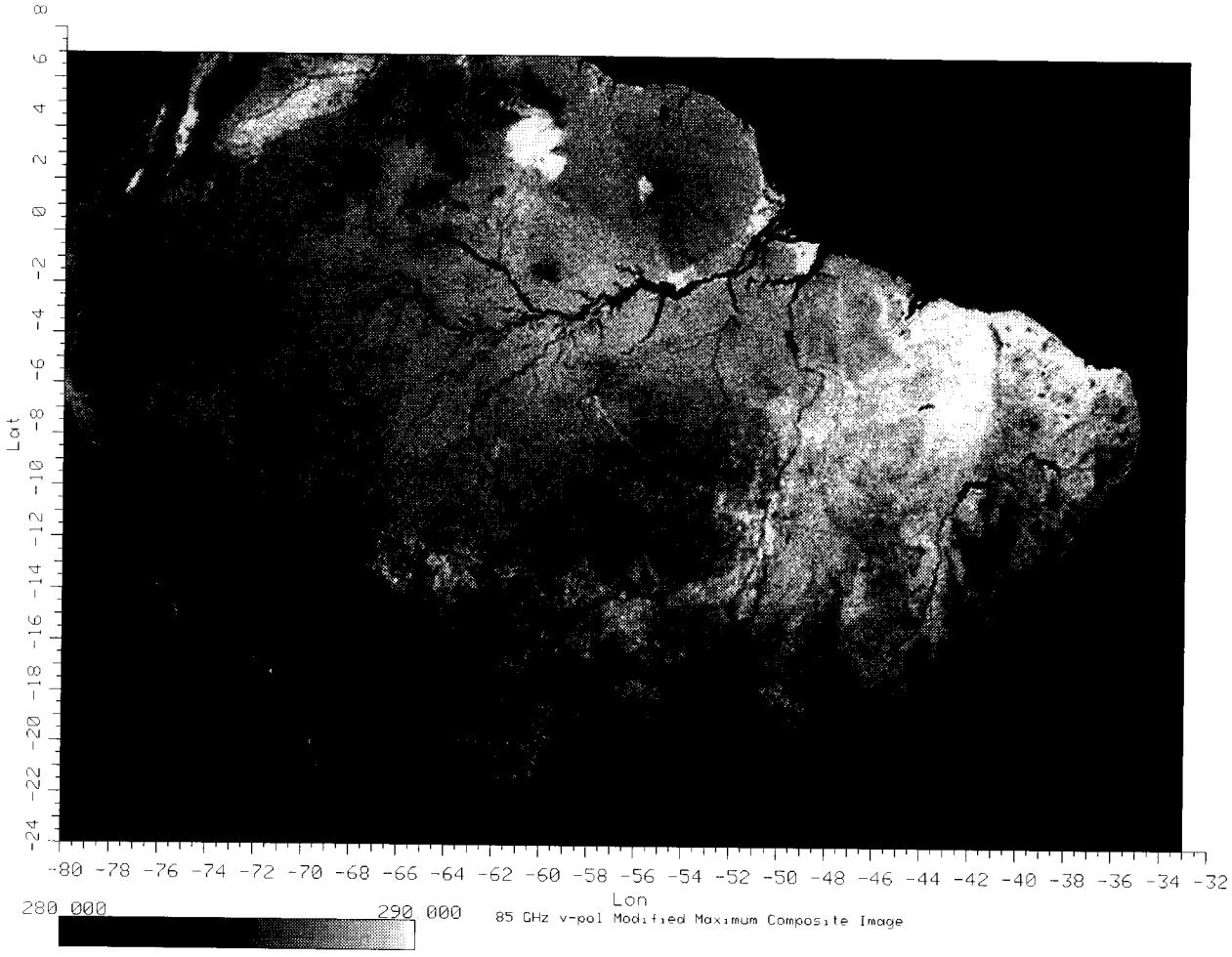

Figure 4.17: Background Mapping of Amazon Basin for 1-15 September, 1992: 85.5 GHz v-pol.

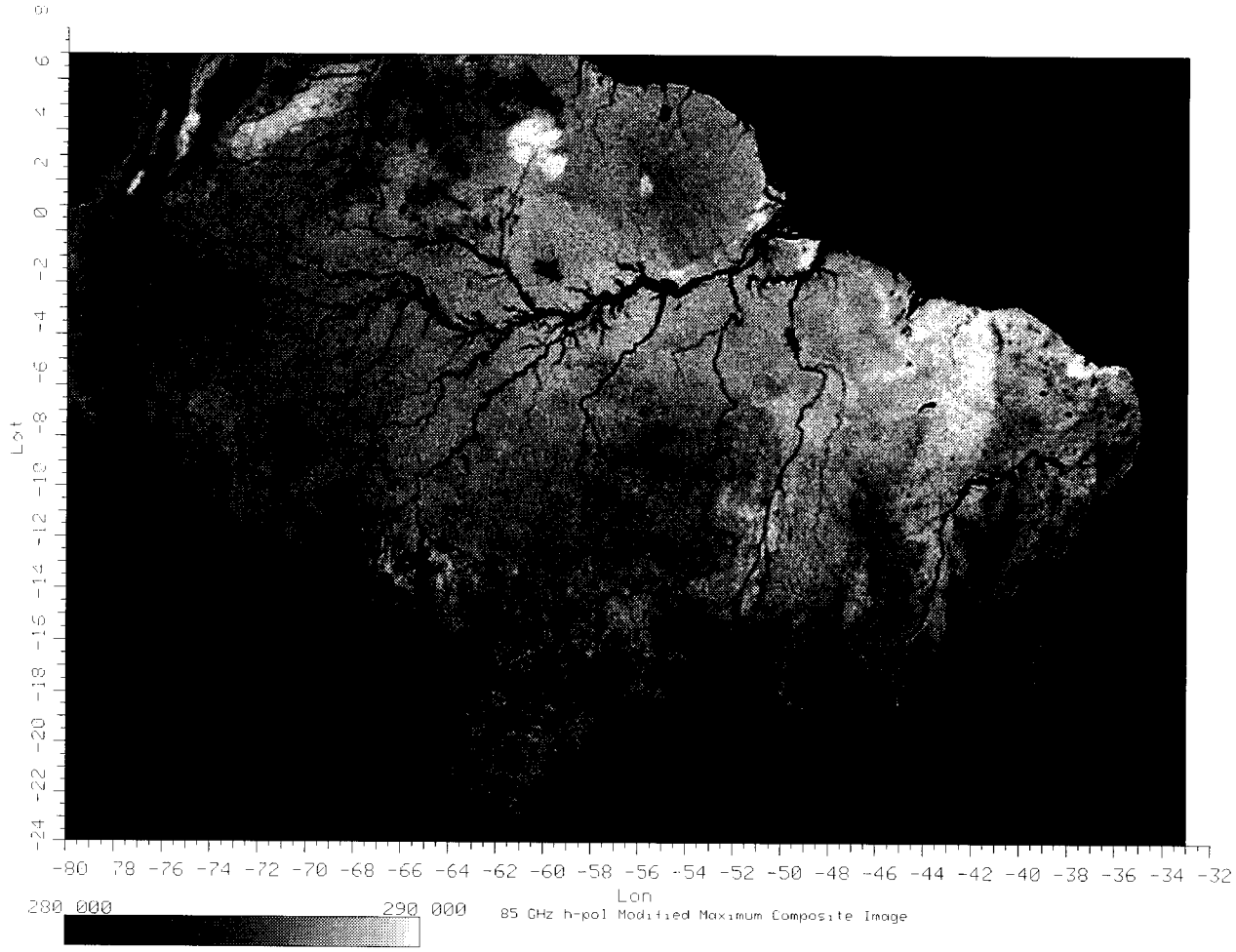

Figure 4.18: Background Mapping of Amazon Basin for 1-15 September, 1992: 85.5 GHz h-pol.

CHAPTER 5

IMAGE ANALYSIS

5.1 Introduction

The threat of global warming has motivated many studies about the role the Amazon rainforest and surrounding regions play in global climate. To understand the area's impact, scientists need accurate geophysical information from the region. A key source for this information comes from remote sensing instruments such as the SSM/I. This thesis explores the utility of enhanced resolution imaging of SSM/I data as applied to vegetation studies of the Amazon. While previous chapters have focused on the enhanced resolution imaging techniques of reconstruction and atmospheric distortion removal, this chapter illustrates how the enhanced resolution images may be applied to surface studies. In particular, this chapter focuses on using the "base" composite images developed in the previous chapters to discriminate between Amazonian vegetation classes. It is found that the SSM/I correctly discriminates between the five major vegetation types of the Amazon Basin 60% of the time. This is comparable to, but less than, the discriminatory capability of scatterometer images.

This chapter presents the following topics: 1) the motivation to use radiometry for vegetation discrimination, 2) a discussion about vegetation discrimination vs. vegetation classification, 3) a description of "truth" data used in discrimination learning algorithms, 4) a presentation of several discrimination algorithms, 5) a comparison of SSM/I discrimination results including a comparison with SASS results, and 6) conclusions of the vegetation discrimination experiment.

5.2 Using Radiometry in Vegetation Discrimination

Earth-looking spaceborne instruments are valuable in detecting multi-decadal and seasonal vegetation changes. Such vegetation changes help researchers understand regional/global climate trends and evaluate the effect of man-made influences. In order for researchers to perform these studies, however, multiannual

spaceborne sensor data must be available and that data must show discriminatory potential. To a degree microwave radiometers fulfill each of these requirements.

Microwave radiometers have been flying in space continuously since the 1970's. Thus, they can provide data to support multiannual studies about the last two decades. In addition, land-based radiometers have demonstrated that the radiometer has the ability to discriminate between vegetation classes through scattering differences from plant structure and leaf shape.

In the past, however, atmospheric distortion and the spaceborne radiometer's low resolution have impeded the radiometer's ability to perform vegetation discrimination. For this reason, most vegetation studies have used other sensors, such as high resolution, limited-coverage IR instruments or atmospheric penetrating microwave scatterometers. The techniques described previously in this thesis help overcome the limitations of the spaceborne microwave radiometer so that the multidecadal data may be more useful. Specifically, this chapter shows that the SSM/I's enhanced resolution, atmospheric-free base images are useful in discriminatory studies.

5.3 Vegetation Discrimination vs. Vegetation Classification

This thesis defines vegetation discrimination as the attempt to differentiate between classes of vegetation on the Earth's surface by using spaceborne sensor data. This is accomplished by characterizing vegetation types according to their sensor response. Defined this way, vegetation discrimination is a tool to increase the ability to correctly estimate broad classes of vegetation types. Vegetation classification algorithms, on the other hand, attempt to uniquely identify vegetation type for an entire region including troublesome spots at boundaries where the vegetation types may be mixed. This thesis does not attempt such a classification. The goal of this research is to demonstrate that radiometric data has a discriminatory correlation with Amazonian vegetation classes. This will be demonstrated through confusion tables instead of a classification pseudocolor map.

5.4 Ground Truth Data

To use the SSM/I base images, a vegetation discrimination algorithm needs "ground-truth" data. This data consists of the vegetation types known from *in situ* measurements for a given set of geographical locations. This ground data is then used in conjunction with the SSM/I base images to train the discriminatory algorithm.

The "truth" data points used in this research are obtained from the United States Environmental Protection Agency Climate Research Program's Global Ecosystems Database [24]. This database is a joint project of the EPA's National Geophysical Data Center, U.S. National Oceanic and Atmospheric Administration, and the Environmental Research Laboratory-Corvallis. It's primary goal is to provide global information on a variety of geophysical parameters which contribute to the world environment. Included in this data set are geographical and time sequential information about temperature, cloud cover, soil moisture, soil types, animal density, etc. The data used in this thesis comes from a subset database entitled *World Ecosystems* by Jerry S. Olson from the Global Patterns Company.

The *World Ecosystems* digital vegetation map classifies all Earth land regions into 73 categories. The map resolution is between 10 and 30 geographical minutes (20-55 km near the equator). Using the EPA provided software, IDRIX, vegetation parameters for the Amazon Basin are extracted. According to *World Ecosystems* the Amazonian region contains 19 different surface classifications. Table 5.1 lists these vegetation types according to vegetation identification number, vegetation description, and surface percentage.

As seen in the table, approximately 85% of the mapped surface is classified in one of six surface classes: 0, 29, 33, 41, 43, or 59. Each of these classes covers a minimum of 5% of the mapped area, thus offering a suitable number of "truth" points to be used in the supervised discrimination. A vegetation pseudocolor mapping of the Amazonian basin is found in Figure 5.1.

The *World Ecosystems* data, however, has two major limitations. First, the database resolution is lower than the resolution of the SSM/I images. This prevents detailed discrimination tests. Second, the vegetation classes are more

Amazon Vegetation Map

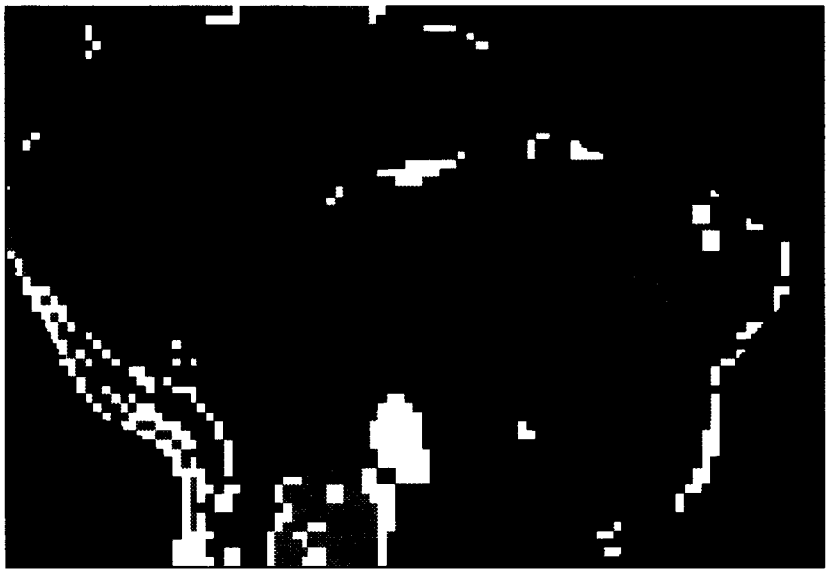

Legend

- Tropical Rainforest (33)
- Tropical Broadleaf Seasonal (29)
- Mild/Warm/Hot Grass (41)
- Savanna/Grass, Seasonal Woods (43)
- Succulent and Thorn Woods (59)
- Tropical Montane Complexes (28)
- Mild/Hot Farmland (31)
- Rain-Green, Seasonal Evergreen (32)
- Fields/Woods with Grass/Cropland (58)
- Marsh or Swampy Wetlands (45)

Amazon Vegetation/Surface Classifications		
ID	Description of Surface Type	Pct.
0	Ocean and sea	27.4
8	Desert, mostly bare stone, clay or sand	0.4
28	Tropical montane complexes, typically evergreen	2.3
29	Tropical broadleaf seasonal, with dry or cool season	14.0
31	Mild/hot farmland and settlements	3.0
32	Rain green (drought deciduous) or seasonal dry evergreen	2.2
33	Tropical rainforest	14.7
36	Paddy rice and associated land mosaics	0.5
37	Warm/hot cropland, irrigated extensively	0.5
41	Mild/warm/hot grass/shrub	14.8
43	Savanna/grass, seasonal woods interspersed	9.1
45	Marsh or other swampy wetlands	1.7
48	Dry evergreen woodland or low forest	0.2
51	Semidesert/desert scrub/succulent/sparse grass	0.3
53	Tundra	1.0
56	Forest/field complex with regrowth after disturbance	1.0
58	Field/woods with grass and/or cropland	1.7
59	Succulent thorn woods or scrub is widespread	5.1
71	Salt/soda flats desert playas	0.1

Table 5.1: Vegetation/Surface Classification Groups for Amazonian Region (80 W - 33 W, 24 S - 7 N) from *World Ecosystems* [24].

broad than those used in other experiments [25]. Unfortunately, a ground truth database with more detail is currently unavailable.

Given the "truth" data set, a group of prototype feature vectors is produced to train the discrimination algorithms. A prototype vector is formed by choosing a large number of geographical points on the EPA vegetation map where the vegetation type is known. These geographical coordinates are then located on each of the seven SSM/I base images. The array of seven brightness temperatures for each geographically located point serves to characterize the known vegetation type and is known as prototype feature vector. I used a prototype data set of 5000 "truth" points extracted manually from the EPA map. These points were extracted from the middle of the specified vegetation regions to avoid areas of mixed vegetation types. After extracting the prototype feature vectors, I was able to characterize each vegetation class by finding the mean and standard deviation

of the prototype points corresponding to its particular vegetation class. A statistical breakdown of the brightness values according to vegetation type follows (See Tables 5.2 and 5.3). Given the colocated ground truth and brightness values just tabulated, I am prepared to implement vegetation discrimination algorithms.

Mean T_B (K) by SSM/I Channel and Surface Type								
Veg. ID	Pts.	19-V	19-H	22-V	37-V	37-H	85-V	85-H
29	938	288.42	286.38	286.81	284.58	282.97	286.50	285.88
33	1107	286.83	285.06	285.27	282.93	281.47	285.49	284.92
41	1106	286.90	281.23	285.15	283.84	279.89	284.19	282.59
43	877	288.29	284.97	286.46	284.60	282.33	285.74	284.97
59	570	288.43	283.94	287.04	285.96	282.59	286.87	285.40
0	402	198.40	135.09	222.75	216.37	159.50	260.03	231.53

Table 5.2: Average T_B in K for Amazonian Vegetation and SSM/I Channels.

Std. Dev. of T_B (K) by SSM/I Channel and Surface Type								
Veg. ID	Pts.	19-V	19-H	22-V	37-V	37-H	85-V	85-H
29	938	2.602	3.938	1.872	2.581	4.259	1.819	2.197
33	1107	2.238	3.975	1.494	2.106	3.998	1.417	1.737
41	1106	4.474	5.759	3.725	4.250	5.334	3.538	3.850
43	877	2.678	3.757	1.956	2.864	3.216	2.229	2.155
59	570	3.658	5.087	2.856	3.734	5.517	2.452	2.879
0	402	13.29	21.29	19.75	9.67	17.27	7.70	15.58

Table 5.3: T_B Standard Deviation (K) for Amazonian Vegetation and SSM/I Channels.

5.5 Vegetation Discrimination Algorithms

Many algorithms have been developed to perform multivariate discrimination [14, 26, 27]. These algorithms use either supervised classification (*a priori* knowledge of feature classes) or unsupervised classification. In addition, the algorithms may or may not require detailed knowledge of statistical density functions. For this thesis, sample discrimination algorithms of each type are implemented.

The prototype information derived in the previous section serves as the basis for the first three discrimination algorithms used in this thesis: 1) Minimum Mean Distance (MM), 2) Mahalanobis Distance Minimization (MDM), and 3)

Nearest Neighbor. The fourth discrimination algorithm is unsupervised and hence disregards the prototype set. This algorithm is called K-means clustering. In this thesis, the seven SSM/I channels form the seven dimensional space used in the algorithms. Each unknown feature vector is a point in that space as is the mean for each vegetation class. The algorithms are now described.

5.5.1 Minimum Mean Discrimination (MM)

Minimum mean discrimination is a supervised, distribution-free algorithm [14]. The algorithm is tested by choosing a point of known vegetation type from the *World Ecosystems* map and then finding its feature vector from the seven SSM/I maps. The vegetation type is then estimated by calculating its feature vector's Euclidean distance from the mean brightness values of each vegetation class (see Table 5.2). The unknown feature vector's vegetation type is estimated as the class with the closest Euclidean mean. The estimation is then compared to the actual vegetation type to quantify the sensor's discriminatory capability. The algorithm yields linear discrimination functions and a very basic classification algorithm.

5.5.2 Mahalonobis Distance Minimization (MDM)

The main weakness of the minimum mean discrimination is its failure to take measurement distributions into account. These distributions are apparent in the differing standard deviations for each SSM/I channel within various surface vegetation classes. To overcome this weakness, the MDM algorithm assumes that each microwave channel of each vegetation class has a normal, correlated distribution. The vegetation is then discriminated using a supervised, distribution based Mahalonobis discriminant function described in [26]. The Mahalonobis discriminant function determines a score based on a non-Euclidean distance from the unknown feature vector to each vegetation type. The algorithm estimates the unknown vegetation type to be the type that yields the highest score. The covariance matrix for each vegetation class is approximated by the arithmetic average of the auto-Kronecker product for each prototype point and the probability of each vegetation class according to its surface percentage.

5.5.3 Nearest Neighbor (NN)

The nearest neighbor algorithm is similar to the minimum mean discrimination functions in that it uses the Euclidean distance between prototype vectors and undiscriminated feature vectors. The algorithm assumes that similar vegetation classes cluster together. To estimate a unknown vegetation class, the algorithm calculates the Euclidean distance from the unclassified feature vector to each of the prototype vectors. A specified number of the closest prototype are found and considered neighbors of the unknown feature vector. The unknown vector is estimated to be the vegetation class most common within the prototype neighbors. If a majority of the prototype neighbors are not dominated by one vegetation class then the algorithm determines that discrimination may not be performed. Jain [14] classifies this algorithm as supervised, distribution-free, and "piecewise linear."

5.5.4 K-Means Clustering (KMC)

The K-means clustering algorithm differs from the previously described algorithms because it is unsupervised. It does not use prototype statistics. Instead, the algorithm groups feature vectors into a user specified number of "clusters" so that the overall Euclidean distance within a cluster is minimized while the inter-cluster distance is minimized. The goal of this algorithm is to separate and cluster different feature vectors solely upon their measurement statistics. The algorithm, therefore, may cluster together two features corresponding to different vegetation types if they have similar feature vector values. In this way the algorithm indicates vegetation classes that have similar sensor responses. Similarly, two features of the same vegetation type may be split into different clusters due their differences in feature vector values. The differences may indicate large subclass variation in the vegetation type caused by geographical variation in surface temperature or elevation. Basically, clustering helps develop a natural correlation among the brightness temperature vectors which may or may not correspond to same-class vegetation clusters.

5.5.5 Discrimination Results

The discrimination algorithms described on the previous pages were tested by estimating the vegetation type of 1500 geographical points of known vegetation types and measured brightness temperatures. The discrimination is completely based on the brightness temperatures of the points and the prototype vector space described earlier.

Confusion matrices (See Tables 5.5 to 5.7) illustrate the discriminated vegetation types and the most common errors with other vegetation types for the supervised discrimination algorithms (MM, MDM, NN). The confusion matrices use the vertical axis to indicate the true vegetation type and the horizontal axis to indicate the estimated vegetation class. The far right column of each table indicates the percentage of points correctly discriminated between classes.

Major Amazon Surface Classifications		
ID	Description of Surface Type	Pct.
0	Ocean and sea	27.4
29	Tropical broadleaf seasonal, with dry or cool season	14.0
33	Tropical rainforest	14.7
41	Mild/warm/hot grass/shrub	14.8
43	Savanna/grass, seasonal woods interspersed	9.1
59	Succulent thorn woods or scrub is widespread	5.1

Table 5.4: Major Vegetation/Surface Classification Groups for Amazonian Region.

The supervised discrimination algorithms offer favorable results. The best discrimination algorithm is the nearest neighbor algorithm utilizing the majority of the nearest 25 neighboring prototype feature vectors. It perfectly discriminates the water and also has the highest minimum discrimination among any of the classes. Disregarding ocean and sea features, the algorithm correctly discriminates between vegetation types 65% of the time. The next best algorithm is the Mahalonobis algorithm at 60% correct and the minimum mean algorithm at 49% correct. These results clearly indicate a correlation between the vegetation types and the brightness temperatures since the percentages are much higher than uncorrelated data would produce. To put things in perspective, an unknown feature vector would be correctly discriminated less than 20% of the time if the classes

Minimum Mean Distance Discrimination								
		Estimated Vegetation Class						% Right
		29	33	41	43	59	0	
True Veg. Class	29	149	13	31	3	4	0	75
	33	70	84	38	7	1	0	42
	41	36	0	103	18	43	0	51
	43	52	31	66	15	36	0	7
	59	5	13	35	7	40	0	40
	0	0	0	6	0	0	218	97

Table 5.5: Confusion Matrix for Minimum Mean Discrimination Algorithm.

Mahalanobis Distance Discrimination								
		Estimated Vegetation Class						% Right
		29	33	41	43	59	0	
True Veg. Class	29	135	49	3	5	8	0	68
	33	18	177	1	2	2	0	89
	41	8	3	150	35	4	0	75
	43	31	54	45	60	10	0	30
	59	14	6	35	28	17	0	17
	0	0	0	0	1	0	223	99

Table 5.6: Confusion Matrix for Mahalonobis Discrimination Algorithm.

Nearest Neighbor Discrimination (Over 50% of 25 Neighbors)								
		Estimated Vegetation Class						% Right
		29	33	41	43	59	0	
True Veg. Class	29	136	48	8	5	3	0	68
	33	15	174	2	8	1	0	87
	41	5	4	166	9	16	0	83
	43	22	60	36	60	22	0	30
	59	1	11	32	8	48	0	49
	0	0	0	0	0	0	224	100

Table 5.7: Confusion Matrix for Nearest Neighbor Discrimination Algorithm.

were randomly estimated.

To better understand the success of the radiometer data, a discrimination is made using the nearest neighbor algorithm with the proven successful Seasat Scatterometer SASS images [25]. The results are found in Table 5.8. As one may see in the table, the SASS discrimination offers similar results to the radiometer data.

Previous work done by Long and Hardin [25] shows that SASS has better discriminatory abilities than this research yields. The cause of its decrease in reliability may be based in the two major differences between the work done by Long and Hardin [25] and this thesis: different discrimination algorithms and more detailed digitized truth maps. First, the nearest neighbor algorithm was chosen in this research for its superior performance with radiometer data. The algorithm used by Long and Hardin [25] optimized the discrimination for the scatterometer. Yet the similar results between the studies' algorithms tend to dismiss this as the main source of discrepancy. The "truth" maps used in the different studies offer a more likely reason for the lower discriminating ability. The map used by Long and Hardin [25] contained better resolution and more detailed types of vegetation

Nearest Neighbor Discrimination Using Seasat Scatterometer Image								
		Estimated Vegetation Class						% Right
		29	33	41	43	59	0	
True Veg. Class	29	138	44	1	15	2	0	69
	33	19	178	0	2	1	0	89
	41	3	8	158	5	26	0	79
	43	62	30	76	17	15	0	9
	59	6	0	48	12	34	0	34
	0	0	0	6	0	0	224	100

Table 5.8: Confusion Matrix for Nearest Neighbor Discrimination Algorithm Applied to Seasat Scatterometer Data.

than the digitized map in this thesis [24]. Thus, the map used in this thesis may have biased both the discriminating ability of the SSM/I data as well as the SASS data. As will now be presented, the non-supervised clustering algorithm supports this claim.

The last discrimination algorithm applied to SSM/I data is K-means clustering. As mentioned earlier, the K-means algorithm does not attempt to discriminate between vegetation types but instead to do a non-supervised clustering of similar vegetation brightness temperature feature vectors. The algorithm divides the prototype points into five main clusters (See Table 5.9). The first three clusters are dominated by class 41 and the other clusters by vegetation types 33 and 29. Only the first cluster, however, has over three quarters of the cluster as one vegetation type.

Clustering the SASS data (see Table 5.10) using the K-means clustering yields similar results to the SSM/I data: only one cluster has over 75% from the same vegetation class. Although SASS may be considered slightly better because

Cluster	Pts.	Veg. Types	Pct.
1	413	41	76
		33	10
2	793	41	32
		43	24
		33	22
		29	11
	518	41	37
		59	25
		43	19
		29	17
4	1497	33	43
		43	20
		29	16
5	1206	29	38
		43	19
		33	15
		59	15

Table 5.9: SSM/I K-Means Clustering Results for 5000 Point Prototype Feature Vectors.

its clusters are more strongly dominated by unique vegetation types, the unsupervised clustering suggests that the SSM/I has discriminatory abilities close to those of other spaceborne sensors such as SASS.

5.6 Conclusion of Vegetation Discrimination

I have illustrated the use of enhanced resolution SSM/I images to extract geophysical data over heavily vegetated land masses. The radiometric images offer vegetation discrimination similar to the discrimination available from scatterometer images. Although the radiometer images can not be used as an exclusive vegetation classifier, they do contain discrimination ability. A multi-sensor approach combining both the radiometer and scatterometer may yield better results.

I do not claim to have found optimal geophysical extraction methods from all discrimination algorithms; instead it shows that enhanced resolution background images produced by SIR have potential. This potential may be better used in traditional radiometric studies which require surface temperatures or direct moisture content readings. The vegetation discrimination, however, shows that the

SASS K-Means Clustering Results			
Cluster	Pts.	Veg. Types	Pct.
1	468	41	78
		43	20
2	855	41	51
		59	27
		43	18
3	1333	33	67
		29	17
		43	11
4	1183	29	50
		43	26
		33	16
5	751	59	40
		41	27
		43	19
		29	11

Table 5.10: SASS K-Means Clustering Results for 5000 Point Prototype Feature Vectors.

enhanced resolution, atmospheric distortion-free images increase the radiometric utility to studies usually dominated by other sensors.

CHAPTER 6

CONCLUSIONS

6.1 Discussion

This thesis explores the use of enhanced resolution radiometric images in extracting geophysical information about the Amazon Basin. This research is driven mainly by the need to gather multidecadal data about the Amazon Basin. Multidecadal data from microwave radiometers is available but its low resolution limits its utility in land-based studies. This thesis compares methods to improve the resolution of radiometer data, offering a possible method to use the existing data. This research uses data from the Special Sensor Microwave/Imager to investigate these methods. The thesis draws the following conclusions and results:

1. The image reconstruction methods known as the Backus Gilbert Inversion technique and Scatterometer Image Reconstruction Algorithm are both suitable for generating enhanced resolution images. These images improve resolution over raw data in amounts previously found [6]. The enhanced resolution is illustrated in both simulated and actual SSM/I data.

2. Since SIR is computationally more efficient than BGI, it is a much faster algorithm making it preferable in large area image reconstructions such as the Amazon Basin. The processing time is approximately twenty times faster.

3. Reconstructed SSM/I images over the Amazon Basin indicate small-spatial scale, temporal atmospheric effects caused by clouds and precipitation. These effects appear as random dark spots in images reconstructed from single satellite pass data.

4. Images without the small-spatial scale atmospheric distortion may be generated by compositing images created from single satellite pass images through a technique called Modified Maximum Average. The composite images remove the atmospheric distortion and lessen the sensor noise level. Simulation results suggest that resulting image may be biased high.

5. Enhanced resolution radiometric images have vegetation discrimination capabilities. Scatterometer studies yield similar, but superior, results. A clustering algorithm shows that the scatterometer data naturally is dominated to a greater extent by vegetation type than the radiometer data. Nevertheless, the radiometric images offer abilities usually ignored in non-traditional radiometric land studies. The vegetation discrimination in this thesis is limited by coarser, less descriptive truth data than previous scatterometer studies. The truth data has low spatial resolution which may be a factor in limiting the radiometer's discrimination capability to 60%.

6.2 Contributions

The contributions of this thesis are: (1) a simulation comparison of the Backus Gilbert Inversion technique and the Scatterometer Image Reconstruction algorithm, (2) an application of BGI and SIR to Amazon Basin imagery, (3) an objective algorithm to remove atmospheric distortion from SSM/I Amazon images, (4) a comparison of several techniques to create composite SSM/I images from multipass data, (5) a study to discriminate between Amazon vegetation using enhanced images, (6) and a summary comparison of vegetation discrimination abilities between scatterometer and radiometer enhanced images.

6.3 Future Research

The vegetation discrimination and image compositing algorithms only use SIR processed images in this thesis. The SIR images are used because SIR is superior to BGI in processing efficiency. Further research can verify if BGI enhanced resolution images yield similar vegetation discrimination abilities as SIR images.

Methods to optimally pick the BGI parameters to suppress noise and increase resolution are not investigated in this thesis. The NSIZE parameter, especially, has not been analyzed although its large effect on processing is noted in this thesis. Methods to optimally chose this and the other parameters are needed.

Methods to combine images and remove atmospheric distortion based on order statistics and quantile techniques need to be further investigated. This

study could provide theoretical support for the existing techniques which have been previously justified on an *ad hoc* approach. For example, future research could include modeling a "third highest" value technique, etc.

The SSM/I images in this thesis suggest that they have discriminatory potential. This vegetation discrimination may be improved by using multisensor data. This includes discriminatory algorithms which utilize both scatterometer and radiometer data. Methods which more efficiently use polarization differences in the SSM/I channels are also needed. The polarization differences should be useful in detecting areas of standing water and grass.

Lastly, the "base" composite images act as background surface brightness maps. This thesis uses those maps in vegetation discrimination. Other research may use these maps along with enhanced images of single pass data to detect and evaluate clouds and precipitation. The differences between the "base" images and the single pass images may be related to geophysical parameters such as cloud particle size and water vapor content. This may aid weather prediction over densely vegetated areas.

BIBLIOGRAPHY

[1] F. T. Ulaby, R. K. Moore, and A. K. Fung, *Microwave Remote Sensing, Active and Passive*, vol. 1. Norwood, MA: Artech House Inc., 1981.

[2] T. J. Jackson and T. J. Schmugge, "Algorithm for the Passive Microwave Remote Sensing of Soil Moisture," in *Microwave Radiometry and Remote Sensing Applications* (P. Pampaloni, ed.), (Zeist), pp. 3–17, VSP, 1989.

[3] P. Pampaloni and S. Paloscia, "Microwave Emission and Plant Water Content: A Comparison Between Field Measurement and Theory," *IEEE Transactions on Geoscience and Remote Sensing*, vol. 24, pp. 900–904, November 1986.

[4] M. J. McFarland, R. L. Miller, and C. M. U. Neale, "Land Surface Temperature Derived From the SSM/I Passive Microwave Brightness Temperatures," *IEEE Transactions on Geoscience and Remote Sensing*, vol. 28, pp. 839–845, September 1990.

[5] D. G. Long, P. J. Hardin, and P. T. Whiting, "Resolution Enhancement of Spaceborne Scatterometer Data," *IEEE Transactions on Geoscience and Remote Sensing*, vol. 31, pp. 700–715, May 1993.

[6] W. B. Davis, "Enhanced Resolution Imaging from Remotely Sensed Microwave Data," master's thesis, Brigham Young University, Provo, UT, 1993.

[7] W. D. Robinson, C. Kummerow, and W. S. Olson, "A Technique for Enhancing and Matching Resolution of Microwave Measurements from the SSM/I Instrument," *IEEE Transactions on Geoscience and Remote Sensing*, vol. 30, pp. 419–429, May 1992.

[8] M. R. Farrar and E. A. Smith, "Spatial Resolution Enhancement of Terrestial Features Using Deconvolved SSM/I Microwave Brightness Temperatures," *IEEE Transactions on Geoscience and Remote Sensing*, vol. 30, pp. 349–355, March 1992.

[9] J. Hollinger, R. Lo, G. Poe, R. Savage, and J. Peirce, *Special Sensor Microwave/Imager User's Guide.* Washington, D.C.: Naval Research Laboratory, 1987.

[10] A. S. Jones and T. H. V. Haar, "Passive Microwave Sensing of Cloud Liquid Water Over Land Regions," *Journal of Geophysical Research*, vol. 95, pp. 16673–16683, September 1990.

[11] R. W. Spencer, H. M. Goodman, and R. E. Hood, "Precipitation Retrieval over Land and Ocean with the SSM/I: Identification and Characteristics of the Scattering Signal," *Journal of Atmospheric and Oceanic Technology*, vol. 6, pp. 254–273, April 1989.

[12] N. C. Grody, "Classification of Snow Cover and Precipitation Using the Special Sensor Microwave/Imager," *Journal of Geophysical Research*, vol. 94, pp. 7423–7435, April 1991.

[13] F. J. Wentz, *User's Manual SSM/I Antenna Temperature Tapes.* Santa Rosa, CA: Remote Sensing Systems, 1991.

[14] A. K. Jain, *Fundamentals of Digital Image Processing.* Englewood Cliffs, NJ: Prentice-Hall, 1989.

[15] G. A. Poe, "Optimum Interpolation of Imaging Microwave Radiometer Data," *IEEE Transactions on Geoscience and Remote Sensing*, vol. 28, pp. 800–810, April 1990.

[16] B. Caccin, C. Roberti, P. Russo, and A. Smaldone, "The Backus-Gilbert Inversion Method and the Processing of Sampled Data," *IEEE Transactions on Signal Processing*, vol. 40, pp. 2823–2825, November 1992.

[17] P. T. Whiting, "Resolution Enhancement of Seasat Scatterometer Data," master's thesis, Brigham Young University, Provo, UT, 1992.

[18] C. M. U. Neale, M. J. McFarland, and K. Chang, "Land-Surface-Type Classification Using Microwave Brightness Temperatures From the Special Sensor Microwave/Imager," *IEEE Transactions on Geoscience and Remote Sensing*, vol. 28, pp. 829–838, September 1990.

[19] S.D.Prince and B. J. Choudhury, "Interpretation of Nimbus-7 37 GHz Microwave Brightness Temperature in Semi-arid Southern Africa," *International Journal of Remote Sensing*, vol. 10, no. 10, pp. 1643–1661, 1989.

[20] T. Fung and E. LeDrew, "The Determination of Optimal Threshold Levels for Change Detection Using Various Accuracy Indices," *Photogrammetric Engineering and Remote Sensing*, vol. 54, pp. 1449–1454, October 1988.

[21] B. Choudhury and C. Tucker, "Satellite Observed Seasonal and Inter-Annual Variation of Vegetation Over the Kalahari, The Great Victoria Desert, and The Great Sandy Desert: 1979-1984," *Remote Sensing of Environment*, vol. 23, pp. 233–241, 1987.

[22] P. M. Narenda, "A Separable Median Filter for Image Noise Smoothing," *IEEE Transactions on Pattern Analysis and Machine Intelligence*, vol. 3, pp. 20–29, January 1981.

[23] J. D. Gibbons, *Nonparametric Statistical Inference, 2cd Ed.* New York, NY: Marcel Dekker, 1985.

[24] J. J. Kineman and M. A. Ohrenschall, *Global Ecosystems Database Documentation Manual.* Boulder,Colorado: United States Department of Commerce, 1992.

[25] D. G. Long and P. J. Hardin, "Vegetation Studies of the Amazon Basin Using Enhanced Resolution Seasat Scatterometer Data," *IEEE Transactions on Geoscience and Remote Sensing*, vol. 32, pp. 449–460, March 1994.

[26] R. O. Duda and P. E. Hart, *Pattern Classification and Scene Analysis.* New York, NY: John Wiley and Sons, 1973.

[27] C. W. Therrien, *Decision Estimation and Classification: An Introduction to Pattern Recognition and Related Topics.* New York, NY: John Wiley and Sons, 1989.